Formation of Fe-rich subsurface precipitate layers on White Island, New Zealand

---

A THESIS SUBMITTED IN PARTIAL FULFILMENT

OF THE REQUIREMENT FOR THE DEGREE

OF

Master of Science in Geology

AT THE

DEPARTMENT OF GEOLOGICAL SCIENCES

UNIVERSITY OF CANTERBURY

by Noel Antony Win

University of Canterbury

2014

Frontispiece

Transformation of Fe is a quick and active process at White Island. The image above shows a of Fe flywheel (≈1m across) being corroded/oxidised by volcanic gases at the old sulphur factory near Crater Bay. Iron chemistry is dynamic, active and ongoing within the volcanic/hydrothermal environment observed in the Main Crater at White Island.

Abstract

White Island is a highly active volcano with an acidic, S-rich hydrothermal system in the Bay of Plenty, North Island, New Zealand. In this acidic environment a series of subsurface Fe-rich layers are ubiquitous in the crater sediments at shallow depth and are capable of modifying the fluid and gas flux dynamics in the system. The mineralogy of the subsurface Fe-rich layer(s) and the processes leading to their formation are unknown. Here the mineralogy and formation of the subsurface Fe-rich layers in relation to the surface and subsurface environment(s) within the Main Crater at White Island are assessed. Based on geochemical analyses, subsurface Fe-rich crusts are composed of a mix of jarosite and goethite, cementing crater fill sediments into cohesive layers. Saturation index (SI) and Eh/pH assessments identify that fluids evolved at White Island are undersaturated with respect to the mineral phases present in the Fe-rich subsurface layers. Formation of the Fe-rich subsurface layers is most likely related to the transition between atmospheric gases and/or meteoric water mixing with hydrothermal fluids/gases. This transition zone creates an environment conducive to forming jarosite and goethite forming in the same layer. Additionally, subsurface sediments including the Fe-rich layers show a consistent organic carbon isotopic signature of -23 ‰. Microscopic investigations confirm diatoms and microbes are present in the subsurface Fe-rich layers. The full extent of microbial activity in relation to the Fe-rich layers at White Island still requires further investigation. Based on chemical extractions for isotopic analyses, Fe-rich layers are shown to preserve $\delta^{13}C$ signatures indicative of microbial life. Interface zones such as those identified in the hydrothermal environment at White Island can create metal-rich deposits and habitable/preservative microbial environments as well as affecting the macroscopic dynamics of volcanic and epithermal systems.

Keywords: White Island, Volcanic, Hydrothermal, Geochemistry, Microbes, Fe-rich precipitates, Epithermal

Acknowledgements

Firstly a big thank you to my supervisors Dr Chris Oze, Dr Ben Kennedy and Dr Travis Horton. Chris for his time, effort and for listening to even my craziest theories. Giving me the freedom to think and then pushing me towards to the right direction. As well as his tireless efforts editing and teaching me about academic writing. Ben, his excitement and energy about all things volcanic, made learning about volcanism fun and to Travis his work and knowledge on carbon chemistry is amazing. Their input and combined knowledge helped me immensely during my journey.

Dr Kerry Swanson, his knowledge/advice about hunting microbes and how to prepare biological samples for SEM was invaluable. Dr Maree Hemmingsen thanks for all the quips/jokes, advice and for help with editing of my thesis. Toni Cox for some pointers and edits. Chris Grimshaw for all his help with sample preparation and advice on different methods. To all the geology department staff and support staff who have made my undergrad and postgrad enjoyable and making the department feel like an extended family. Thanks to my office mates in room 401, the pranks and feeling of camaraderie, made it worth turning up every day. A big thank you to Mark Letham-Brake who gave me the opportunity to visit White Island as a field assistant (2012) and later helped with field work (2013) and to Matt Hanson for his help during the 2013 field work trips.

Thanks to Professor Keith Gordon, Department of Chemistry, University of Otago for access to the raman equipment and to Geoffrey Smith for running the equipment, collecting data over two days, as well as helping with analyses. The Buttle Family Trust for allowing access to White Island and to Pee Jay Tours for providing transport to the island. Karibu backpackers for an enjoyable stay in Whakatane. Funding for this project came from the Mason Trust, Department of Geological Sciences at the University of Canterbury.

To the Ashworths for the accommodation while I was in Dunedin and lastly to the Win family for there continued support, help and encouragement over the years, without which I would not be back at university completing my Thesis.

Contents

Figures

Tables

Scientific Glossary, Abbreviations and Acronyms

AA : Amyl Acetate
bd : below detection limit
CPD : Critical point dryer, this is an instrument used to dry biological and mineral samples using critical point CO_2
δ^{13}C‰ : A measure of the ratio of stable isotopes ^{13}C : ^{12}C, reported in parts per thousand (per mil, ‰)
δ^{13}C : Isotopic signature for analysed sample
DNA : Deoxyribonucleic acid
EDS : Energy Dispersive Spectrometery
Eh : Oxidation / reduction potential
EPS : Extracellular polymeric substance
Fe : Iron
Fe^{2+} : Valence state 2+ iron (ferrous iron)
Fe^{3+} : Valence state 3+ iron (ferric iron)
GGW : GNS Science Geothermal and Groundwater Database
nd : None detected
pH : Measure of the acidity or basicity
ppm : Parts per million
SEM : Scanning Electron Microscope
SI : Saturation Index
S : Sulphur
wt% : Weight percent
XRD : X-ray Diffraction
XRF : X-ray Fluorescence
ZVI : Zero valence iron

Chapter 1: Introduction

1.1 Overview

White Island is an island strato/composite volcano with a highly active and accessible/shallow epithermal system. Hydrothermal fluids in an epithermal system(s) mobilise and transport dissolved metals/elements, which may precipitate to form metal-rich deposits in subsurface environments (White and Hedenquist, 1990; Hedenquist and Lowenstern, 1994; Sillitoe and Hedenquist, 2003). A variety of Fe-rich precipitate deposits are present on the surface and in the subsurface sediments of the Main Crater of White Island. Of particular interest are a series of Fe-rich subsurface precipitate layers cementing crater sediments into hard layers. These subsurface Fe-rich layers show decreased porosity and permeability over unconsolidated crater sediments (Letham-Brake, 2013). The subsurface Fe-rich layers are forming in a highly acidic environment which are generally not conducive for the precipitation and deposition of most Fe-rich minerals (Bigham et al., 1996a,b). The Fe-rich subsurface layer(s) potentially cover a large area, as much as several 100 m^2; however, the extent is unknown due the continual deposition of volcanics and related sediments. The formation of the subsurface Fe-rich precipitate layers at White Island presents an opportunity for further investigation into Fe deposition/chemistry in a active hydrothermal environment.

On White Island a variety of chemical pathways may result in the formation of Fe precipitates in the subsurface environment. These pathways may be related to: 1) epithermal (hydrothermal) fluids (White and Hedenquist, 1990; Hedenquist and Lowenstern, 1994; Scher et al., 2013), 2) weathering (Bigham and Nordstrom, 2000; Curtis, 2003; Mathur et al., 2011), 3) microbial interactions (Brown et al., 1999; Warren and Kauffman, 2003; Kappler and Straub, 2005; Konhauser et al., 2011; Southam, 2012), 4) a combination of 1), 2) and/or 3). Each of these processes have been known to form subsurface Fe-rich precipitate layers in other volcanic systems. Epithermal fluids can leach rock and carry elements upwards towards the surface creating Fe-rich layers (White and Hedenquist, 1990). Weathering can leach and mobilise elements downwards (Mathur et al., 2011) and microbal actively can actively or passively create Fe-rich precipitate(s) (Fortin and Langley, 2005).

Assessing the internal interfaces (redox/geochemical) within an active hydrothermal system such as the one seen at White Island allows for direct observations and measurements of the dynamic systems involved in Fe mineral deposition. The formation of Fe-rich precipitate(s) is dependent on the redox chemistry. The redox chemistry of the

subsurface environment affects the dominant valence state of Fe available and the types of geochemical/biogeochemical reactions that can proceed. How these redox reactions interact between epithermal fluids, weathering and microbial interactions will provide an understanding of the processes leading to the formation of Fe-rich deposits at White Island as well as other similar geological environments. Here the mineralogy, geochemistry and redox conditions at White Island is investigated to understand the formation of the subsurface Fe-rich crusts within this S-rich volcanic hydrothermal environment. This thesis is a step towards understanding the processes leading to the formation of Fe-rich layers in the shallow subsurface and some of the potential outcomes related to the layers formation within this S-rich volcanic environment.

1.2 Research purpose and objectives

The objective of this research is to evaluate the geochemical and potentially biogeochemical pathways leading to the formation of Fe-rich subsurface precipitate layers at White Island. The main hypothesis is that these Fe-rich precipitate layers represent a redox front/boundary between the epithermal system and near-surface environment. Additionally, microbial activity interacting within the system maybe influencing the formation of the Fe-rich layers. To answer the main hypothesis, the following questions were used as a guide: 1) What are the Fe-rich precipitates and how are they forming? 2) Are microbial communities present in this layer? 3) If so, how might they be interacting with it?

To understand the geochemical and biogeochemical environment leading to the formation of the subsurface Fe-rich deposits at White Island, field work, laboratory analysis and chemical modelling was undertaken. The mineralogy was investigated using microscopy, petrography and scanning electron microscopy (SEM) in order to assess vesicularity, weathering and mineralisation. X-ray diffraction (XRD) was used to provide information on crystalline components making up the Fe precipitate layers. X-ray fluorescence spectrometer analysis (XRF) provides data on the bulk chemistry of Fe layers. Raman spectroscopy was utilised to provide information about speciation of minerals (especially for determining Fe oxyhydroxide phases) and SEM with Energy Dispersive Spectrometery (EDS) was used to provide mineral chemistry.

The biogeochemistry was investigated using carbon chemical analysis and SEM. Isotopic and total carbon values were analysed to provide evidence of microbial activity. SEM analysis was completed to visually confirm the presence of any microbes in the samples taken around White Island. Both methods were used to provide insight into the type and potential abundance of microorganisms in the Fe-rich layers. Chemical analyses were completed on water samples from creeks in the Main Crater to understand the fluid chemistry. Redox and chemical analyses of the hydrothermal water was used in geochemical modelling using PHREEQC (Version 3) and PhreePlot was used to inves-

tigate the different pathways of formation and the likelyhood of Fe-precipitates formation.

This thesis is a step towards understanding the Fe chemistry and the formation of the subsurface Fe-rich layers in the hydrothermal environment at White Island. Information garnered provides insight into Fe chemistry at other similar acidic sulphur-rich hydrothermal systems. Additionally, this study may provide insights into the role and abundance of biology in subsurface Fe-layers in an active epithermal and hydrothermal system.

1.3 Thesis structure

The thesis is organised into six chapters as outlined below.

Chapter 1: This chapter provides an overview and the research aims and objectives and an outline of the thesis. This section introduces epithermal systems and metal precipitate formation, as well as providing a description of the potential pathways for creating the subsurface Fe-rich precipitates seen at White Island.

Chapter 2: Background geology, geochemistry and mineralogy of White Island is covered and information about Fe precipitate deposits, common mineral species and formation in other similar acidic environments, microbial activity related to formation of Fe-precipitates is presented.

Chapter 3: This methods chapter describes the experimental work, materials, analyses and calculations used to provide data for this thesis.

Chapter 4: The results presented in this chapter are divided into four sections: 1) field sampling and observations, 2) mineralogy and geochemistry, 3) biogeochemistry and 4) geochemical modelling.

Chapter 5: Results from chapter 4 are discussed with respect to Fe chemistry on White Island, mineralogy, formation of the Fe-rich subsurface precipitate layers, potential microbial influence and potential future outcomes from the layers formation.

Chapter 6: A summary of this thesis is provided.

Chapter 2: Background

2.1 White Island

White Island (Whakaari) is an active volcanic island approximately 50 km north of the coast of the Bay of Plenty on the North Island of New Zealand (Figure 2.1) and it represents the northern most expression of the Taupo Volcanic Zone (TVZ). The volcano is a stratovolcano that rises 1600m above the sea floor and contains a large central crater, close to sea level.

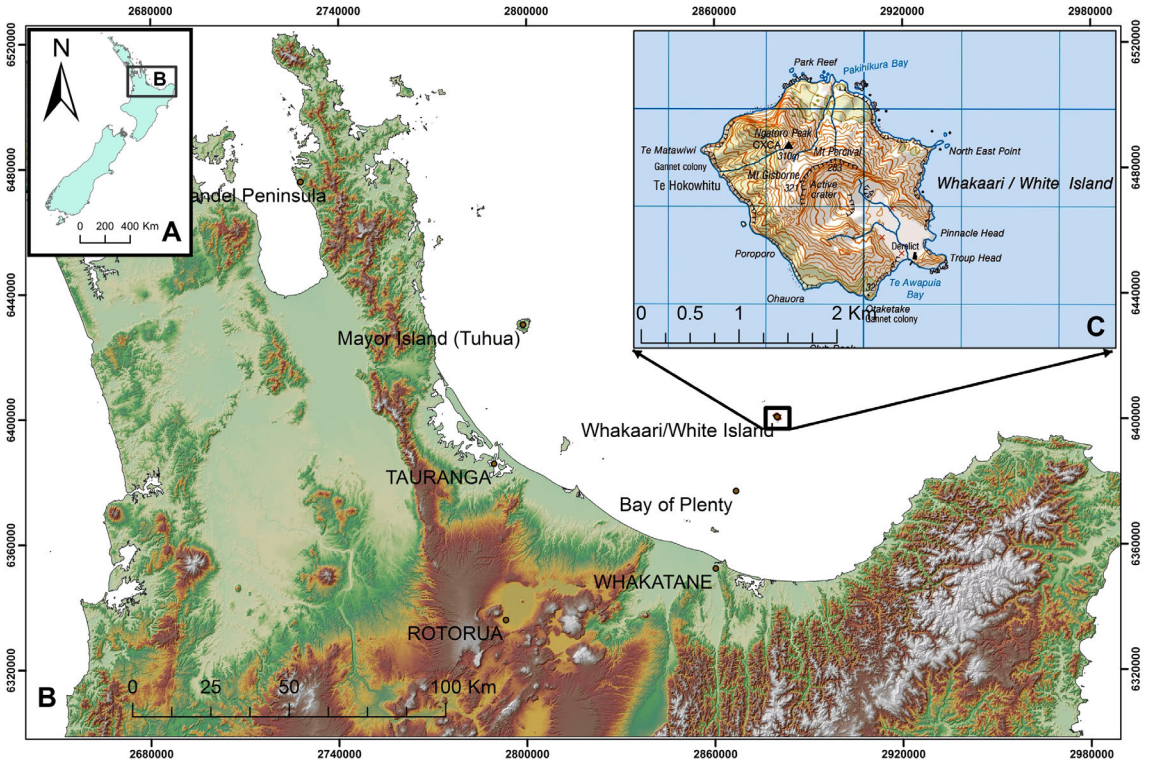

Figure 2.1 – Orientation maps: (A) large orientation map of New Zealand, (B) Upper North Island, Bay of Plenty area and position of White Island and, (C) White Island. (Map data sources see Appendix A).

Volcanism at White Island is driven by subduction of the Pacific plate under the Australian Plate (Cole et al., 2000). The present island volcano complex consists of two overlapping cones, the remnants of the older cone form the western edge in the Mt Ngatoro area and the younger which overlaps the older cone and forms the majority of the island (Black, 1970). The current Main Crater area, shown in Figure 2.2 was created by a sector collapse that breached the cone to the southeast and currently takes up a large area of the island (Black, 1970; Moon et al., 2009). The Main Crater can be subdivided into three subcraters (Centre, Western and Eastern) as shown in Figure 2.2.

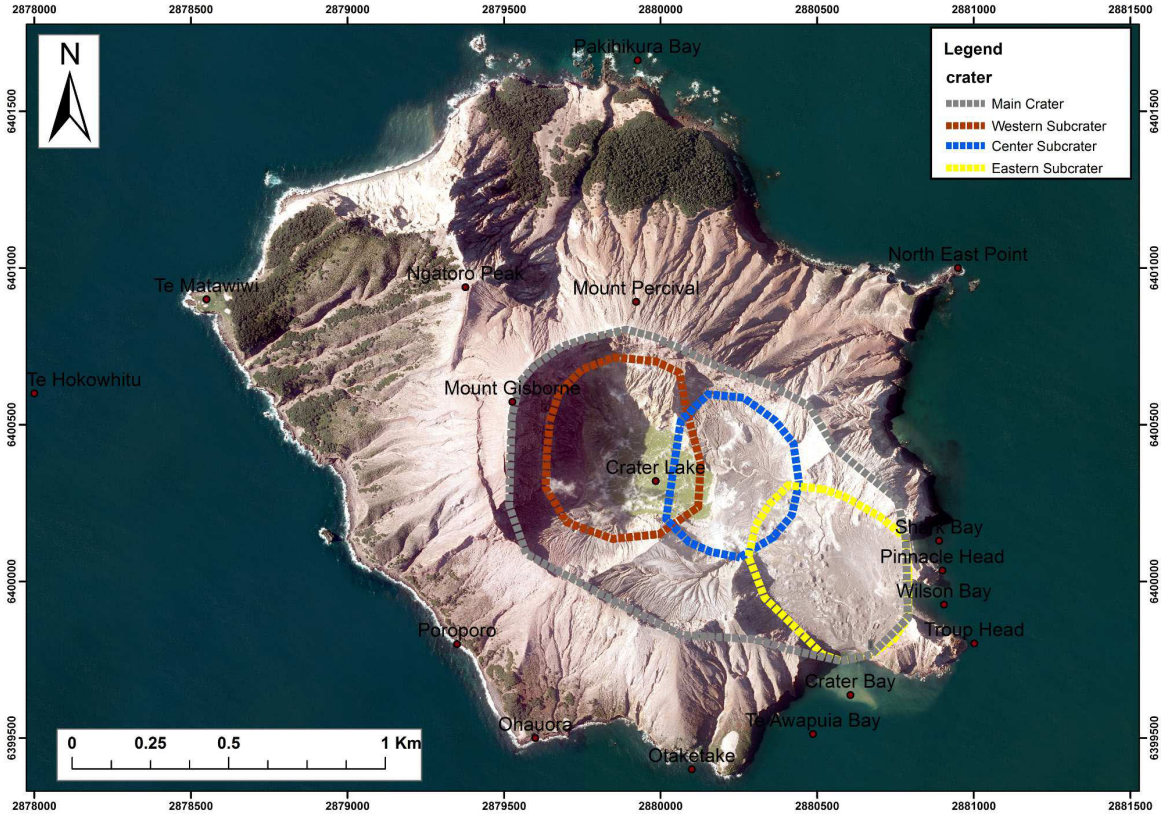

Figure 2.2 – A topographic map of White Island showing land marks, Main Crater and subcrater zones. The subcrater subdivision areas are from Cole et al. (2000) and Moon et al. (2005). (Map data sources see Appendix A).

The sector collapse that created the Main Crater area is thought to have been caused by a telescoping porphyry and hydrothermal alteration, which weakened the crater walls leading to the destabilisation and crater wall collapse (Sillitoe, 1994). The resulting sector collapse removed a large amount of confining volcanic rock, depressurising the volcanic system and changing the style of volcanic activity (Moon et al., 2009; Letham-Brake, 2013). The base of the Main Crater is filled to an unknown depth with a varied mix of volcaniclastic eruptive products (Mongillo and Wood, 2000). The volcaniclastic products that fill the crater include ash, tephra, volcanic bombs, lava, crater lake sediments and altered rock from the crater walls as well as debris from a crater rim collapse causing the 1914 debris avalanche. Many of the large mounds in the crater today are hummocks created during deposition of the 1914 debris avalanche (Black, 1970). The crater fill is added to by collapse, weathering of crater walls and constant volcanic eruptions.

The volcanic ash, lapilli and lavas that make up the stratocone and fill the crater have a composition that ranges from andesite to dacite. The lavas are commonly made up of glassy to hypocrystaline ground mass with 10 - 20% phenocrysts made up of feldspar, pyroxenes, olivine and magnetite in order of abundance (high to low) (Hedenquist et al., 1993; Cole et al., 2000). The feldspar phenocrysts are dominantly plagoclase (An_{52-97}),

pyroxenes (50/50 ortho- and clino-pyroxenes), which plot in the enstatite and augite fields. The spinels are magnetite and chromite and olivine is dominantly Fo_{88-97} (Cole et al., 2000). The lavas have a total Fe range of between 6.20% to 8.13% with an average of 7.23% and all the erupted lavas are very low in sulphur generally $< 0.04\%$ (see Appendix B).

The historical volcanic activity at White Island has been characterised by continuous, intense fumerolic activity with common small phreatic, phreatomagmatic and strombolian eruptions (Haughton and Nairn, 1991). The hydrothermal system has been active for at least the past 10,000 yrs (Hedenquist and Lowenstern, 1994). Most of the visibly active fumaroles are confined to within the Main Crater zone. The crater floor rises gradually from sea level at the bays to the east, up to the lip of the current crater lake approximately 20m above sea level. Acidic streams flow out of the bases of fumaroles and hotpools across the Main Crater floor to the sea at Crater Bay.

2.2 Water chemistry of White Island

The water chemistry of a hydrothermal site like White Island provides insight into the types of minerals that could form from the fluids, as well as the type of environment the Fe-precipitates may be forming in (i.e acidic/basic). The hydrothermal fluids seen at White Island are made up of a mix of magmatic gases/fluids, seawater and meteoric water, these fluids leach, dissolve and alter volcanic host rock creating hydrothermal brines rich in dissolved elements (Giggenbach et al., 2003). Data in this section has been compiled from the GNS Science Geothermal and Groundwater Database (GGW) found at http://ggw.gns.cri.nz/ggwdata/ (accessed: 28/05/2013). The water(s) at the surface of White Island is divided into several types : (1) the crater lake, (2) surface outflows seeps, hotpools and other features connected to ground water at depth, and (3) streams and creeks.

Table 2.1 – Water temperature, pH, Fe, S content averages from all sites sampled at White Island (GNS Science Geothermal and Groundwater Database)

	Average Water temperature	Average pH	Average Iron content mg/L	Average Sulphate mg/L (as SO4)
(1) Crater Lake	53.72	0.16	4541.95	15126.28
(2) Surface outflows	88.24	2.09	1122.00	4137.00
(3) Creeks and Streams	47.74	1.19	1529.85	6491.42

Average temperature, pH, iron, sulphur in Table 2.1 show how different the crater lake fluids are from the surface outflows and the creeks and streams. The crater lake is in a depression at the Western subcrater, the difference in the crater lake elemental concentrations is most likely due to the lake being directly above the magmatic source. Additionally the elements are being concentrated through evaporation making the crater lake fluids acidic and metal-rich. The crater lake is segregated from the creeks (sits in a

depression below the crater floor surface level) in the western Subcrater (see Figure 2.2) and does not currently outflow into the creek system.

The streams and surface outflows have similar attributes this is most likely due to the streams being fed by surface outflows sources across the crater, which are connected to upwelling subsurface hydrothermal waters (Note: A table with all the water chemistry values is in Appendix C). Not all of the surface outflows add water into the creeks and are potentially coming from different depths/zones within the hydrothermal system. This may explain some of the concentration and acidity variations between the different creeks and surface outflows. All the water sources have an average low pH of < 2.09 and high concentrations of dissolved Fe ranging from 0.05 to 12,110 mg/L and sulphur range from 660 to 37,612 mg/L.

2.3 Gas flux and gas chemistry

The volcanic system at White Island is actively degassing from fumaroles and through the sediments in the crater floor. Figure 2.3A shows small clouds of condensing gases coming out of sediments on cold day. Figure 2.3B shows a grey/white solfatara developing around actively degassing fumarole. The solfatara deposits are made up of a mix of minerals, which can include alunite, gypsum, silica and native sulphur.

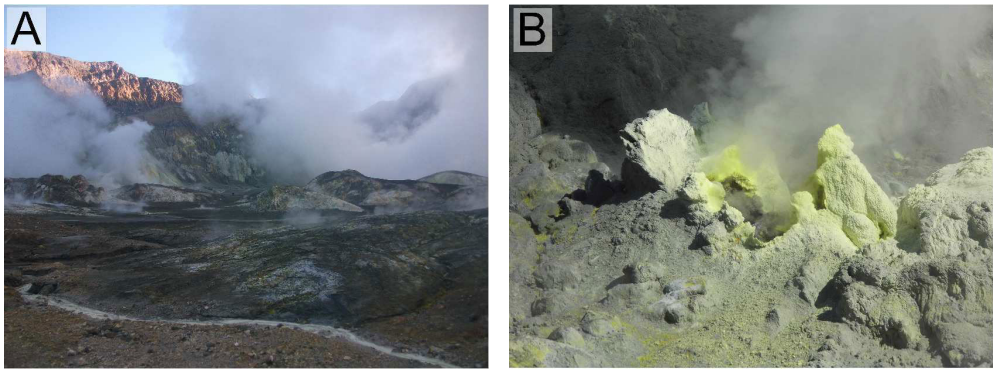

Figure 2.3 – (A) Gases rising from Main Crater, fumaroles and crater floor.(B) White/grey solfataras and native sulphur depositing around degassing fumarole.

The gas discharges are made up of two source components: (1) a primary "magmatic" component high in SO_2, rising rapidly and directly from the underlying magma and (2) a secondary "hydrothermal" component rising slowly from a two-phase, saline brine-vapour envelope surrounding the magmatic system (Giggenbach, 1987). It was thought that the hydrothermal system is chemically sealed and that there is no/limited mixing between (1) primary and (2) secondary gases/fluids. Current isotopic evidence suggests there is lateral infiltration of seawater into the hydrothermal system (Giggenbach et al., 2003;

Bloomberg, 2012). The gasses coming out of the fumaroles in the Main Crater have been studied, since the 1970s (Giggenbach, 1987) and can be summarised as being mainly H_2O, CO_2, H_2S and SO_2 (Giggenbach, 1987; Giggenbach and Matsuo, 1991; Hedenquist and Lowenstern, 1994). Complete gas compositions and totals are in Appendix D.

White Island has flux values for H_2O, CO_2, SO_2 are H_2O 1.9x10^6 t yr^{-1}, CO_2 0.44x10^6 t yr^{-1}, SO_2 0.13x10^6 t yr^{-1} measured by spectrometry (Hedenquist and Lowenstern, 1994). The hydrothermal system actively degases through permeable areas around the crater and it is hypothesized that subsurface clay layers are considered to be a major control on degassing pathways at White Island. An isotopic study of the CO_2 going through the crater floor by Bloomberg (2012) shows a minimum $\delta^{13}C_{CO_2}$ value of -10.2‰ with an average $\delta^{13}C_{CO_2}$ value of -5.8‰. The average $\delta^{13}C_{CO_2}$ value of -5.8‰ indicates the soil is being saturated with a mix of magma-hydrothermal sourced CO_2 with some input from background sources (atmospheric and/or microbial respiration).

2.4 Temperature flux across the crater

White Island has both active magmatic vents and a vent-hosted hydrothermal system, heat flow to the surface varies in a complex manner (Browne and Cole, 1973). The structures that control the flux of fluid and gases across the Main Crater most likely control heat flux, since water/gases/heat are closely associated in hydrothermal systems. The shallow soil temperatures across the crater can range from 10℃ (ambient) to 100℃ (boiling point) (Bloomberg, 2012). The temperature range measured in the gasses coming out of the fumaroles ranged from 100 to >700℃ (Giggenbach, 1987). A long term study undertaken between 1968 to 1971 by Browne and Cole (1973) found that there were constant temporal and spacial variations of temperature across the crater floor, which were attributed to volcanic activity. Such as the temperature decrease observed at monitored sites after the 19 July 1971 eruption. Bloomberg (2012) found that shallow soil temperatures had arithmetic mean of 40.3 ℃ and an declustered mean of 37.0℃. Temperature is one of the many factors that will be accounted for during this study when looking at Fe-chemistry. Since temperature effects the kinetics (reactivity) and thermodynamics (stability) of the chemical reaction(s) involved in Fe precipitation.

2.5 Fe and the formation of Fe-rich precipitate deposits

Iron (Fe) exists in a range of oxidation states from -2 to +6, the most common oxidation states being Fe^{2+} (ferrous iron) and Fe^{3+} (ferric iron) (Taylor and Konhauser, 2011). Fe^{2+} is relatively water soluble and Fe^{3+} is highly water insoluble. In the most common surface conditions, an oxygenated environment with near neutral pH conditions Fe is relatively immobile and locked in stable Fe^{3+} oxides or mineral complexes. In reducing or low pH (acidic) Fe^{2+} is more dominant and Fe becomes more mobile/available in the environment

(Cundy et al., 2008). The stability and/or solubility properties of the two main valence states of Fe (Fe^{2+} and Fe^{3+}) are predominantly controlled by pH and redox conditions.

Redox transformation between Fe^{2+} and Fe^{3+} are of major importance in biological and element cycling processes (Kappler and Straub, 2005; Cundy et al., 2008; Taylor and Konhauser, 2011). Redox cycling of iron is intimately linked to other elemental cycles (i.e nitrogen, sulphur) on both local and global scales (Taylor and Konhauser, 2011). Iron precipitate mineralisation can form in a large variety of environments surface/subsurface, oxidising/reducing and acidic/basic. Each environment can form a wide variety of Fe mineral species that are unique to the chemistry of each situation. Common surface Fe minerals are shown in Table 2.2, these Fe-rich species are classified in the following groups, native Fe, oxides/hydrated oxides, carbonates, phosphates, sulphates, sulphides and silicates.

Table 2.2 – Common Fe-bearing minerals present in surface and near-surface environments table modified from Cundy et al. (2008)

Mineral class	Name	Formula
Native or metal form (rare)	Zero-valent iron (ZVI)	Fe
Oxides/hydrated oxides	Hematite	α-Fe_2O_3
	Maghemite	γ-Fe_2O_3
	Magnetite	Fe_3O_4
	Goethite	α-FeO·OH
	Lepidocrocite	γ-FeO(OH)
	Ferrihydrite	$Fe_2O_3 \cdot \frac{1}{2}H_2O$
	Green rusts	Fe(II-III)
		hydroxysalts,
		general formula:
		$[Fe^{II}_{(1-x)}Fe^{III}(OH)^2]^{x+}\cdot$
		$[(x/n)A^{n-}\cdot(m/n)H_2O]^{x-}$,
		where x is the ratio
		$Fe^{III}/Fe_tot\cdot$
Carbonates	Siderite	$FeCO_3$
	Ankerite	$Ca(Fe, Mg, Mn)(CO_3)_2$
Phosphates	Vivianite	$Fe_3(PO_4)_2 \cdot 8(H_2O)$
	Strengite	$FePO_4 \cdot 2(H_2O)$
Sulphates	Hydrated	$FeSO_4 \cdot 7H_2O$
	ferrous	(melanterite form)
	sulphate	
	(copperas)	
	Schwertmannite	Ideal formula $Fe_8O_8(OH)_6SO_4$
		but may range to
		$Fe_8O_8(OH)_{4.5}(SO_4)_{1.75}$ (Bigham et al., 1996b)
		or may have formula $Fe_8O_8(OH)_6SO_4 \cdot nH_2O$
		where n= a variable number of H_2O attached (Bibi et al., 2011)
	Jarosite minerals	M $n(Fe^{3+})_6(SO_4)_4(OH)_{12}$
		where M may be K, $(NH4)^+$, Na, Ag or Pb
		and where n=2 for monovalent cations and 1
		for the divalent cations (Frost et al., 2006)
Sulphides	Pyrite	FeS_2
	Marcasite	FeS_2
	Pyrrhotite	$(Fe,Ni)_{1+x}S$
		(where X = 0 to 0.11)
	Greigite	$Fe^{2+}Fe^{3+}_2S_4$
Silicates	Berhierine	$(Fe^{2+}_4Al_2)(Si_2Al_2)O_{10}(OH)_8$
	Chamosite	$(Fe^{2+}_5Al)(Si_3Al)O_{10}(OH)_8$
	Greenalite	$Fe^{2+}_6Si_4O_{10}(OH)_8$
	Glauconite	$KMg(FeAl)(SiO_3)_6 \cdot 3H_2O$

Since White Island has concentrations of dissolved Fe ranging from 0.05 to 12,110 mg/L and sulphur ranging from 660 to 37,612 mg/L (Table 2.1), it is likely that Fe sulphides/sulphates minerals will be forming in addition to the Fe-oxides/hydrated oxides commonly seen in most surface environments as shown in Table 2.2. Figure 2.4 shows the formation pathways (chemical reactions) related to a epithermal source (Reaction 1.1) that is acidic and rich in Fe and S (like the epithermal system seen at White Island). The likely reaction paths are shown for both chemical and microbial, oxidation/reduction of Fe into Fe-rich minerals, oxyhydroxides (Reaction 1.4.1 goethite), hydroxysulfate(s) (Reactions 1.4.2 copiapite, 1.4.3 jarosite and 1.4.4 schwertmannite,). The oxidation of Fe^{2+} to Fe^{3+} Reaction 1.2 (oxidation Fe^{2+}) uses acidity to form the oxidised Fe^{3+}, whereas, the reactions forming Fe-rich precipitates (Reactions 1.4.1 to 1.4.4) all generate acidity.

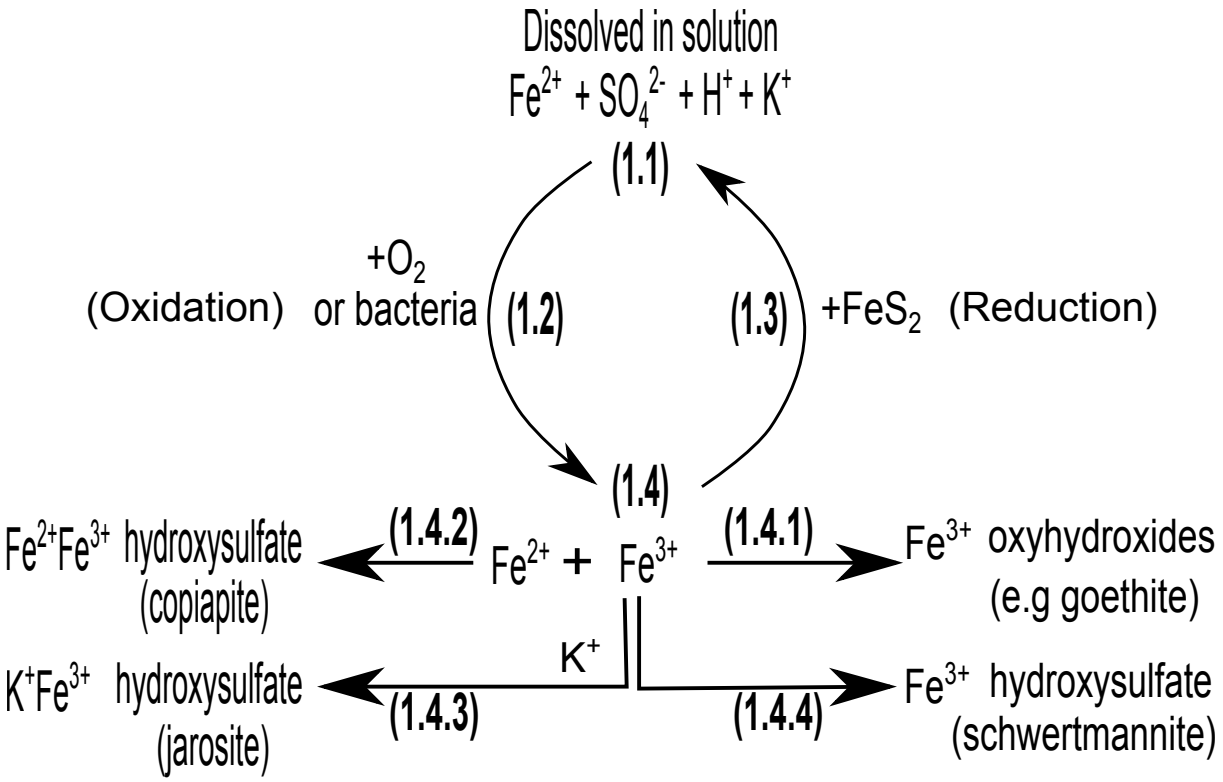

(Reaction 1.1) Initial solution $\longrightarrow Fe^{2+} + SO_4^{2-} + H^+ + K^+$

(Reaction 1.2) $Fe^{2+} + 0.25\,O_2 + H^+ \longrightarrow Fe^{3+} + 0.5\,H_2O$

(Reaction 1.3) $FeS_2 + 14Fe^{3+} + 8H_2O \longrightarrow 15Fe^{2+} + 2SO_4^{2-} + 16H^+$

(Reaction 1.4) $Fe^{3+} + 3H_2O \longrightarrow Fe(OH)_3 + 3H^+$

(Reaction 1.4.1) $Fe^{3+} + 2H_2O \longrightarrow FeOOH + 3H^+$

(Reaction 1.4.2) $4Fe^{3+} + Fe^{2+} + 6SO_4^{2-} + 22H_2O \longrightarrow Fe^{2+}Fe_4^{3+}(SO_4)_6(OH)_2.20H_2O + 6H^+$

(Reaction 1.4.3) $3Fe^{3+} + K^+ + 2SO_4^{2-} + 6H_2O \longrightarrow KFe_3^{3+}(SO_4)_2(OH)_6 + 6H^+$

(Reaction 1.4.4) $8Fe^{3+} + SO_4^{2-} + 14\,H_2O \longrightarrow Fe_8O_8(OH)_6(SO_4) + 22H^+$

Figure 2.4 – Modified from schematic diagram showing the steps in pyrite oxidation and possible secondary Fe minerals in Bigham and Nordstrom (2000) to show the possible precipitation paths from solution to secondary mineralisation hydrothermal water

The oxidation pathway in this case forms Fe precipitates, whereas, the reduction pathway puts elements back into solution. The fluid pH and SO_4 concentration largely controls the precipitation of ferrihydrite, schwertmannite, goethite and jarosite (Kawano and Tomita, 2001). It is possible that other Fe-rich minerals are forming since the White Island sites hydrothermal fluids carry a large variety of other dissolved elements (see Appendix C).

2.6 Microbes and Fe precipitates

Microbes are found in almost all environments on Earth, from black smokers in the depths of the Atlantic to the Antarctic ice shelf (Amils et al., 2007). Microbes can take advantage of natural geochemical processes or directly interact with rock and sediments to suit their nutrient and/or energy needs (Fortin and Langley, 2005; Konhauser et al., 2011; Southam, 2012). Microbes (prokaryotes) are capable of respiring a variety of compounds with a favourable redox potential (Nealson et al., 2002; Southam, 2012). As a result of being able to utilise geochemical redox energy pathways, microbes have become intimately connected to natural geological reactions and cycles of the Earth (Nealson et al., 2002). Mineral precipitates including Fe-rich precipitates can actively (i.e., oxidisation of Fe^{2+} to Fe^{3+}) and/or passively (i.e., biological surfaces can act as nucleation sites) form through microbial interactions (Greenwood et al., 2013).

Microbes can gain energy for growth by oxidising or reducing Fe or S (Kappler and Straub, 2005). These microbial redox interactions can mobilise or deposit Fe in the environment. Lithotrophic ("rock eating") microbes can speed up the release of Fe^{2+} by accelerating the oxidative dissolution of the pyrite (Johnson and Hallberg, 2003). Other species of microbes can directly oxidise Fe^{2+} to Fe^{3+} and use the gained electron as energy for metabolic processes, this forms Fe-rich precipitates as a by-product.

Iron metabolising microbes have a preference for particular chemical and redox enviroment(s). They need a redox environment that keeps Fe^{2+} (potential source of metabolic energy) in solution. Acidic or low O_2 environments are preferred due to Fe^{2+} being the dominant oxidation state found in both acidic and reducing environments. The main reason for the redox preference is that microbes cannot compete with abiotic oxidation at near neutral, oxygenated environments (Taylor and Konhauser, 2011). Many different species of Fe-rich precipitates have been observed forming in acidic SO_4^{2-}-rich hydrothermal waters due to microbial influence. Biomineralized phases of ferric iron have been found forming at Yellowstone (United States);(Kozubal et al., 2012) and Waiotapu hydrothermal sites (New Zealand);(Jones and Renaut, 2007). Some of the minerals include ferric oxyhydroxides, k-jarosite, goethite, hematite, schwertmannite, lepidocrocite and scorodite depending on geochemical conditions (Kozubal et al., 2012; Jones and Renaut, 2007).

2.7 Life on White Island

The identification and categorisation of the microbial activity on White Island is still a work in progress. Many studies have found both prokaryotes (archaea, bacteria) and eukaryotes (diatoms, algae) in sediment and water samples around the Main Crater (Donachie et al., 2002; Butterworth, 2004; Ibáñez–Peral, 2008; Burns et al., 2009). The majority of the microorganisms investigated at White Island are previously uncultured species, but many are closely related to microbial species from other acidic S-rich hydrothermal sites (Donachie et al., 2002). Some of the prokaryotes identified at White Island are closely related to known (or suspected) S and Fe metabolising microorganisms (Burns et al., 2009). There are therefore species of microbes in the sediment and water of White Island that may contribute to the formation of the Fe-rich layers.

Chapter 3: Materials and methods

3.1 Field sampling and investigation

Mapping and field work was undertaken at White Island, New Zealand, during June 2012 and May 2013. The field area is confined to the Main Crater and the sampling sites were within the Eastern and Central subcraters shown in Figure 2.2. The field work undertaken during June 2012 was to identify potential Fe-rich precipitate deposits and to conduct preliminary site investigations and sampling. The May 2013 field work was done to fully investigate identified Fe-rich deposit sites via mapping, soil/regolith profile examinations and sample collection. Gloves were worn during the collection of all samples and all implements were cleaned between use to reduce potential cross contamination of collected samples. Site investigation and collected sample site positions were logged using a Garmin GPSMAP 62s (GPS). Temperature measurements were all taken using a Fluke Laser thermometer (model 62 Mini IR Thermometer). The samples were stored in taped and labelled plastic bags.

3.2 Rock and sediment samples

Sediment and rock samples were prepared for different analysis methods. Slides of subsurface Fe-rich layers were prepared for petrological, EDS and Raman analysis methods through the Department of Geology, University of Canterbury. Both polished and unpolished thin sections were prepared and the thin sections were left uncovered. The XRD, XRF and carbon analysis, rock and sediment samples were prepared by drying at $\leq$50℃ for a minimum of 24 hrs. Then the samples were ground to a fine powder using a mortar and pestle or ring mill, which were cleaned between samples and the powders were stored in glass bottles at room temperature.

3.3 Scanning electron microscope (SEM) sample preparation

The method used for sampling was designed to limit contamination, all instruments used for sampling were washed with ethanol and cleaned between use and gloves/mask/hat were worn while sampling to limit potential contamination sources. The rock and sediment samples were taken in the field at each deposit and directly transferred into sterile glass bottles filled with a solution of 10% ethanol, which was increased to 20% within 2 hours of sampling. The approximate sample size taken at each site was 0.5 cm in diameter for rock and a few grams for sediment and duplicate samples were taken (3-5 samples at each site). Before the samples could be used for critical point drying (CPD) they were

dehydrated by increasing the solution surrounding the samples from 20% to 100% ethanol solutions. This was done by removing a 5ml-15ml of solution surrounding the sample with a pipette and adding the amount of ethanol needed to increase the solutions concentration by 10% increments. The solution was mixed by lightly swirling the solution in the bottle. Once the solution was mixed the samples were allowed to equilibrate for at least 1 hour before increasing to the next concentration of ethanol. When the sample solution was at 100% ethanol, the same was done with Amyl Acetate (AA) replacing the ethanol with AA. Once the samples are in a solution of 100% AA they are considered to be stable and can be left in the solution until the samples could be dried in the CPD using liquid CO_2. The CPD model used was a Polaron E3000 series II.

Two types of sample type taken in the field unconsolidated (clays, loose sediments, microbial filaments) and consolidated rock. Both were treated slightly differently during drying and mounting. Loose sediments/clay and microbial samples were diluted and then floated onto gold plated glass cover slips, then dried in the CPD. Floating consists of shaking the loose sediment sample to suspend the sediment in solution, which a 15ml pipette sample is transtered to a new test tube. This new sample is diluted by adding 15ml of AA (dilute by approximately 50%). This is done up to four times and each resulting solution is transferred onto the gold/palladium coated glass slides by pipette, while the sediment is suspended in solution. This crates a thin uniform coating of sediment across the plated glass slides. The consolidated samples were dried without any extra processing. The samples were mounted and coated with gold/palladium using a sputter coat method.

3.4 SEM with Energy-dispersive x-ray spectroscopy (EDS)

The microscope used was an JEOL JSM 7000F field emission, high resolution scanning electron microscope (SEM). The SEM was used with standard operating protocols. Images were saved in a tiff format with information about operating mode, voltage, magnification, scale bar and WD (working distance) included on each image. Polished slides were analysed using Energy-dispersive x-ray spectroscopy (EDS) attachment on the SEM. This was done to provide information about Fe-precipitate and mineral chemistry. Point analyses and element mapping were completed; however, carbon percentages were not recorded, as the slides were carbon coated.

3.5 Binocular microscope

Uncut sections of rock and slides were looked at using a Meiji EMZ-8TRD stereomicroscope with a Infinity 1 camera and Capture software. A series of pictures were taken to investigate internal features in the subsurface Fe-rich layer(s), to help with identifying structure(s), texture(s) and composition associated with the Fe-rich subsurface layer(s). Close attention was given to identifying vesicularity, weathering, mineralogy and colour

changes within the samples.

3.6 Petrology

Thin sections of subsurface Fe-rich precipitate layers were used for petrographic analysis of the crystals, groundmass and the precipitates. The microscope used was MEIJI polarising microscope model MT 9200 and the system used to take digital images of thin sections in transmitted light was a Leica DM 2500P petrological microscope with a Leica DFC295 camera and LAS software package. ImageJ 1.47v programme was used to estimate the percentage of Fe-rich precipitates and other minerals as well as pore space at specific sites, from petrographic images (Rasband, W.S., ImageJ, U. S. National Institutes of Health, Bethesda, Maryland, USA, http://imagej.nih.gov/ij/, 1997-2012).

3.7 X-ray diffraction (XRD) and X-ray fluorescence (XRF)

X-ray diffraction and XRF was completed at the Department of Geological Science, University of Canterbury. The rock and sediment powders were analysed using a Philips PW1820/1710 X-ray Diffractometer to identify the crystalline components present in the samples and by a Philips PW2400 Sequential Wavelength Dispersive X-ray Fluorescence Spectrometer (XRF) to determine bulk element concentrations including sulphur.

3.8 Raman spectroscopy

Raman analysis was conducted at the Department of Chemistry, University of Otago, New Zealand. A polished slide and a rough cut rock section from sample NW 5b was used in analysis. Thirty seven sites were tested on the polished slide and 28 sites were tested on the rough cut rock sample to obtain sufficient Raman spectra data for analysis. The Raman spectra were recorded using a Senterra dispersive Raman microscope (Bruker Optics, Ettlingen, Germany). Both 532 nm and 785 nm diode laser frequencies were used on samples at 25 mW, 50mW and 100 mW before the objective was focused by a 20x lens with an aperture of 50x1000μm.

Each spectrum set was collected for 5 seconds with 10x coadditions (spectra data was collected from sample site 10 times then added together and averaged), data were collected between 0 and 4440 cm^{-1} at 1 cm^{-1} resolution. Software used to analyse and manipulate the data was Opus Version 6.5 Build:6,5,92 (20080204) Bruker Optik GmbH 1997-2007. The spectra range in the data set was between 90-1500 cm^{-1}. The reference data used for analysis were downloaded from the RRuff Projects Data Base (Downs, 2006).

3.9 Carbon isotope chemistry

The rock/sediment samples used for carbon analysis were ground as described in sample preparation Section 3.2. Three types of sample were created out of the ground rock/sediment samples: (1) total carbon (undigested/unmodified ground sample), (2) inorganic carbon removed (ground sample digested using HCl), (3) all organic carbon removed (ground sample digested using HCl then hydrogen peroxide removing organic carbon). This was done so the total carbon in the rock/sediment could be compared to samples with inorganic and organic carbon. During the rest of the document and analyses, the three samples types will be reclassified as (1) total carbon (2) organic carbon (3) residual carbon.

A small amount (≈15 grams) of homogenised undigested powdered rock/sediment was transferred to a sterile glass vial as the (1) total carbon sample. Then an ≈30 gram amount of homogenised undigested powdered rock/sediment sample was digested in 0.5 molar HCl to remove inorganic carbon. The sample temperature was incrementally increased (5 to 10℃) from ambient to ≤50℃ while adding fresh HCl. This addition of heat and acid was done as the reaction stopped/slowed. Once the samples stopped reacting, they were left in solution for an additional 24 hours before centrifuging.

The centrifuging method used to remove the supernatant liquid. The samples were washed into to 50ml centrifuge tubes with distilled water and shaken for at least 1 minute to homogenise the suspension. Then the sample was centrifuged at 1500rpm for 10 minutes, this was repeated 5 times for each sample. The centrifuge tubes were refilled with distilled water and shaken and left to sit for 10 minutes after each removal supernatant. The samples were then dried at ≤50℃ and split in half, half was used as (2) organic carbon sample and the other half of the sample was digested using 50% hydrogen peroxide instead of HCl. The same method was used as in HCl digestion, resulting in the (3) residual carbon sample.

During the preparation of the White Island samples for carbon analysis, it was found there was a loss of mass during the HCl and hydrogen peroxide digestion stages. The loss of mass was most likely due to material becoming soluble during treatment and being washed out during the centrifuging stage of preparation. This will effect the accuracy of the total carbon (by mass) for each sample. The HCl and hydrogen peroxide digestion methods were done again with new samples and the loss of mass was measured to help create a correction factor for the total carbon (by mass).

It was also noticed that the White Island samples are highly reactive to hydrogen peroxide. The samples were still reacting after 5 weeks, it was decided to use the samples for analysis even though they were still reacting, because the carbon was most likely

gone and another reaction was occurring. The unknown reaction has caused some carbon enrichment in the (3) residual carbon samples, through either loss of mass or fixing of atmospheric CO_2 into the samples. The samples were tested with HCl after treatment, but did not react showing that its unlikely to be CO_2 is being fixed back into the (3) residual carbon samples.

Samples from each site and treatment method were run three times to check the homogeneity of sample and to check that the results be replicated. All samples were analysed for their carbon weight percentage and $\delta^{13}C‰$ values using the University of Canterbury's Costech Elemental Combustion System (ECS) 4010 and the Thermofinningan Delta V+ Gas Isotope Ratio Mass Spectrometer (GIRMS). Conflow III was used to control gas flow between the ECS and GIRMS. The $\delta^{13}C$ values were determined (of CO_2) by combusting samples at 1080℃, under continuous flow of ultra-high purity (99.9999%) helium. An empty autosampler well was left between every sample during analysis to ensure the signal of each sample was not contaminated by residual combustible material of adjacent samples. Percentage of carbon by mass and volume were determined by measuring the yield of precisely massed (±1 mg) certified reference materials of known carbon content.

3.10 Water samples

Water samples were obtained from creeks for pH, Eh measurements and for ICP-OES analysis. Sample locations are shown in Figure 3.1 and Table 3.1 describes the water collection protocol used. The Eh and pH analyses of water samples were completed within 5 hours of collection. The pH/Eh meter used was a Mettler Toledo SevenGo Duo pro pH/Ion/Cond with meter heads, Mettler Toledo Inlab® Expert Pro-ISM-IP67 pH 0-14, 0-100℃ and Mettler Toledo Inlab® 738 ISM Conductivity NTC 30kΩ 0.01-1000mS/cm, 0-100℃. The pH meter was re-calibrated using standard pH 4.01 and 7.00 buffer standard solutions before use and was regularly calibrated with standard buffered solutions.

Table 3.1 – Description of water sampling method used at White Island.

1	Clean sterile 50ml sample centrifuge containers were used for the sample collection
2	Two water samples were taken at each site, one to be used for Eh, pH measurements and the other for ICP-OES analysis
3	The containers were washed in the sample water and then filled in the fastest section of the stream and capped underwater to reduce the amount of trapped air in sample
4	Parafilm was wrapped around the lids to create a airtight seal and the samples were stored for transport

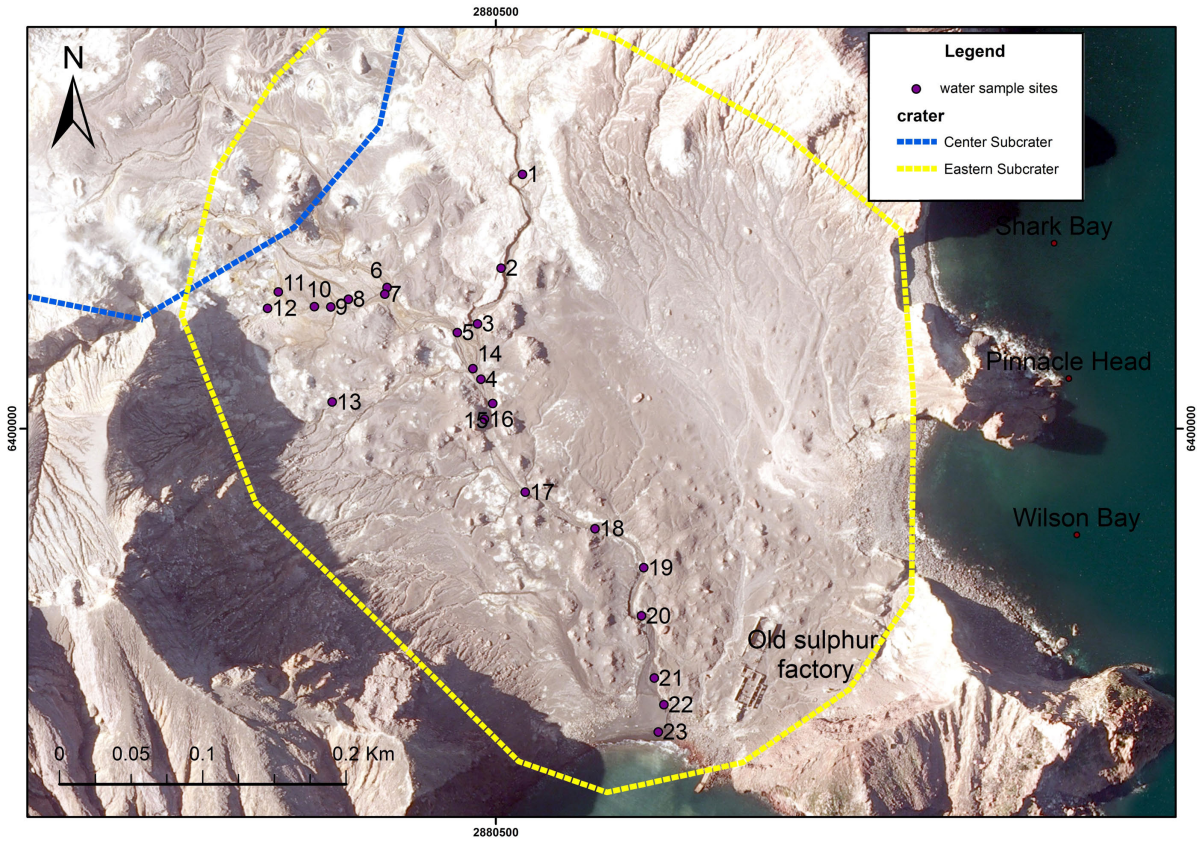

Figure 3.1 – Orientation map showing all sites where water samples were taken during May 2013. (Map data sources see Appendix A).

The samples being used for ICP-OES were filtered using 0.2μm syringe filter. This was done to remove any sediment, which would potentialy damage the ICP-OES analyser. The filtered water was transferred to clean, sterilised 50ml centrifuge containers with lids and sealed with Parafilm inorder to stop atmospheric gases interacting with the water samples. The samples were stored at room temperature until they were analysed at Lincoln University, Canterbury, New Zealand, using a Varian 720-ES Inductively Coupled Plasma Optical Emission Spectrometer (ICP-OES) fitted with an SPS-3 auto-sampler and ultrasonic nebuliser.

3.11 Geochemical modelling methods

Two different programmes were used to investigate the geochemistry and pathways of Fe precipitate formation. PHREEQC version 3 (Parkhurst and Appelo, 2013) was used to investigate speciation and the Saturation Indexes (SIs) of potentially forming Fe-rich minerals sulphur and gypsum, under different pH, Eh and temperature conditions. The wateq4f.dat database was used as it has Fe and jarosite speciation available. The Phree-Plot programme (Kinniburgh and Cooper, 2014) was used to create a series of Eh and pH diagrams to help predict the conditions required for precipitating specific iron mineral species.

The GGW database and field measurements of pH, Eh and element concentrations were used to provide information for computer modelling of the formation pathways of minerals. The various data was compiled and used to confine the range(s) of pH, Eh, chemistry, temperature(s) commonly seen at White Island in order to create models to investigate the formation of precipitates. Creek data was used as a proxy for the subsurface environment since the creeks are all being fed by subsurface geothermal sources.

A synthesis of data sources was used to narrow the minerals considered including PHREEQC geochemical simulations based average concentrations, Eh, pH and temperatures from collected water data, atmospheric O_2 set at 1 bar. Simulations were run to see what minerals were potentially precipitating forming in solution. Results from field observations and geochemical results were additionally used to help narrow the Fe-rich minerals considered in geochemical modelling.

Schwertmannite was added into the phreeqc/phreeplot calculations of SI and Eh pH mineral stability plots using the following information. Other log_k and delta_h values from other papers and databases were evaluated, the values below were used in the final geochemical models.

Schwertmannite

$Fe_8O_8(OH)_6(SO_4) + 22H^+ = 8Fe^+3 + 14H_2O + SO_4^{-2}$

log_ k 18 # from Bigham et al. (1996b), the log_k is quoted as $18^+_-2.5$

delta_ h -823.3 kJ # from Majzlan et al. (2004)

Chapter 4: Results

4.1 Field sampling and observations

Figure 4.1 shows all the sites where samples and observations were collected. Table 4.1 lists the type of analysis completed on the samples taken at each site and notes if Fe-rich subsurface layers were present. A full sample catalogue is in Appendix E. At some of the sites multiple samples were taken, whereas, at other sites only observations and photos were taken. Sites 1-4 (sample numbers NW 1 - NW 6) were collected in 2012, sites 5 - 26 (sample numbers NW 7 - 17 and carbon samples) were collected in 2013. After the initial analysis of the 2012 samples, the sampling during 2013 focused on identified Fe-rich subsurface sites.

An image taken from site 20 (see Figure 4.1) is shown in Figure 4.2. The panoramic view shows the field area including the landing site (left hand side), crater lake (centre right), to the higher crater surface of the Eastern subcrater (right hand side). Some key sites are marked on the image for orientation purposes (i.e., sites where Fe-rich subsurface bulk samples were taken from 2,5,11,21). Many of the low flow creeks between the boat and site 2 have thin Fe-rich layers coating the creek beds, as well as abundant microbial fibres/mats. Iron-rich clays were found at site 3 and at site 4, large amounts of white and yellow precipitates were found suspended in water outflowing from a large spring. Site 25, has a 1-3 cm thick, finely laminated Fe-rich layer coating base of hot outflow. The colours in the sediments and creeks around the outcropping subsurface Fe-rich layers are rusty yellows reds and browns, as seen in Figure 4.1 between sites 11 and 21. Similar colours and potential layers can be seen in the crater walls, in the old layered/bedded crater fill and lake deposits (centre top area of Figure 4.1).

Several types of Fe-rich deposits are present in the crater surface and subsurface (Figure 4.3). The surface deposits are mostly associated with hydrothermal water(s) depositing precipitates that coat creek sediments (Figure 4.3A), seeps (Figure 4.3B) and outflows (Figure 4.3C). In the subsurface red Fe-rich clays (Figure 4.3D) and Fe-rich subsurface deposits (Figures 4.3E,4.3F) are prevalent. Microbial colonies fibres/mats and algae are present in the creeks around the area of forming Fe-rich precipitate layers and above the creek layers. These observations support that microbial activity is present around the zones of Fe formation.

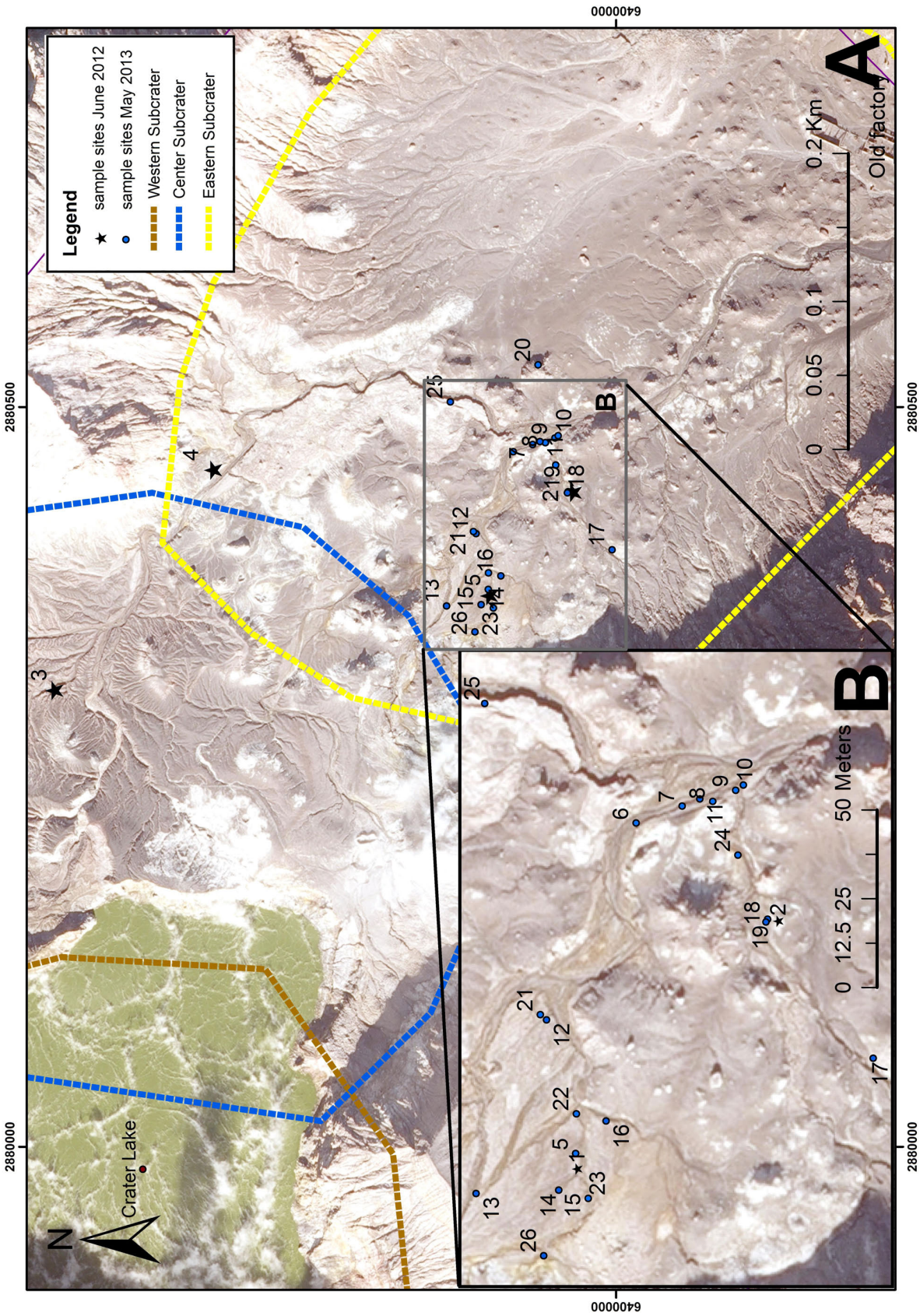

Figure 4.1 – Orientation map showing all sample and observation sites 2012-2013, A) Shows the full field area (2012), B) Main focus area during 2013 where all subsurface deposits were found within this boundary. (Map data sources see Appendix A).

Table 4.1 – Analyses conducted at each site and if Fe-rich subsurface layers are present

Site	SEM sample	Rock/sediment samples	Carbon samples	Subsurface Fe-rich layer
1	✓			
2	✓	✓		
3	✓			
4	✓			
5	✓	✓	✓	✓
6				✓
7				✓
8				✓
9				✓
10				✓
11	✓	✓		✓
12				✓
13	✓	✓		
14				✓
15				✓
16				✓
17				
18				✓
19				✓
20				
21	✓	✓	✓	✓
22	✓	✓		✓
23				✓
24	✓	✓		✓
25	✓	✓		
26	✓			

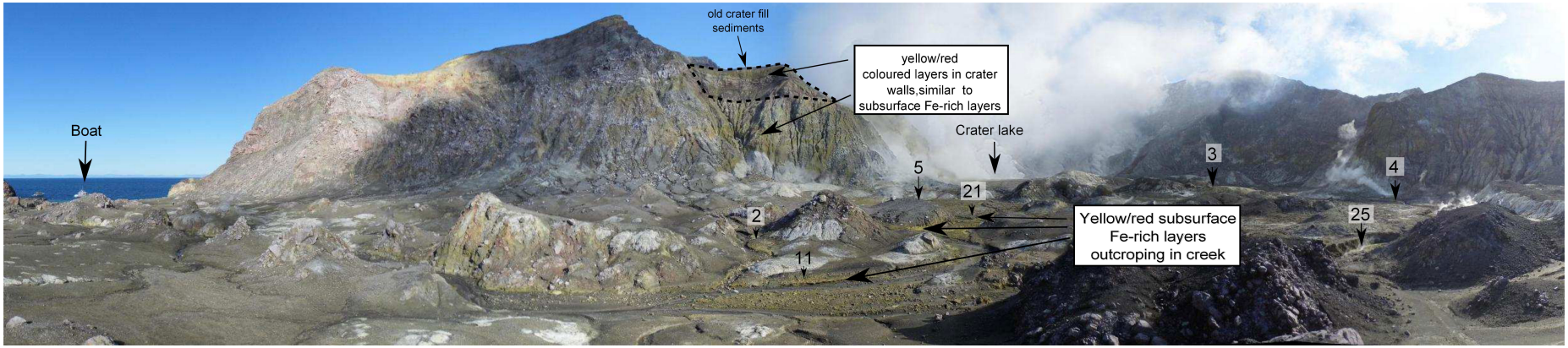

Figure 4.2 – Image of the field area showing western side of crater (taken from site 20).

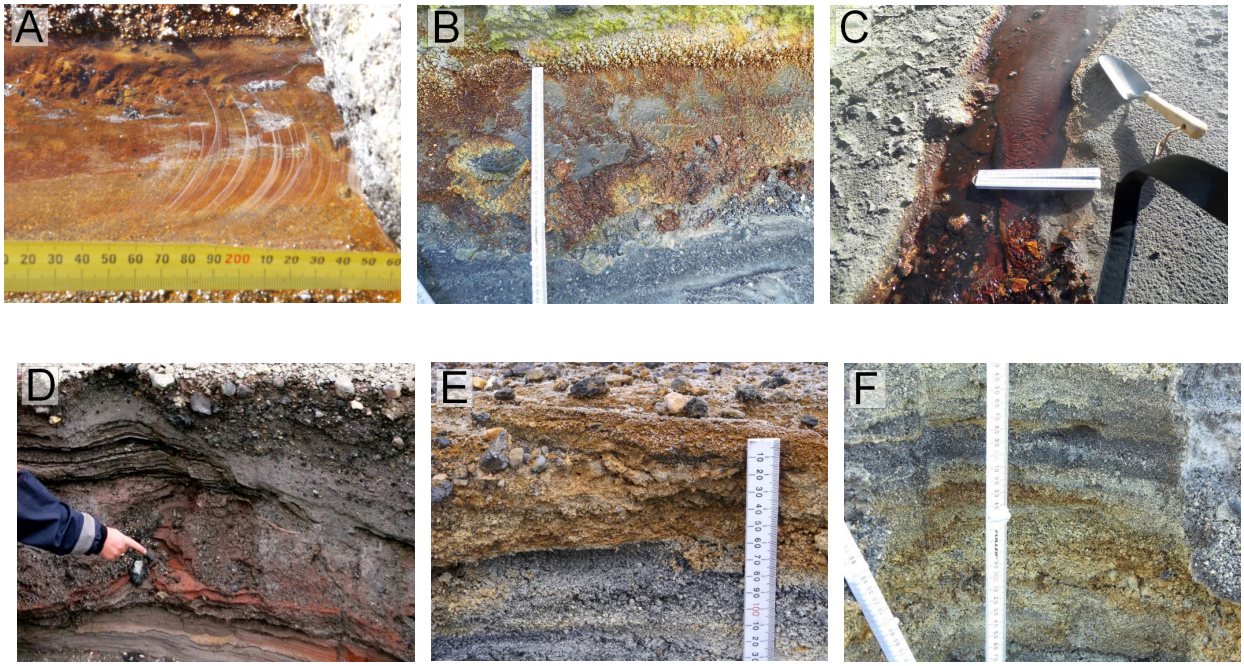

Figure 4.3 – (A) Thin Fe layer coating creek, white microbial fibres floating on the waters surface. (B) Deep red Fe layer and white gypsum crystals precipitating on bank of creek from seep water. (C) Thick red Fe layer coating bottom of hot outflow. (D) Subsurface deep red Fe-rich clay layers in upper crater. (E) Hard well indurated Fe-rich subsurface layer. (F) Soft poorly indurated Fe-rich subsurface layer

The thin Fe layers coating the top of the creek beds (Figure 4.3A) are predominately found in creeks/streams with low flow rates on the western edge of the Eastern Subcrater. The layers are thin (0.5 to 2mm thick) and form a crust over the bottom of the creeks and have a distinctive light brown colour. White microbial fibres are present in the creek water at most sites. The Fe layers coating hot seeps (Figure 4.3B) range in thickness from (1 to 3+mm) and colour from a mid-red to a dark reddish brown. These layers coat the sides of creeks where hot water is seeping out of the sediments. The layers are harder and thicker (2mm to 1+cm) than the thinner iron layers coating the bottom of creeks (Figure 4.3A). Many of the layers are covered in white gypsum crystals. The Fe coating hot outflows (Figure 4.3C) have a similar colour range to the hot seeps but form thicker deposits (0.5-3+cm thick). When the thicker layers are broken, the layers are made up of very fine laminated Fe precipitates.

The subsurface Fe-rich clay layers (Figure 4.3D) are very fine deep red layers ranging from 0.5 to 3cm thick and are mainly found in the upper section of the Centre Subcrater. The layers appear to be volcanic ash that has weathered into clays and are covered with alternating layers of ash, tephra and lapilli, from other eruptions. No large volcanic clasts have been observed in the Fe-rich clay layers. The subsurface Fe-rich precipitate layers (which are the focus of this thesis) range from well indurated, cemented (needed

a hammer to brake and bent one shovel) to soft, cemented (can dig with a shovel). The hard well indurated layers can be seen in the sides of creeks and are exposed as creeks cut through the crater sediments (see Figure 4.4). The maximum distance between identified outcrops of the Fe-rich subsurface is ≈100m long (Figure 4.1 from site 5 to 10) by an ≈25m wide strip. This means the subsurface Fe-rich layer(s) could be forming under an area of 2500m^2. The actual/full extent of the subsurface Fe layers is still unknown since there is between 0.5 to 1.5m of crater fill sediment covering the layers between outcrops.

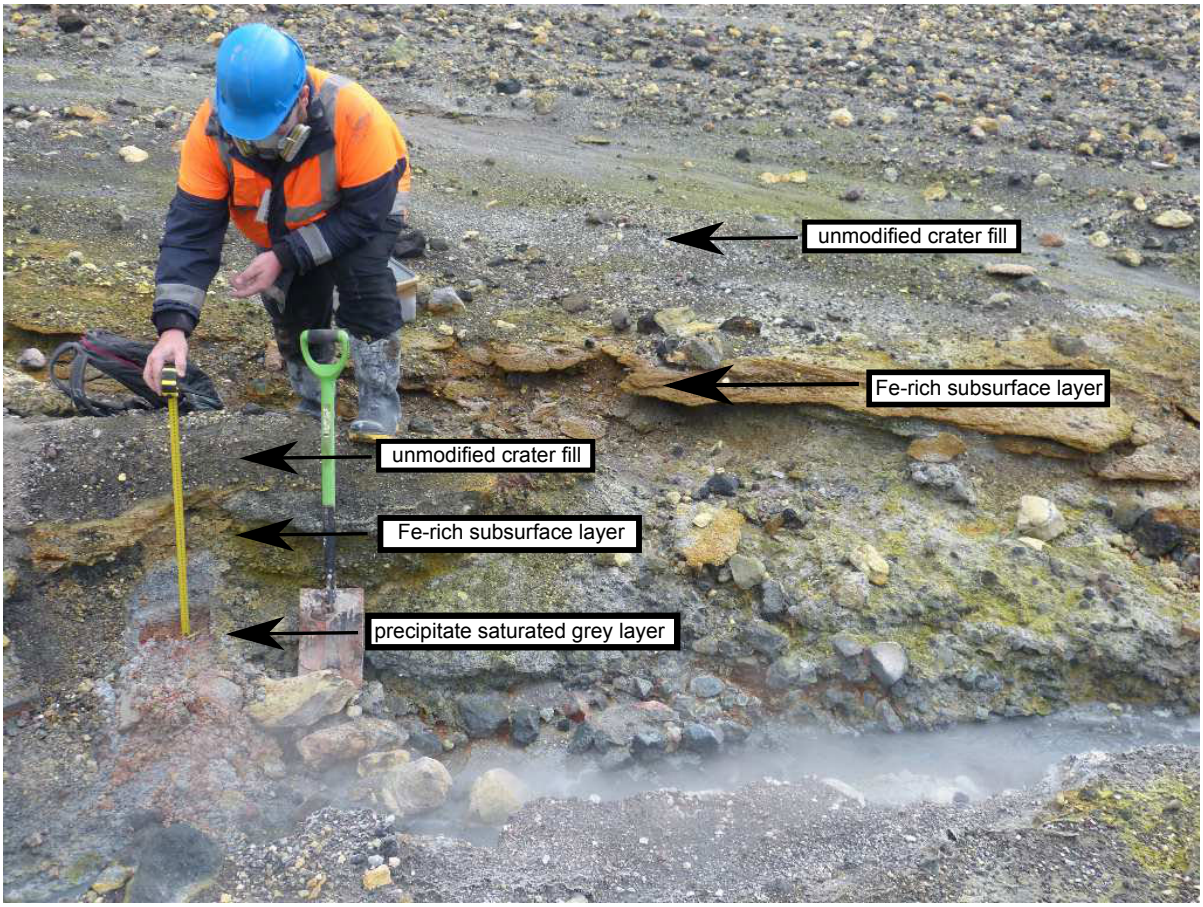

Figure 4.4 – Subsurface Fe-rich layer exposed in creek

The subsurface Fe-rich layers observed in the field range from yellow to red in colour, with some sense of stratification internally. The sediments that are being cemented range from well sorted to moderately sorted and look similar to the deposits above and below the cemented zone. Most of the Fe-rich layers observed are cementing mostly ash to tephra sized clasts together, but there are some larger random bombs and crater wall mixed and cemented in the layers. The precipitates coat and/or infill between the clasts, cementing them into a cohesive layer. At the sites where the Fe-rich subsurface layers have been observed, contain almost no visible precipitates in the crater fill sediments above the leading edge of precipitation (see Figure 4.5). Whereas, below the leading edge a marked change in precipitate content and colour within the sediments happens, the sediments below are saturated with precipitates and fluids (see Figure 4.6). Gases have been observed bubbling out of the saturated sediments at some of the sites.

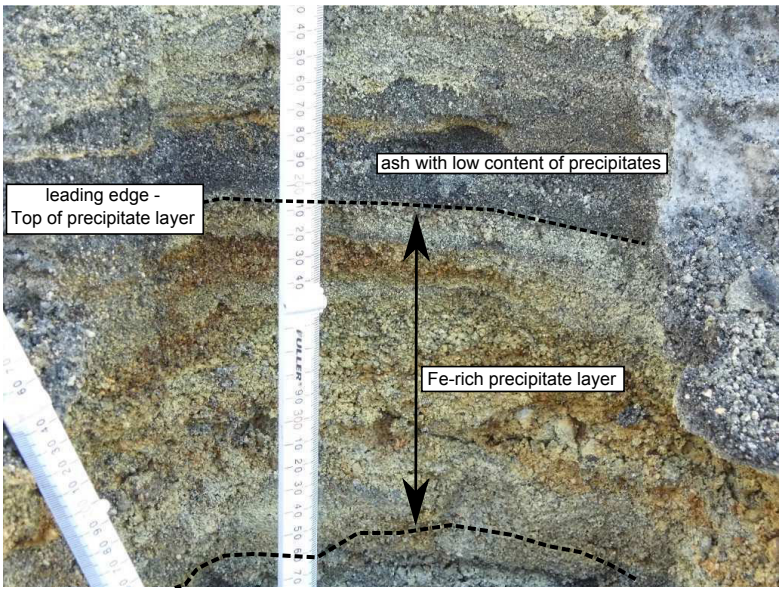

Figure 4.5 – Subsurface Fe-rich layer, leading edge of precipitates and unmodified sediments with low precipitate content

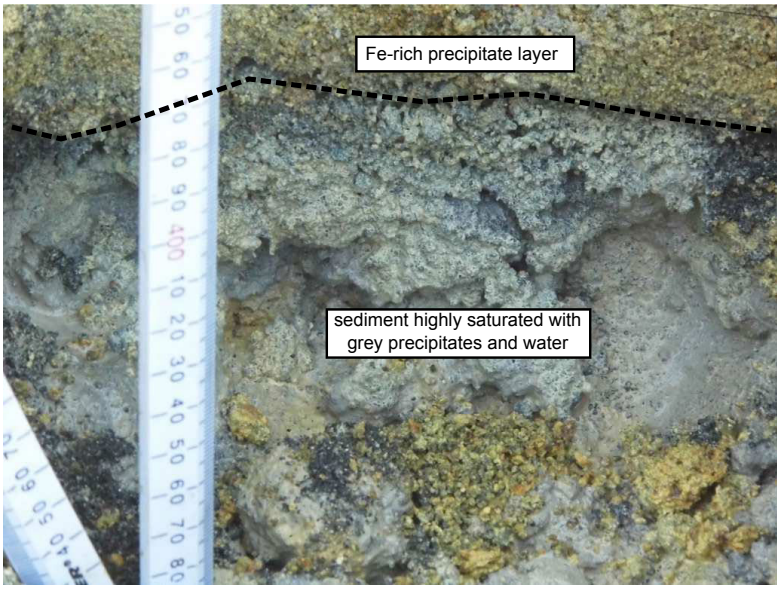

Figure 4.6 – Layer highly saturated with precipitates and water below subsurface Fe-rich layer

At the sites of well indurated Fe-rich layers, the saturated sediments below the Fe-rich layer are hotter than the less saturated sediments above the Fe-rich layer. There appears to be a temperature divide across the Fe-rich layers. The largest temperature change measured across the subsurface Fe-rich layers, was at site 5 (see Figure 4.1). The temperature the base of the Fe-rich layer was 35.0 ℃ and the top of the layer 18.2 ℃. This reduction in temperature of 16.8 ℃ occurred over a distance of 7cm (the thickness of the layer). The temperature reduction is less notable at the soft Fe-rich precipitate sites. The Fe-rich precipitate layers were found to have a temperature range from 22.0 to 35.0 ℃ at the base and a range of 14.0 to 18.2 ℃ at the top of the layers. The creeks around the layers were found to have a average temperature of 47.05℃.

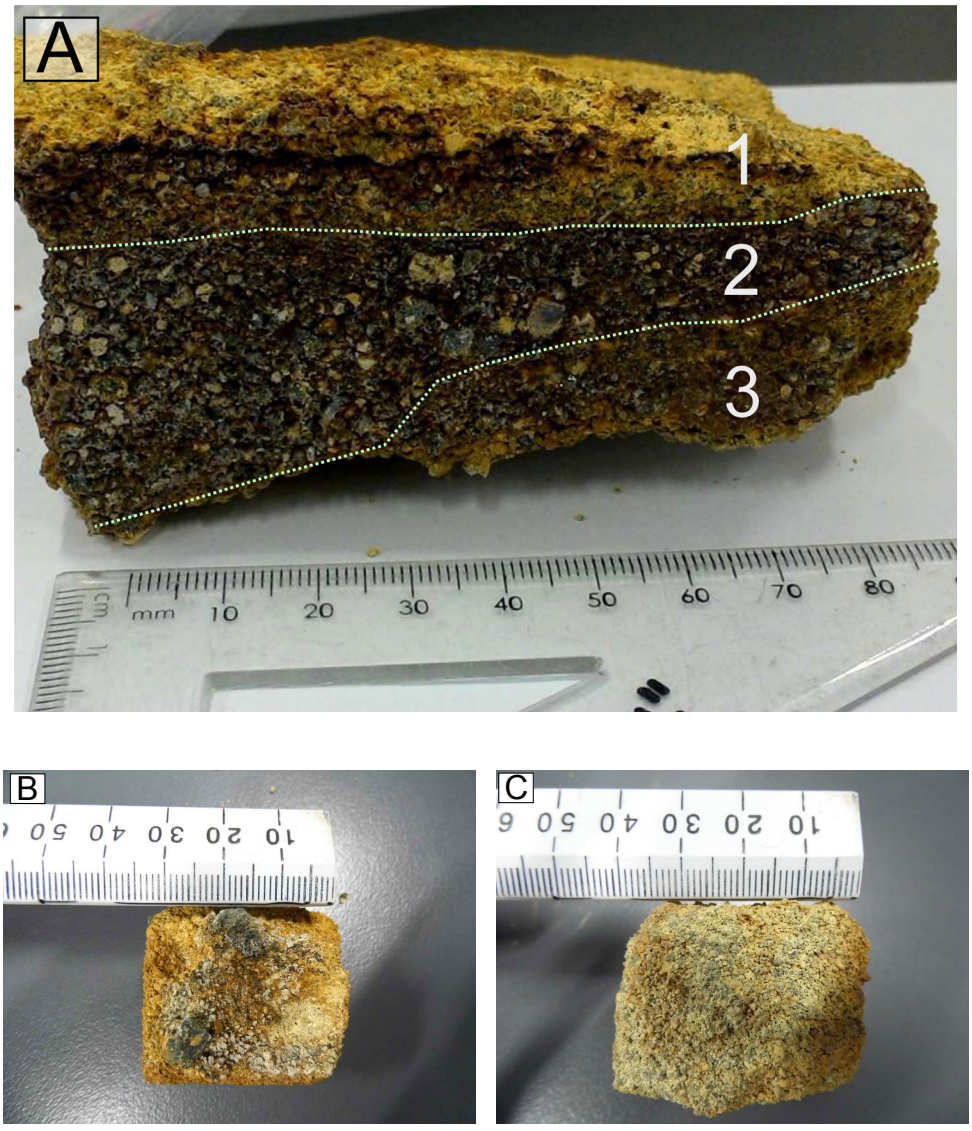

Figure 4.7 – (A) Close up of side of main Fe-rich precipitate layer from site 3 2012 (NW5b)(B) Top view (C) Bottom view

Figure 4.7 is a close up of the subsurface Fe-rich layer, the thickness of the layer at the sample site ranged between (4-7cm) thick. Three zones have been drawn on the side view (Figure 4.7A), 1 and 3 are infilled predominately yellow coloured precipitates. Site 2 has a deep redish colour and open pores can be observed in this section (potently has connected porosity). Less powdery yellow precipitates fill between the clasts in this section. The top and bottom are infilled have a light yellow/orange colouration (Figures 4.7B and 4.7C). The top and bottom of the layer are softer than the central red section of the layer, but overall the layer is very well indurated.

All the observed Fe-rich subsurface layers have similar morphologies and have a range of internal colours ranging from light yellow to dark red/brown. The thickness of the Fe-rich subsurface layers ranges from site to site, from 4 up to ≈50cm thick. The thicker Fe precipitate sites look to be made out of multiple layers. The soft (poorly indurated) sub-

surface Fe-rich layers (shown in Figure 4.3F), tend to less red/deep red coloured sections when compared to the harder well indurated Fe-rich subsurface layers. All of the Fe-rich subsurface layers are cemented by precipitates which coat all the grains in the layers. The dominant grain size in the layers is between ash to medium tephra sized clasts.

4.2 Minerology and geochemistry

4.2.1 Binocular microscope

Under the binocular microscope the Fe-rich subsurface layer is made up of cemented pieces of ash to lapilli sized clasts and has distinct coloured layers. The top section has light yellowish/red colour and the bottom (which is the middle section of the layer) is a dark brownish/red as shown in Figure 4.8. The layer can be split in to two distinct sections by colour (Figure 4.8B). The top light yellow/red layer (Figure 4.8C) has less open pore space visible than darker brownish/red layer (Figure 4.8D). The top and bottom of the Fe-rich layers tends to be in filled and cemented like Figure 4.8C, whereas, the middle sections of the layers are coated and cemented like in Figure 4.8D.

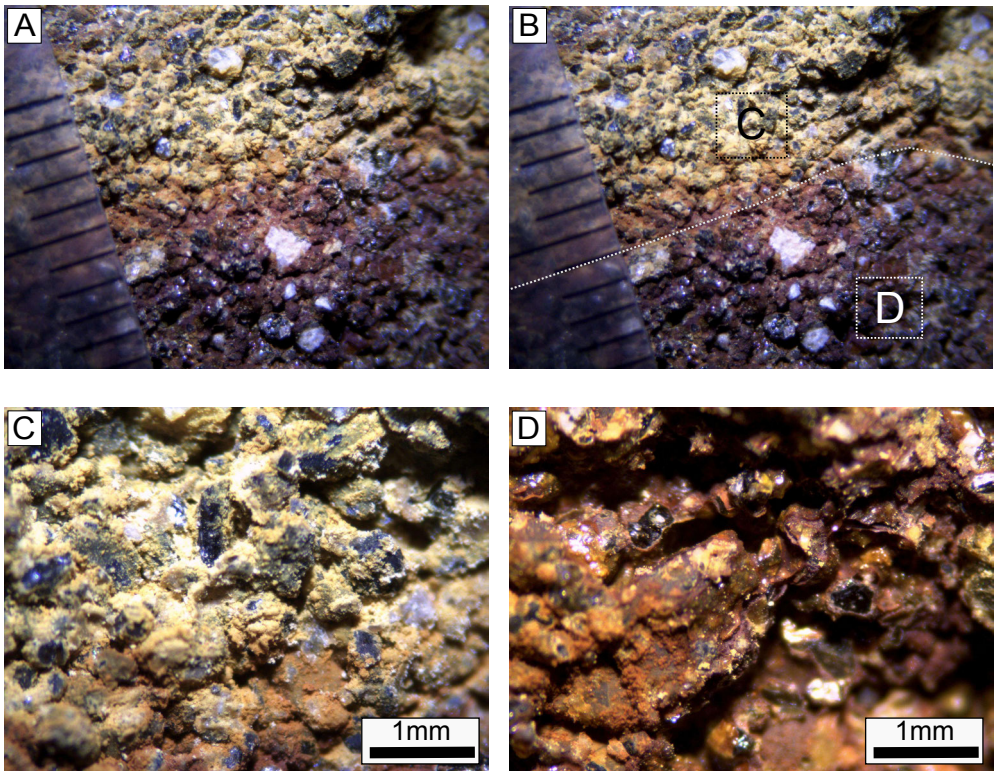

Figure 4.8 – (A) Close up of top and middle of main Fe-rich precipitate layer from site 3 2012 (NW5), scale on left hand side is in 1mm increments, (B) Sites for images C and D and boundary between infilled/open pore layers, (C) Light yellow/red precipitates layer filling in all gaps around tephra/ash sized volcanic ground mass and crystals (D) Dark brownish/red precipitate layer coating all grains, note: there is more open pore space in this section.

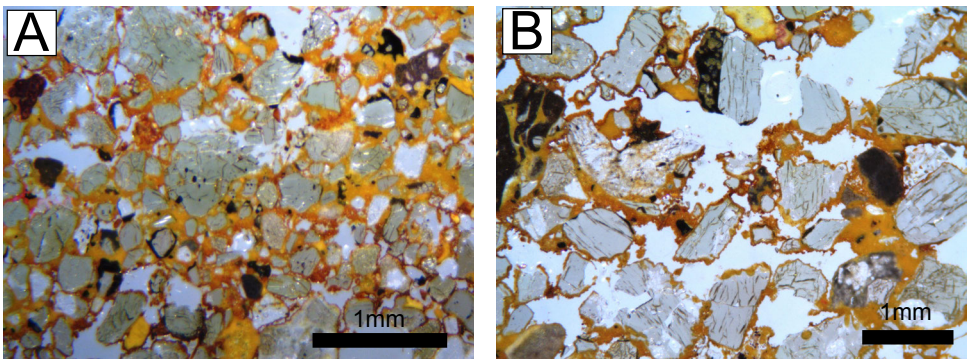

Figure 4.9 – (A) Image of a polished thin section (sample NW5), the area is similar to infilled section observed in Figure 4.8C, (B) section of Fe-rich precipitate (sample NW5), the area is similar to open pore section observed in Figure 4.8D

Figure 4.9 shows polished slide (sample NW5), the bright yellow to orange coloured Fe-rich precipitates infill/surround and cement clasts of volcanic glass and phenocrysts. The sites shown are similar to infilled section and open pore sections identified in (Figure 4.8). Figure 4.9A shows a section similar to site (Figure 4.8C), identified as more infilled and visibly has less pore space than Figure 4.9B. Many of the pyroxenes (the clear crystals) in Figure 4.9B have a dissolved/weathered appearance around the edges and there is very little volcanic glass/ground mass coating some of the individual crystals of pyroxene (Figure 4.10). The area circled in Figure 4.10 is one of many sections of Fe-precipitate that has dark opaque minerals embedded in the precipitate. These dark opaque minerals can be found scattered throughout the Fe-rich precipitate.

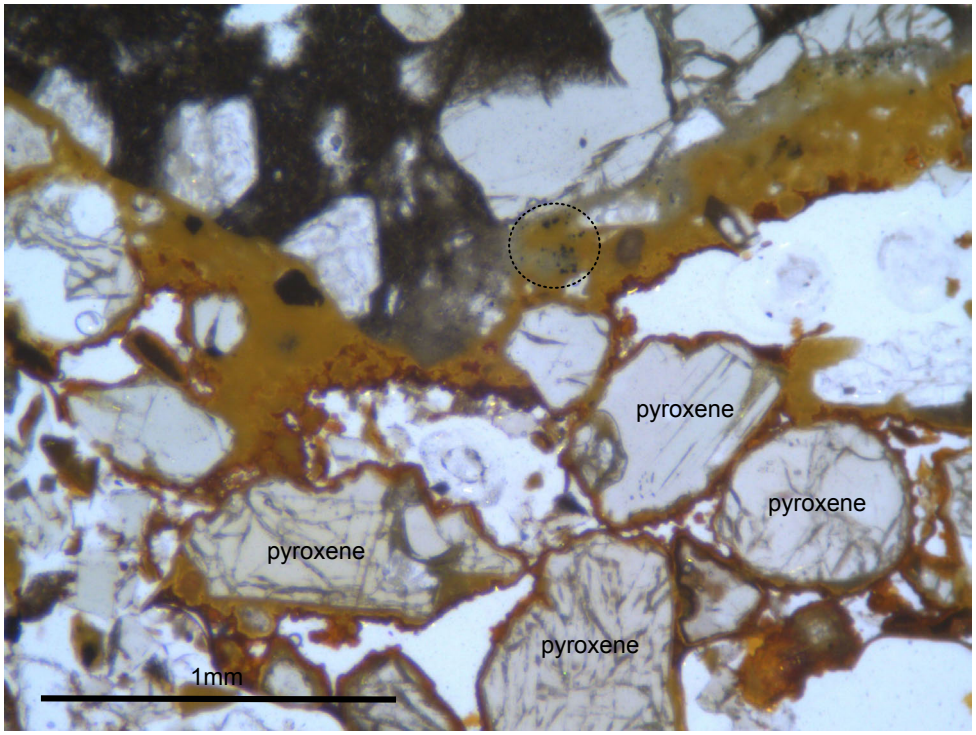

Figure 4.10 – Fe-rich precipitates coating and infilling between minerals (sample NW5). The pyroxenes labelled show potential dissolved edges and the dotted circle shows an area with dark opaque minerals in the Fe-rich precipitates.

4.2.2 Petrology

All the volcanic clasts being cemented by the Fe-rich precipitates are common eruptive products: ash, lapilli, bombs, pieces of lava or crater wall. All the clasts have varying amounts of hydrothermal alteration/weathering and leaching. Many of the observed pyroxene phenocrysts are free of attached volcanic glass/ground mass. The composition of the two layers (infilled/open) as identified in Figure 4.8 and Figure 4.9 are very similar in the minerals, phenocrysts and ground mass that make up each one. The amount of pore space in each zone and the amount of Fe precipitate vary. An analysis of Figure 4.11 and Figure 4.12 using ImageJ, found that the infilled site (Figure 4.11) has 49.48% Fe-precipitates and the more open site (Figure 4.12) has 38.89% Fe-precipitate infilling, coating and cementing the clasts.

All of the slides analysed have phenocrysts of feldspar, pyroxene (both ortho- and clino-pyroxenes) and clasts of volcanic lava made up of glassy or crystalline ground mass. All of the volcanic casts/phenocrysts are coated by amorphous looking Fe-rich precipitates, in less porous sections the precipitates infill between the clasts (blocking porosity). The Fe-precipitates are semi-opaque to opaque minerals which range in colour from muted orange/red to very dark red in colour. Feldspars identified are all plagoclase showing remnants of both twinning and zoning despite alteration. Some feldspars have been replaced in sections by amorphous silica and/or clay minerals. The pyroxenes have fractures and other features that are filled with semi-opaque staining and the pyroxene phenocrysts not surrounded by groundmass appear to have dissolved edges. Pyroxene can still be identified by their shape, cleavage and extinction angle. No olivine or common olivine weathering products are present in any of the slides analysed.

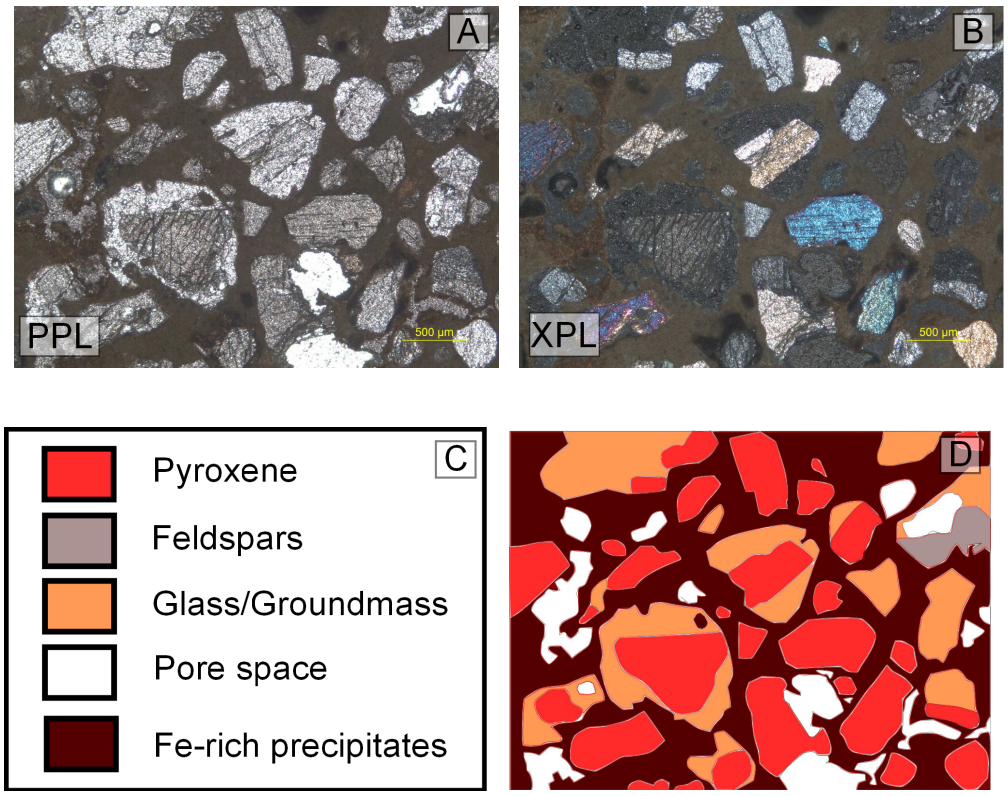

Figure 4.11 – Infilled, cemented section of subsurface Fe-rich layer, (A) plane-polarised light, (B) cross-polarised light, (C) legend, (D) key.

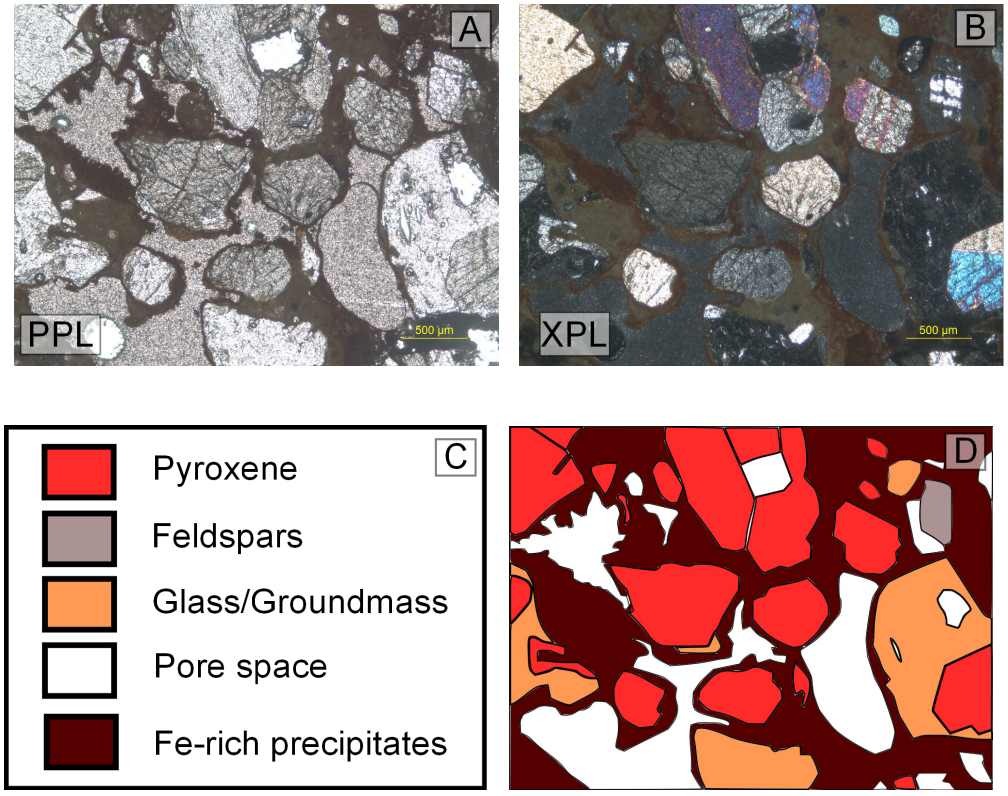

Figure 4.12 – Open pore, cemented section of subsurface Fe-rich layer, (A) plane-polarised light, (B) cross-polarised light, (C) legend, (D) key.

4.2.3 XRD

X-ray diffraction (Table 4.2) identified jarosite and goethite in the Fe-rich subsurface precipitate layer and Fe-precipitate layer from hot outflow. Many of the other minerals detected in the samples line up with the common minerals that make up the lavas found at White Island (i.e., feldspar and pyroxenes (Cole et al., 2000)). The Fe-rich subsurface precipitate layer and Fe-precipitate from hot outflow samples also have cristobalite, which is a common high temperature, low pressure, silica polymorph created during volcanic eruptions (Reich et al., 2009) and/or through acid S hydrothermal alteration of volcanic rocks (Gray and Coolbaugh, 1994; Hamasaki, 2002). Cristobalite which has been created through hydrothermal alteration has been observed at White Island (Wood, 1994; Giggenbach et al., 2003). However, the process that have lead to the formation of cristobalite in the samples tested by XRD cannot be discerned without additional testing.

Table 4.2 – Minerals found by XRD analysis

Sample ID	Description	Albite	Cristobalite	Jarosite	Goethite	Enstatite	Natroalunite	Magnetite
NW 2b	Fe layer coating creeks	✓				✓		
NW 5b	Fe-rich subsurface layer	✓	✓	✓	✓			
NW 12	Fe-precipitate from hot outflow	✓	✓	✓	✓			

When the XRD samples are analysed with respect to depth across a subsurface Fe-rich layer (Table 4.3), the subsurface Fe-rich layer (highlighted in pink) has albite, cristobalite, jarosite, goethite and enstatite. Jarosite and goethite were not found in the samples above or below the subsurface Fe-rich layer. The only other Fe mineral found in the samples was magnetite present in the top surface crater fill layer. The layers below the subsurface Fe-rich layer have natroalunite $NaAl_3(SO_4)_2(OH)_6$ which is a common product of hydrothermal alteration of volcanic rock. Natroalunite is in the same alunite mineral supergroup as natrojarosite which has the chemical formula $NaFe_3(SO_4)_2(OH)_6$.

Table 4.3 – Minerals found by XRD analysis by depth across subsurface Fe-rich layer

position	Sample ID	Description	Albite	Cristobalite	Jarosite	Goethite	Enstatite	Natroalunite	Magnetite
above Fe layer	2/1	Crater fill	✓				✓		✓
above Fe layer	2/3	Ash layer	✓				✓		
Fe layer	NW 13a	Fe-rich subsurface layer	✓	✓	✓	✓	✓		
below Fe layer	1/4	White precipitate layer	✓				✓	✓	
below Fe layer	1/5a	Crater fill with white precipitate removed	✓						
below Fe layer	1/5b	White precipitates and fine particles washed from 1/5a	✓	✓				✓	

4.2.4 XRF

XRF results for subsurface Fe-rich precipitate layers are shown in Figure 4.13. The results show fairly similar elemental compositions with minimal variation. Most of the variation is associated with Fe and S. The total Fe ranges from 14.33 to 21.60 wt% and total sulphur from 2.77 to 12.91 wt%. A table showing the full XRF results can be found in Appendix F.

XRF versus depth from sites 5 (subsurface Fe-rich layer and below) and 21 (above Fe-rich subsurface layer) are shown in Figure 4.14. The samples are ordered by depth/position relative to subsurface Fe-rich layer. These results show that the subsurface Fe-rich layer and the layers above have higher total Fe percentages than the layers below the subsurface Fe-rich layer. Total S percentages are variable between each layer tested and the layer with the highest S percentage was below the subsurface Fe-rich layer.

A sample of the layer saturated with water and white precipitate from below the subsurface Fe-rich layer at site 5 was split into two samples: 1/5a (the rock and sediment) and 1/5b (white precipitate and water soluble components). This was done to help understand how much Fe and S is potentially related to each. The results in Figure 4.15 show that most of the Fe is in the rock/sediments. Total S and Al are higher in the white precipitates, then in the rock in the sample. This higher Al content in the supports the XRD finding of natroalunite $NaAl_3(SO_4)_2(OH)_6$ which is an Al-rich mineral (Table 4.3 sample 1/5b).

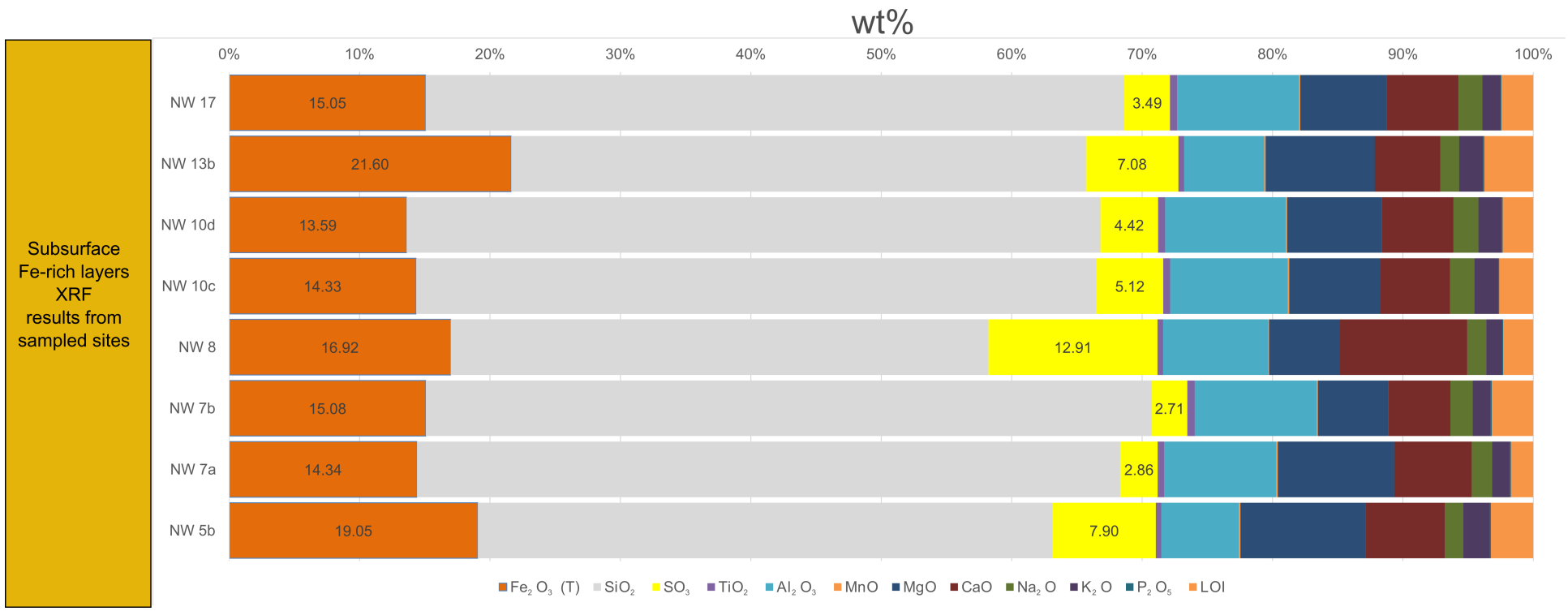

Figure 4.13 – XRF results for all subsurface Fe-rich precipitate samples

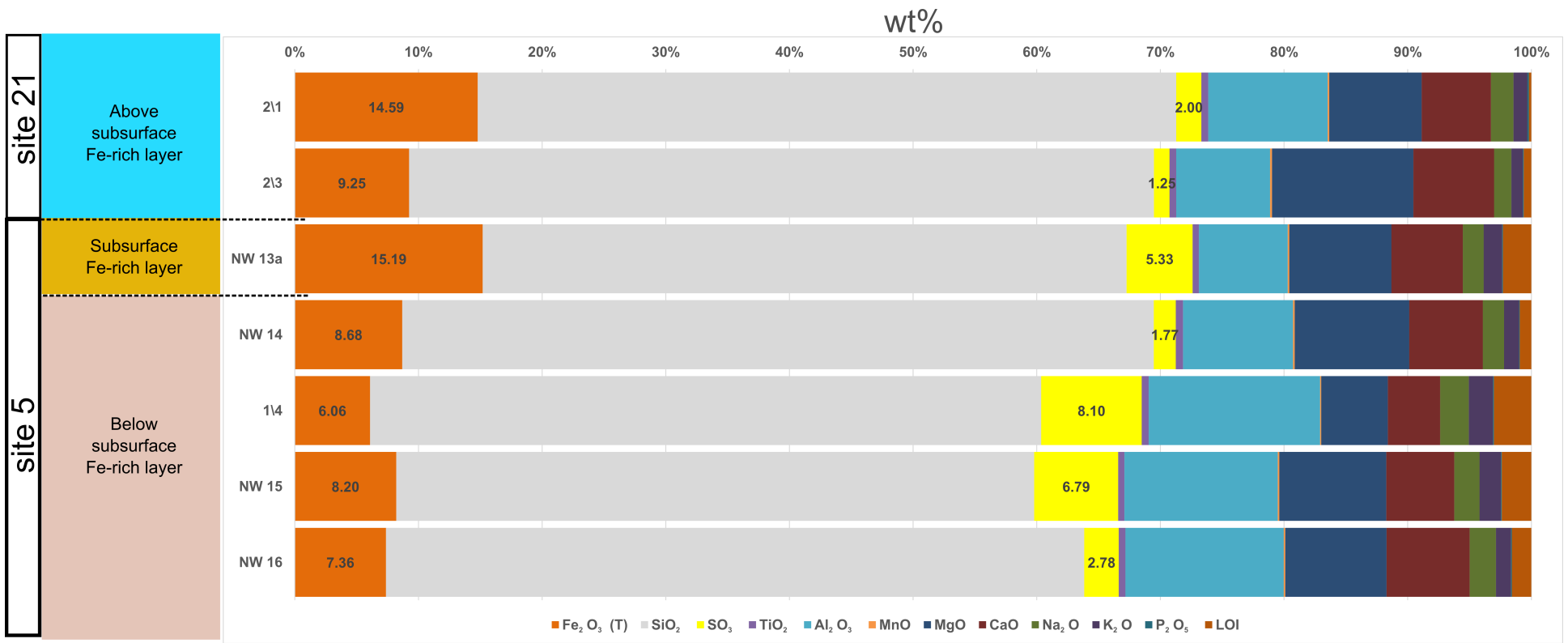

Figure 4.14 – XRF data vs depth across a Fe-rich precipitate layer

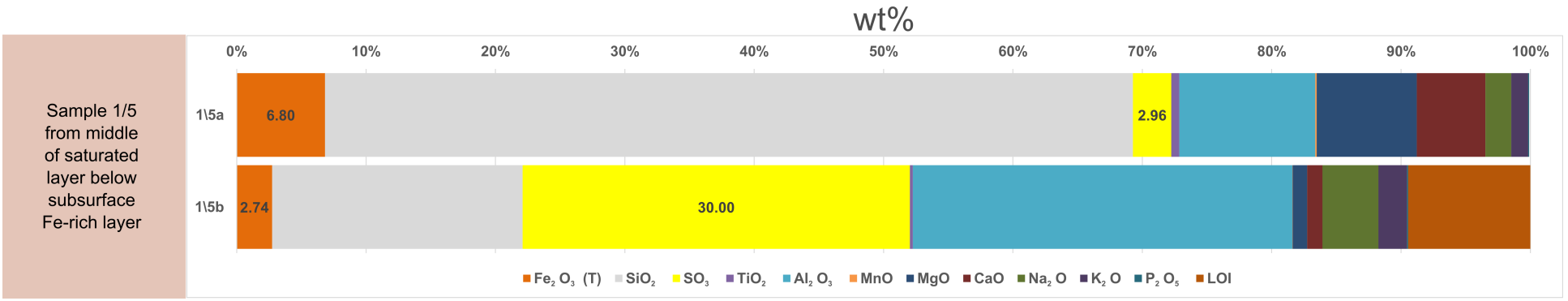

Figure 4.15 – XRF data for sample 1/5 (sample from approx middle of white precipitate saturated layer below Fe-rich subsurface layer), Sample 1/5 was split into two samples 1/5a (rock and sediments) and 1/5b (precipitates and water soluble minerals washed from 1/5a).

4.2.5 Raman spectroscopy

Raman analyses identified that the Fe-rich subsurface layers are dominantly jarosite based on the spectra from a variety of sample sites. Raman spectra in Figure 4.16 show the closest spectra matches are either jarosite and/or natrojarosite. This confirms XRD data showing jarosite in the layers. Other Fe-rich minerals are potentially in the thin section but because of the point source used for raman analyses we did not get a strong signal from those minerals. The spectra for jarosite and goethite have very similar peaks, the strong jarosite signal maybe overwriting the goethite spectra sites. In polished thin section the Fe-rich areas targeted looked amorphous, no individual internal layers or crystals could be identified, which may mean the Fe-minerals are mixed. There are some minor unknown peaks within the jarosite spectra which may be from goethite or another unknown mineral, a definitive identification of the minerals related to the minor peaks was not able to be made. Raman analyses did not provide an adequate means to identify other Fe-minerals in these fine grained precipitate layers.

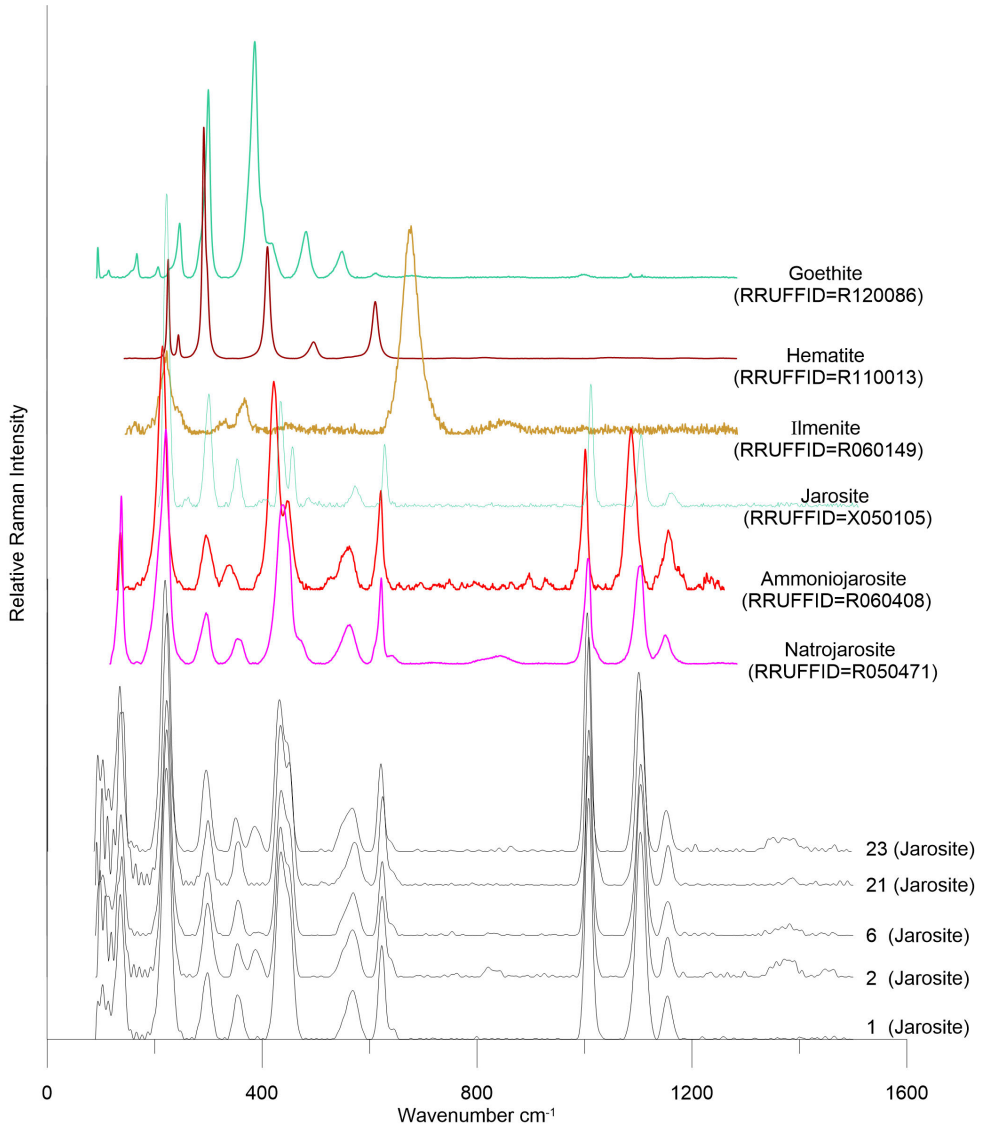

Figure 4.16 – Raman spectra from tested sites 1,2,6,21,23 on polished slide (jarosite) compared to Fe-rich minerals reference spectra

4.2.6 SEM with EDS

Polished slides created from Fe-rich subsurface layer at site 5 (sample NW 5b) were analysed using EDS. Volcanic glass/groundmass, phenocrysts and Fe-rich precipitates were spot analysed and element maps were created. Point sampling results are shown in Figure 4.17. Feldspar, volcanic glass/groundmass and pyroxenes have little to no content of S by wt% and the amount of Fe in the groundmass and phenocrysts are similar to values given in Cole et al. (2000). Any site the phenocrysts and volcanic glass have been altered show either an enhanced total percentages S and/or Fe and in some cases increases in both. The forming Fe precipitate(s) have a high percentages of Fe, >36.9% and S >13.7% at all sites measured. A table with full elemental percentage results can be found in Appendix G.

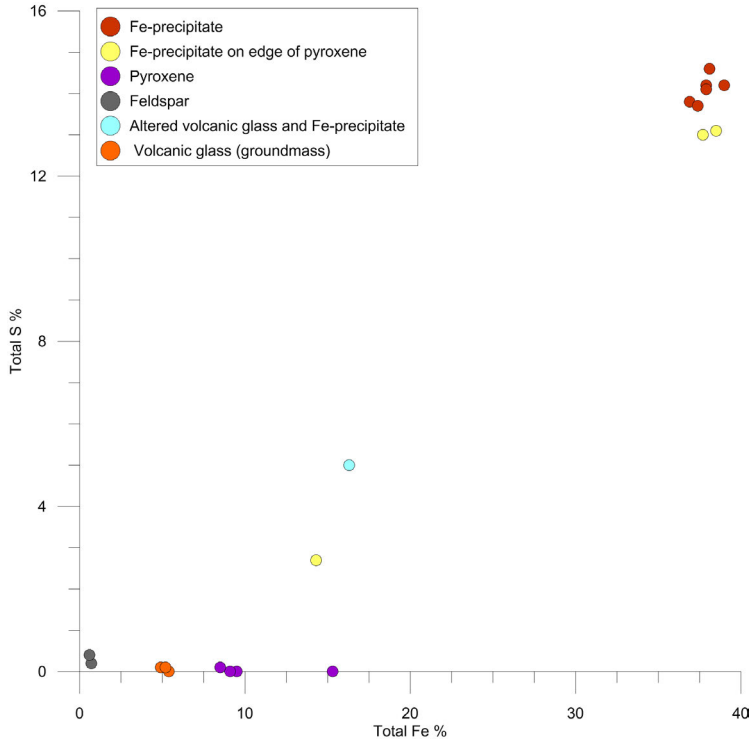

Figure 4.17 – EDS Total S/Fe for minerals found in subsurface Fe-rich layer

The EDS element map in Figure 4.18 is of an area similar to open pore section where the Fe-precipitate is coating, infilling and cementing clasts/phenocrysts (see Figure 4.8D). Elemental gradients for each map is on the left hand side (white = 100% of element). The Fe-rich precipitates in the section show the highest percentages of Fe (Figure 4.18B) and S (Figure 4.18D). The groundmass and other phenocrysts have the highest Mg (Figure 4.18C) and Si (Figure 4.18E) elemental concentrations. Any site that has high Si or Mg has low concentrations of Fe and S and vice versa.

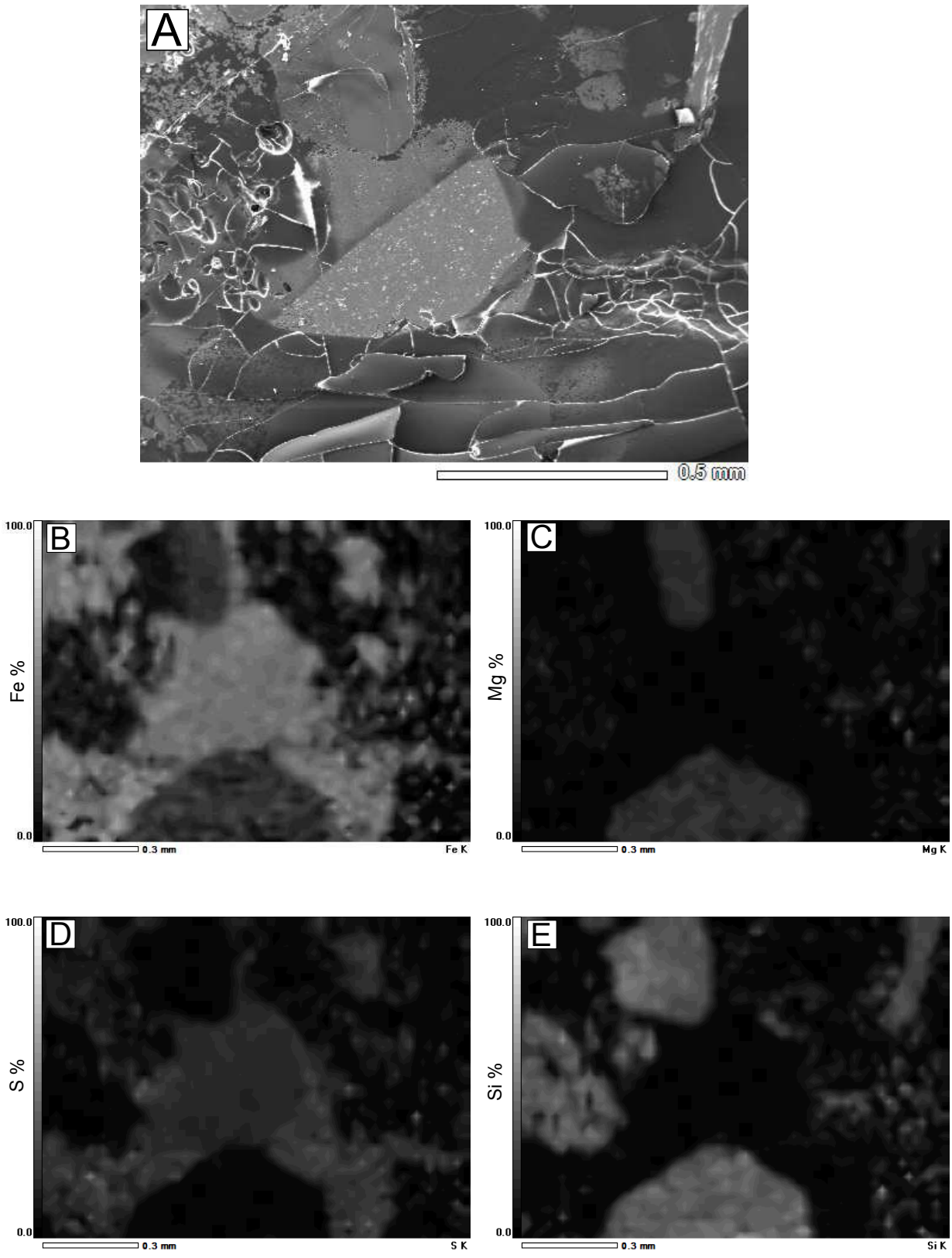

Figure 4.18 – EDS map of Fe-rich precipitate site 1

4.2.7 Water chemistry

On the day of water sampling, the air temperature was 12℃ and there had been no precipitation on White Island for at least two days. Water samples 1 to 22 are from the main acid stream and many side streams running over the Central and Eastern Subcrater zones. The Eh/pH and temperature results are summarised in Table 4.4 and the elemental analyses are in Table 4.5. Full results can be found in Appendix H for Eh, pH and temperature and in Appendix I for full ICP-OES results including major elements and rare earth elements (REEs). Creek temperatures ranged from 16.4 to 70 ℃, the pHs from 0.730 to 3.084, and Eh from 122 to 204.2 mv. When the samples are compared to meteoric water (Table 4.4), the pH of the creek water is very low (acidic) and the seawater is similar (near neutral). All the Eh values measured from the creek and seawater are close to, or less than half the lowest Eh value given for meteoric water (Table 4.4). Creek waters have overall low pH and Eh values when compared to meteoric water and the creek waters are comparatively more reducing than meteoric waters.

Table 4.4 – Summary field measurements of Eh, pH and Temperature

	Temperature	pH	Eh in mv
sample number 1 to 22 Average Totals	31.6	1.4	168.8
sample number 23 (Sea water)Total	16.2	6.4	128.2
Meteoric water (from Sanders (1998))	ambient	4 to 7	400 to 600mv

ICP-OES results of water samples show high amounts of dissolved metals. Iron concentrations range from 28.1 to 1268.0 mg/L and S values are between 262.1 to 1449.2 mg/L. Averages of major elements from creek and seawater are listed in Table 4.5. When compared to the creek waters, the seawater (sample number 23) has a high of pH 6.4 and low Fe concentration of 1.88 mg/L and an near average S concentration of 882.89 mg/L. Sample 2 (see site Appendix I) which was a hot outflow actively depositing Fe-precipitates had the lowest Fe reading 28.1 mg/L. Other element concentrations are variable and full elemental analysis are in Appendix I. It was noted during field work that the creeks are fed from multiple sources, which are outflowing from depth (the creeks are fed by hydrothermal sources). Creek data potentially give a insight into the geochemical environment at depth. Water analysis results (Table 4.5) support that there are high amounts of dissolved metals within solutions and this data is used for geochemical modelling.

Table 4.5 – Summary table of ICP-OES analysis results showing major elements (units in mg/L), excluding REEs, (bd = below detection limit)

Elements	Average of samples 1 to 22 White Island Creeks	Sample 23 (sea water)
Al	512.92	1.81
Fe	390.74	1.88
Mn	19.26	0.21
Ca	1011.42	361.74
K	134.83	257.47
Mg	606.86	1216.97
Na	619.89	9928.52
P	1.81	0.04
S	900.11	882.89
As	0.17	0.04
B	5.40	4.98
Cd	0.005	bd
Cr	1.43	0.02
Cu	0.06	bd
Li	1.02	0.26
Mo	bd	bd
Ni	0.15	bd
Pb	0.11	0.03
Sr	2.23	7.86
Zn	0.84	bd

4.3 Biogeochemistry

4.3.1 Scanning electron microscope, Fe-rich layers and microbial life

Samples of Fe-rich layers from the surface and subsurface or the Main Crater were accessed for the presence of microbial life and/or biological byproducts using SEM. It was noted during field work that microbial streamers and algae are present in the creeks across the Central and Eastern Subcrater zones and often in great abundance. Many of the sites with microbial streamers also host Fe-rich layers that coat the bed of the creeks. The SEM analysis located microbes in multiple surface and subsurface samples taken from White Island. Table 4.6 provides an overview of Fe species present and whether microbes are present in the sample. Representative images of each sample can be found in Appendixes J and K.

Table 4.6 – Summary SEM results of Fe-rich minerals and microbial life in/on each sample.

Sample ID	microbes	diatoms	jarosite	goethite	schwertmannite	hematite	magnetite
NW1a			✓				
NW1b	✓						
NW2a	✓	✓					
NW2b	✓		✓		✓		
NW3							
NW4							
NW5			✓	✓			
NW6	✓						
NW7	✓	✓	✓	✓			
NW8				✓			
NW9							
NW10a			✓	✓			
NW10b	✓		✓	✓			
NW11a	✓	✓	✓	✓	✓		
NW11b	✓	✓	✓	✓	✓		
NW12	✓			✓			

(one tick designates that the microbes, diatoms or Fe-species were observed)

The thin Fe-rich layers that coat the base of low flow creeks (NW 2b, Figure 4.19A) shows the highest visible amount of microbial life at White Island. The needle-like (spiky) mineral that the microbes are attached and/or embedded in, matches descriptions of schwertmannite's unique pin-cushion morphology (Bigham and Nordstrom, 2000; Burgos et al., 2012). As schwertmannite is variable in its crystal morphology, visual identification is not reliable (Bigham and Nordstrom, 2000). However, the water chemistry from the sites and ochre red colour of the thin layers coating the creeks suggests these layers are potentially schwertmannite. The hot outflow Fe layer (NW 15, Figure 4.19B) has mainly rod shaped bacteria that are attached with extracellular polymeric substance (EPS), and some unusual collapsed looking structures spread across other sections of the Fe layer. This sample was taken from water with a temperature of 65℃ and pH of 3.084. A thick goethite layer has formed covering the base of the outflow (see Figure 4.3C).

Samples from the subsurface Fe-rich layers show microbes on the surface of the minerals. Overall, limited visual evidence of microbial life is present in the subsurface Fe-rich layer samples. Microbes observed within the subsurface Fe-rich layers are mainly rod shaped, individual or in small groups, randomly scattered. Figure 4.19C shows a rod-shaped microbe residing on possible schwertmannite in the Fe-rich subsurface layer (NW 11). Other rod-shaped microbes are scattered randomly throughout the sample. In some of the samples there is a large number of preserved diatoms. Figure 4.19D shows an intact diatom found in the Fe-rich subsurface layer (NW 7). The diatom is resting on goethite and in some areas layered groups of diatoms are cemented by minerals. Figure 4.19E shows a diatom and microbe sitting on goethite and Figure 4.19F shows a microbial fibre resting on jarosite crystals. These observations of microbes, identified through SEM imaging cannot confirm whether they are growing/living in the subsurface Fe-rich layers.

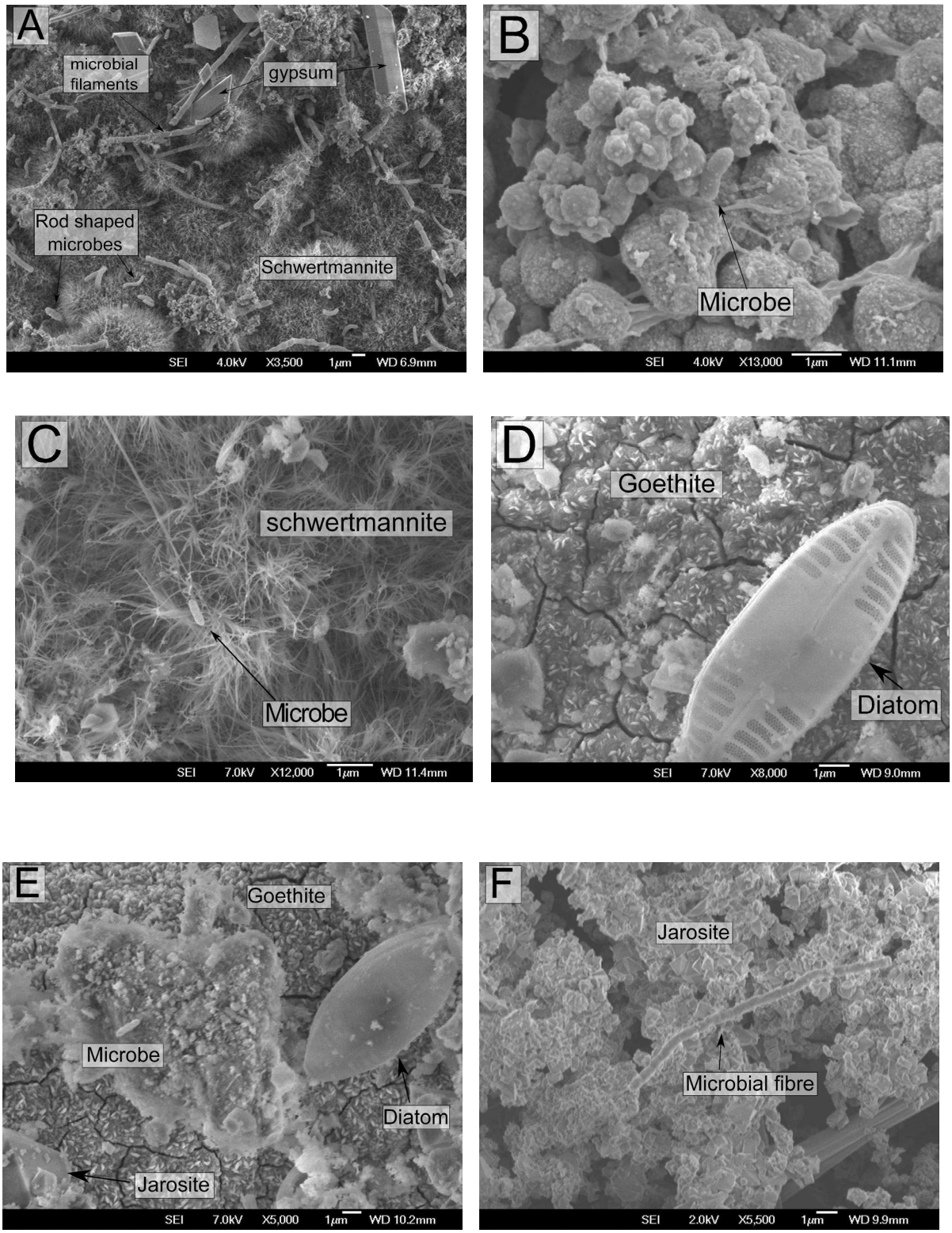

Figure 4.19 – Examples of microorganisms found on Fe-rich subsurface layers. (A) Thin Fe layer coating base of creek, (sample NW 2b), microbes, schwertmannite and gypsum crystals. (B) Goethite coating base of hotout flow (Sample NW 15), microbe and EPS sticking to forming minerals. (C) Rod shaped microbe sitting on schwertmannite, sample NW 11, soft Fe-rich subsurface layer. (D) One of the many intact diatoms sitting on goethite (sample NW 7), hard Fe-rich subsurface layer. (E) Diatom and microbe on goethite NW 7 (Fe-rich subsurface layer). (F) Microbial fibre and Fe-precipitate sample NW 10b (Fe-rich subsurface layer).

Figure 4.20 shows a cemented layer of Fe-rich minerals next to an area which starting to grow/nucleate Fe-rich precipitates on the mineral surface. In Figure 4.20A goethite has cemented jarosite minerals into a cohesive layer over the surface of the volcanic clast. This is a common mineral assemblage observed in the Fe-rich subsurface layers, (i.e., goethite mineralisation cementing and encasing jarosite). In Figure 4.20B Fe precipitates are shown to start nucleating on the clean glassy clast surface. When the site is examined in more detail, some of the forming goethite minerals have a unique rod shape, that look similar in size and shape to the potentially identified microbes at other sites in the subsurface Fe-rich layers. To correctly identify mineralised microbes using SEM, visual recognition depends upon them being distinct entities segregated from the host matrix (Jones and Renaut, 2007). At sites where Fe-rich minerals are forming, any microbes present, especially Fe oxidising microbes commonly covered in precipitates, will become enclosed in the growing Fe minerals. Microbial shaped minerals/features are common across the subsurface Fe-rich layers. These features are most likely related to goethite mineralisation. These microbial "looking" minerals need to be confirmed as mineral or biological using a different method.

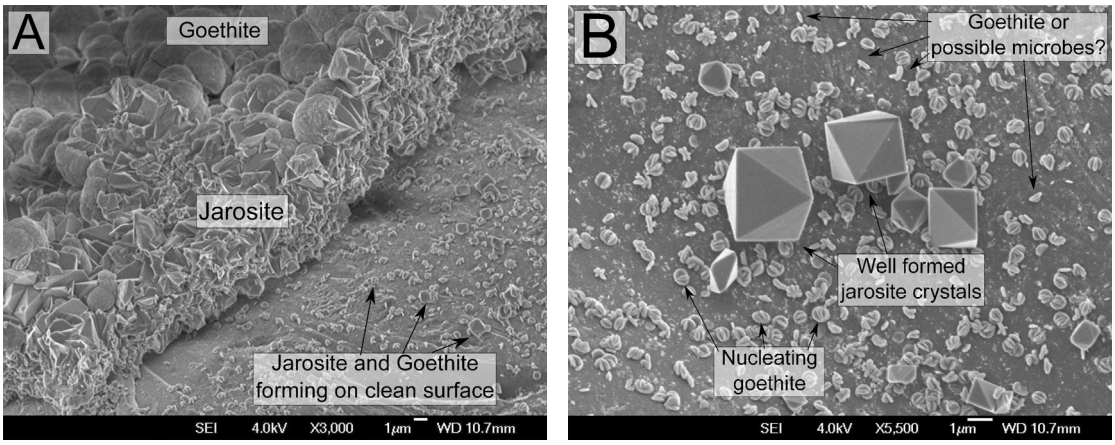

Figure 4.20 – Precipitating Fe minerals: (A) Precipitate on volcanic clast, (sample NW 5), on the left side of the image, thick precipitate layer of goethite surrounding and coating jarosite and on the right side Fe precipitates forming on clean clast surface. (B) Microbes or microbial shaped precipitates?, (sample NW 5), close up of nucleating Fe-precipitates, goethite and well formed jarosite crystals.

4.3.2 Carbon analyses

Carbon analyses of rock, sediments and subsurface Fe-rich layers are reported in terms of total C wt% and δ^{13}C (is reported in parts per thousand ‰). This information is used to determine how abundant inorganic/organic carbon is in the rocks, sediments and subsurface Fe-rich layers at White Island. Isotopic δ^{13}C values are also used to investigate the source of the carbon as well as for potential biosignatures. The results are presented in Figure 4.21 and Figure 4.22, the data is shown next to the crater sediment profile at each site. The residual carbon figures have been removed from C by wt% graphs since an unknown process has increased the total wt% of the carbon in the samples.

Carbon site 1 ((sample site 5) see Figure 4.1) is a well indurated (hard) layer, the total carbon by mass in the samples ranges between 0.04 and 0.12 wt% (see Figure 4.21A), with the highest amount of total carbon at the base of the Fe-rich layer (1/3 - 10cm). Organic carbon ranged any where from ≈10 to 80% of the total carbon. All samples have some organic carbon and the highest amount of organic carbon is below the Fe-rich layer (1/4 - 15cm). The δ^{13}C isotopic values for all samples are all below -23‰ (see Figure 4.21B). Carbon site 2 a poorly indurated (soft) Fe-rich layer ((sample site 21) see Figure 4.1) and it has a similar carbon chemistry to site 1. The total carbon by mass in the samples was found to range between 0.05 and 0.12 wt% (see Figure 4.22A), with the highest total carbon is in the Fe-rich layer (1/4 - 30cm). The organic carbon ranged between ≈10 to 60% of the total carbon and the δ^{13}C values for all samples are all below -23‰ (see Figure 4.22B).

Both sites show minimal amounts of carbon total carbon and smaller amounts of organic carbon in all the samples. The carbon isotope values of the organic carbon when compared to the total carbon values are within $\pm$1 of the total carbon isotopic values. Both present similar isotopis values. Whereas, many of the residual carbon samples present a lower sub -28‰ isotopic signature. The sub -23‰ (stable carbon) isotopic values at White Island are typical of organic carbon derived from life (Greenwood et al., 2013).

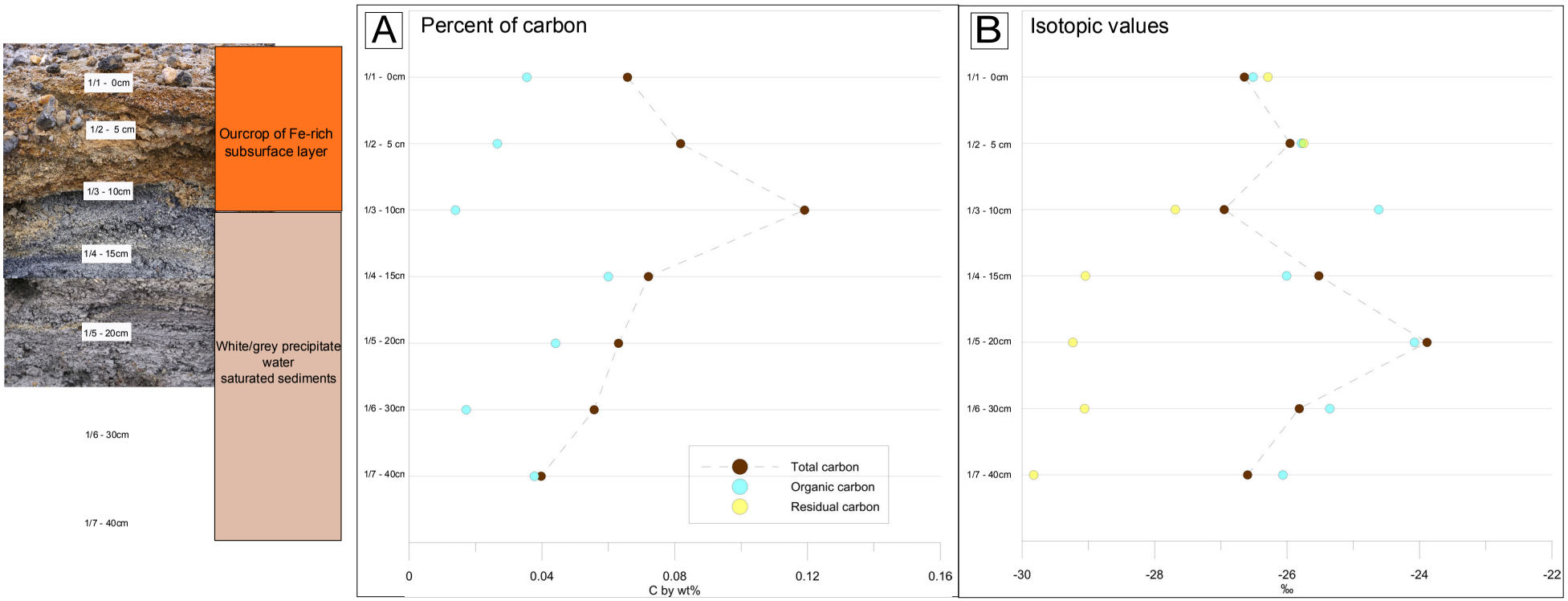

Figure 4.21 – Carbon site 1, (A) C by wt% for total and organic samples and (B) δ^{13}C isotopic values for all sample types down a vertical profile across subsurface Fe-rich layer.

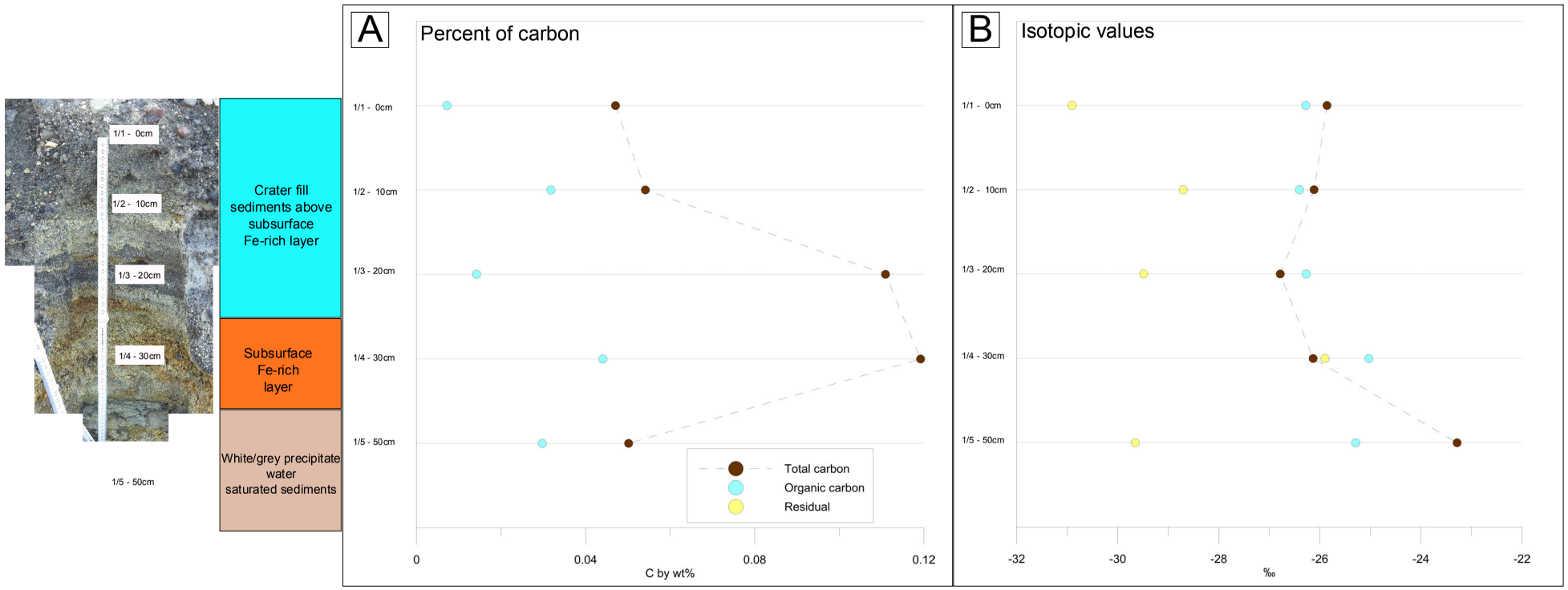

Figure 4.22 – Carbon site 2, (A) C by wt% for total and organic samples and (B) δ^{13}C isotopic values for all sample types down a vertical profile across subsurface Fe-rich layer.

4.4 Geochemical modelling

Data from the GGW database, ICP-OES water sampling and field measurements of Eh/pH are used for geochemical modelling. It was noted during analyses that element concentrations at many of the sites in the GGW database varied dramatically overtime. At site 1611 (GGW database) between 22/10/2008 and 12/11/2008, sulphate increased from 7520 to 14469 mg/L, (increased by 192.4%). Over the same period Fe concentrations dropped from 1489 to 1321 mg/L (decreased by 11.3%). Here, the average results from the GGW database (as an average high concentration for fluids:Table 4.7) and water sampling (as an average low concentration for fluids:Table 4.8) is utilised to evaluate Fe mineral formation/stability.

The lowest temperature measured at the base of the subsurface Fe-rich layer is 22.4 ℃. For all calculations the temperature range investigated is between 20 and 99 ℃. Two different Eh values are used when needed for calculations: 1) the average Eh from the creek data 168 mv (used as low value) and 2) an Eh of 600 mv (used as high value) which is the upper Eh value given for meteoric water (see Appendix H). Minerals considered during modelling of saturation index (SI) values are $Fe(OH)_3$(a), jarosite(ss), jarosite-K, jarosite-Na, schwertmannite, goethite, gypsum and sulphur. Calculations of SI were completed with respect to changing temperature and pH. Data set 1 (Table 4.7) and data set 2 (Table 4.8) are used in the modelling.

Table 4.7 – Data set 1 (SI high concentration) Fe, S, K, Na, Ca, temperature, pH averages from Appendix C.3

	Average Fe content mg/L	Average Sulphate mg/L (as SO4)	Average Potassium mg/L	Average Sodium mg/L	Average Calcium mg/L	Temperature ℃	Average pH
Creeks and Streams	1529.85	6491.42	925.15	5601.67	1928.49	22.4	1.19

Table 4.8 – Data set 2 (SI low concentration) Fe, S, K, Na, Ca, temperature, pH averages from Appendix I

	Average Fe content mg/L	Average Sulphate mg/L (as SO4)	Average Potassium mg/L	Average Sodium mg/L	Average Calcium mg/L	Temperature ℃	Average pH
ICP-OES data creeks	390.74	900.11	134.83	619.89	1011.42	22.4	1.4

In Phreeplot, data sets 1 (Table 4.9) and 2 (Table 4.10) are utilised to calculate Pourbaix diagrams or Eh/pH diagrams. Element concentration and the effect of temperature Fe mineral stability fields are assessed by creating diagrams from temperatures 20 to 90 ℃ in 10℃ increments. Mineral phases are constrained to $Fe(OH)_3$(a), jarosite(ss), jarosite-K, jarosite-Na, schwertmannite, goethite and hematite. The gas pressures and ratios used

for O_2, CO_2 were set to atmospheric. Water stability lines are included on the graphs. The Phreeplot hunt and track method of diagram construction was used. The Eh and pH water results from Appendix H are added to the graphs as well as the highest Eh and mid range pH values given for meteoric water H.

Table 4.9 – Data set 1 (Eh/pH high concentration) Fe, S, K, Na, averages from Appendix C.3

	Average Fe content mg/L	Average Sulphate mg/L (as SO4)	Average Potassium mg/L	Average Sodium mg/L
Creeks and Streams	1529.85	6491.42	925.15	5601.67

Table 4.10 – Data set 2 (Eh/pH low concentration) Fe, S, K, Na, averages from Appendix I

	Average Fe content mg/L	Average Sulphate mg/L (as SO4)	Average Potassium mg/L	Average Sodium mg/L
ICP-OES data creeks	390.74	900.11	134.83	619.89

4.4.1 PHREEQC (Version 3)

Results for data set 1 (Table 4.7) will be presented since both data sets presented similar results with very little variation. Changing the concentration of elements between the high to low values had little effect on the SI results observed. The effect of pH on SI (Figure 4.23A and B) shows all minerals are undersaturated at low pHs. The jarosite family of minerals is undersaturated at all pHs (Figures Figure 4.23A and B), whereas, goethite and $Fe(OH)_3(a)$ become oversaturated as pH increases. Schwertmannite becomes oversaturated at pHs above 8 in (Figure Figure 4.23B). As the Eh is increased (Figure 4.23A) to (Figure 4.23B) a marked change happens to the SIs of all minerals where all species become less undersaturated. Increases in both Eh and pH can change the SI of Fe-minerals into oversaturation.

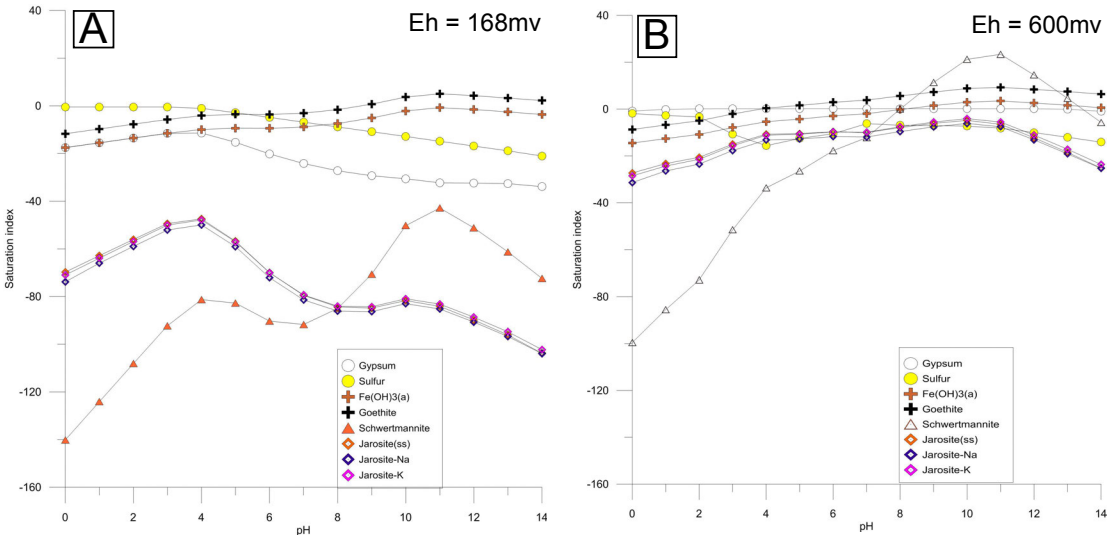

Figure 4.23 – Affect of pH on SI results solution data set 1

Temperature has a minimal effect upon SI values at the temperature range considered for all minerals, except schwertmannite (Figure 4.24) which becomes less undersaturated as temperature is increased. All Fe-minerals were undersaturated at all temperatures only S (in Figure 4.24A) and gypsum (in Figure 4.24B) were in oversaturation. Increasing pH can move some of the Fe species into oversaturation, whereas, temperature does not within the range tested. When Figure 4.23 and Figure 4.24 are compared against each other, it can be observed that increasing Eh makes the Fe minerals become less undersaturated. Overall, Eh and pH were more effective at changing SI values than temperature, with respect to the geochemical and temperature parameters used in modelling.

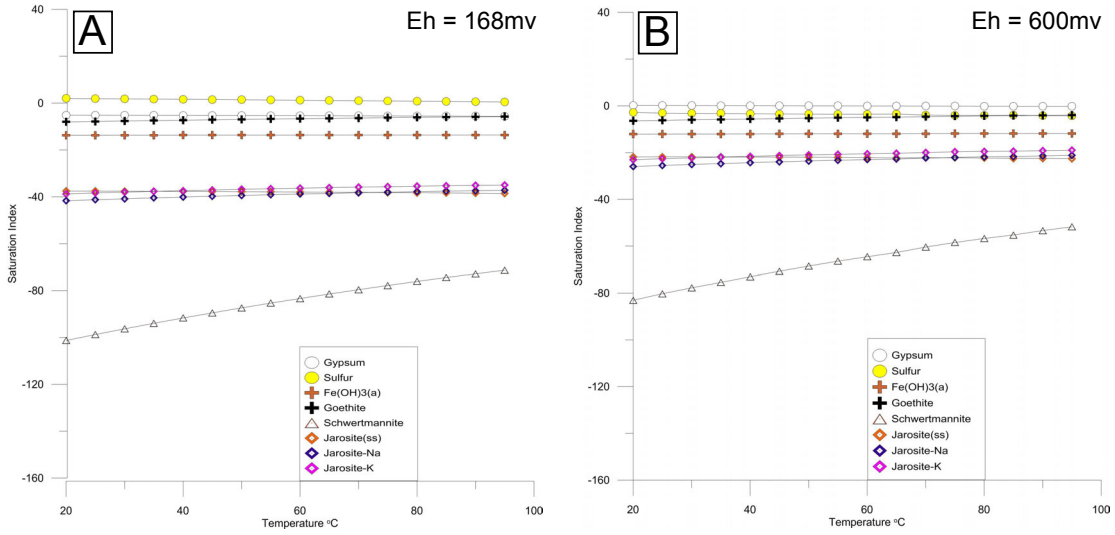

Figure 4.24 – Affect of temperature on SI results solution data set 1

4.4.2 Phreeplot

Figure 4.25 shows the results using data set 1 (Table 4.9) with jarosite(s), schwertmannite and $Fe(OH)_3$(a) (used as an analog for goethite). As temperature increases (see Figure 4.25), schwertmannite becomes more dominant and its stability field increases at the expensive of $Fe(OH)_3$(a) and jarosite. The main species of jarosite changes from being dominantly jarosite(ss) to jarosite-K as temperature is increased. At 20℃ (Figure 4.25B) all the creek data (Eh pH data collected) plots within the Fe^{2+} stability field. The seawater and meteoric water plot within the schwertmannite stability field. This shows that the waters collected from the crater creeks at White Island are relatively reduced and acidic when compared to meteoric water and seawater.

Schwertmannite becoming a dominant mineral phase at higher temperatures agrees with the effect temperature has on SI (seen in Figure 4.24). Temperature appears to have a significant affect on the stability of schwertmannite in the hydrothermal fluids. Modelling completed using data set 2 (Table 4.10) gave almost identical results to (Figure 4.25), the only major changes observed were that the S-rich species are less dominant, jarosite fields is reduced in size and the $FeHSO_4^{2+}$, $FeSO_4^{+}$ fields is replaced by Fe^{3+} species (as seen in Figure 4.26B).

When data set 1 (Table 4.9) was modelled without schwertmannite, the $Fe(OH)_3$(a) (goethite) mineral species becomes dominant (see Figure 4.27). As temperature is increased the $Fe(OH)_3$(a) stability field reduces in size and the jarosite stability field increases. Creek data still plots with in the Fe^{2+} stability field at all temperatures. Meteoric water plots within the $Fe(OH)_3$(a) field at <30℃ and seawater at <60℃, above those temperatures the waters will plot within the jarosite field. With no schwertmannite forming, goethite has the largest stability field at temperatures <70℃ and jarosite has the largest at temperatures >70℃. When data set 2 (Table 4.10) was modelled without schwertmannite forming, the same pattern observed in Figure 4.26B was found, the jarosite fields were reduced in size and the $FeHSO_4^{2+}$, $FeSO_4^{+}$ fields are replaced by Fe^{3+} species. This slight reduction in size of the jarosite stability field was observed at all temperatures tested when results from data set 1 and 2 were compared. This shows changes in element concentrations can affect mineral stability and species.

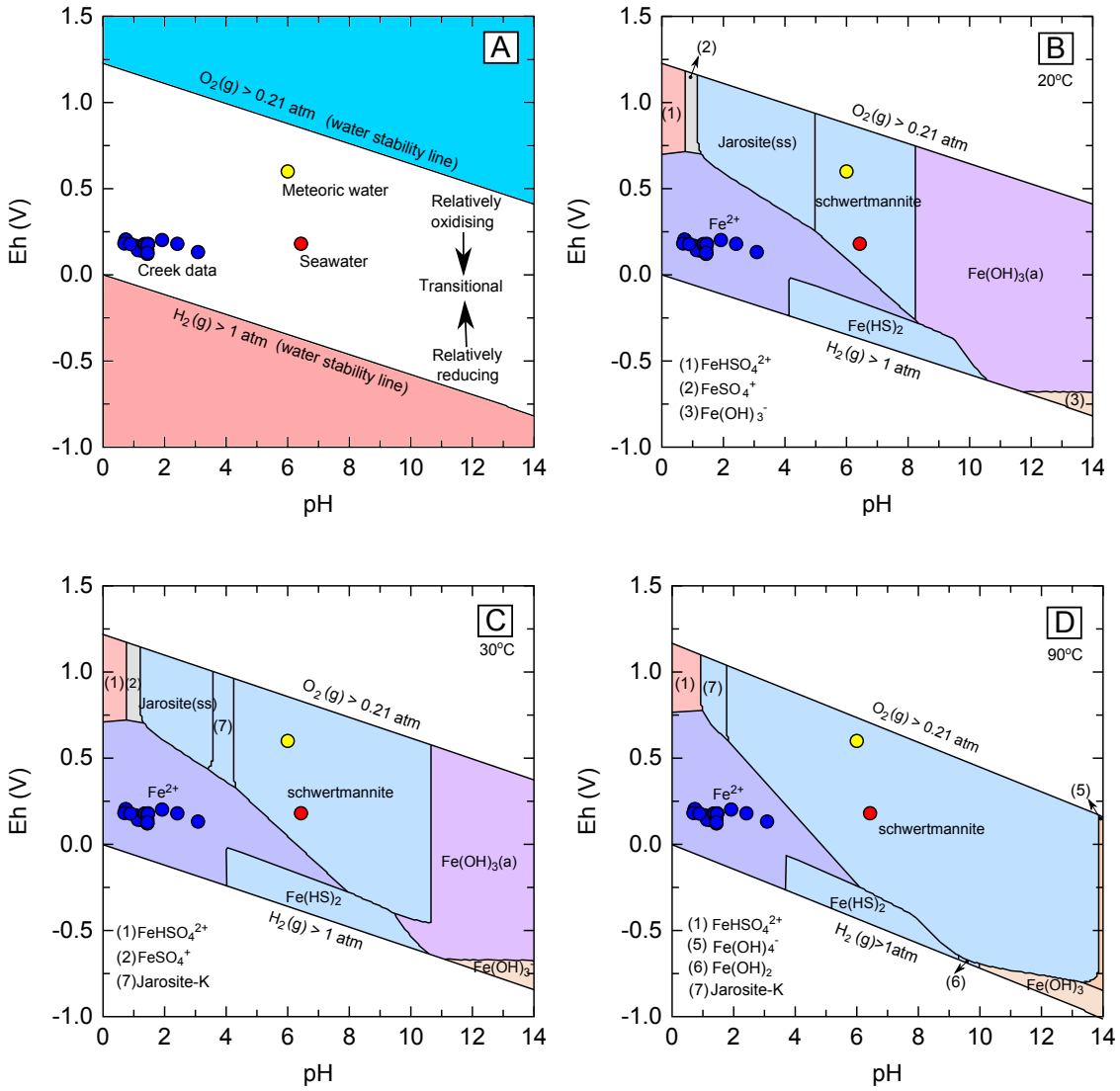

Figure 4.25 – Schwertmannite Eh pH results using (data set 1) Table 4.9

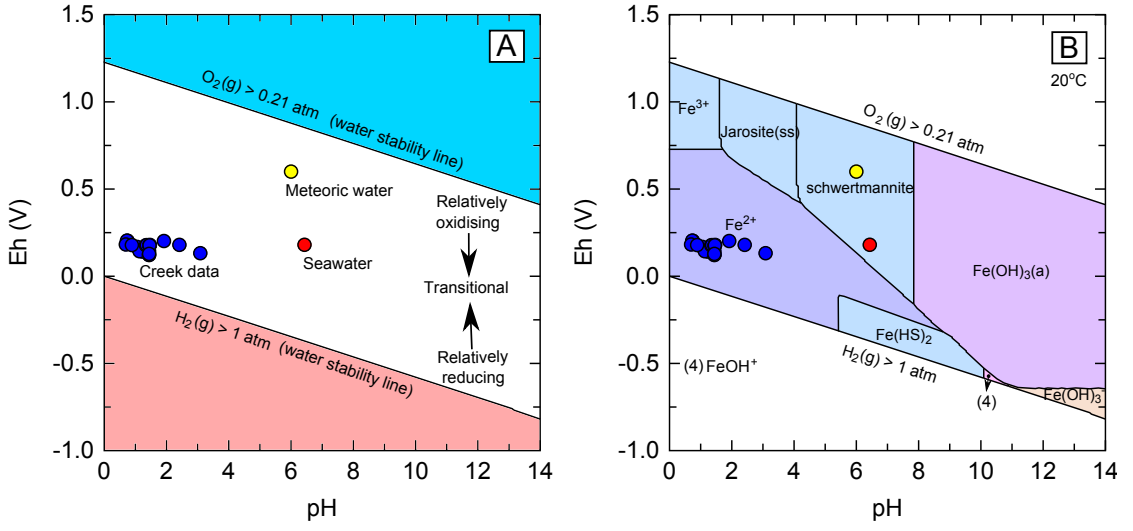

Figure 4.26 – Schwertmannite Eh pH results using (data set 2) Table 4.10

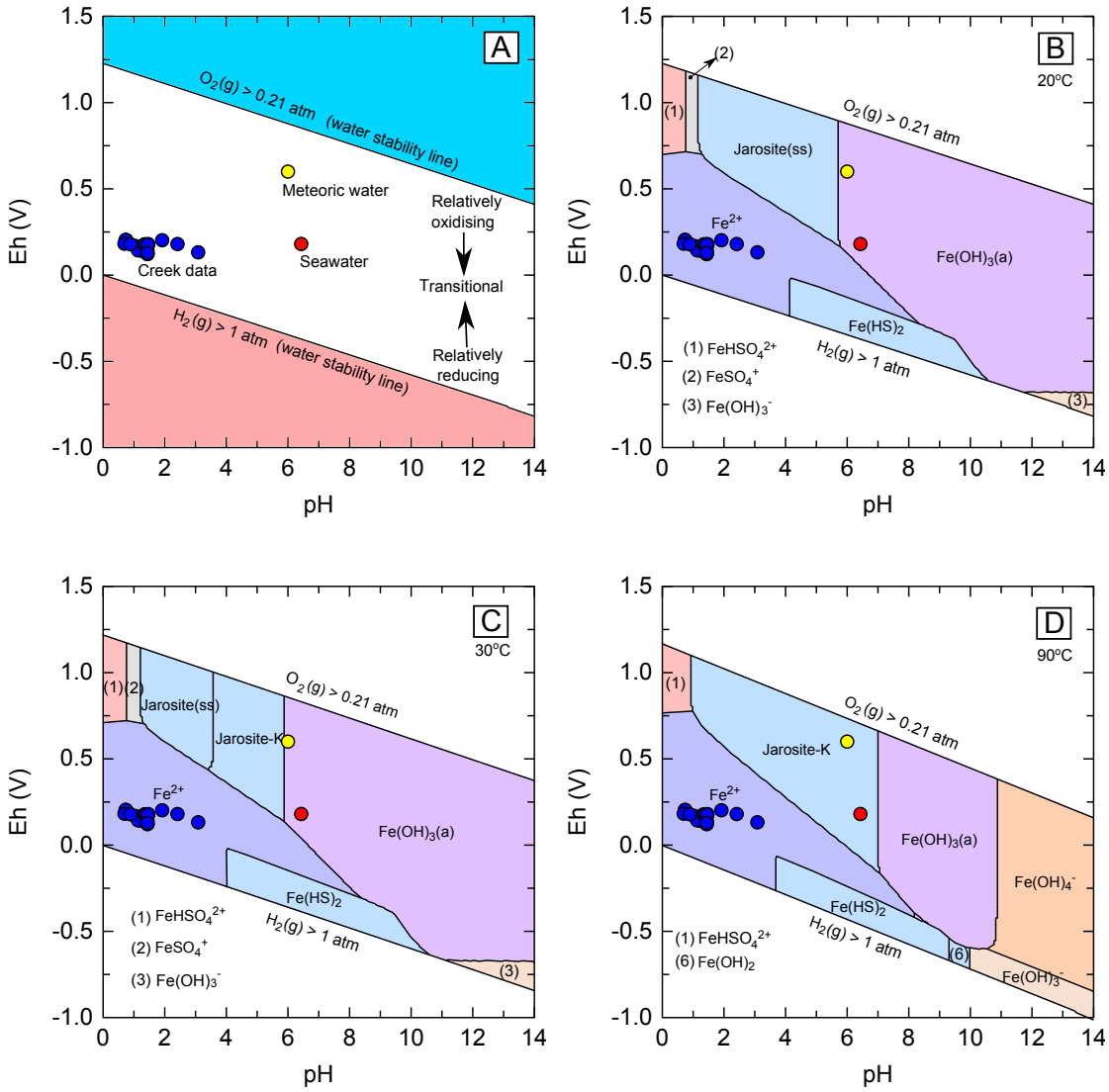

Figure 4.27 – Eh pH results with no schwertmannite precipitating for solution 1

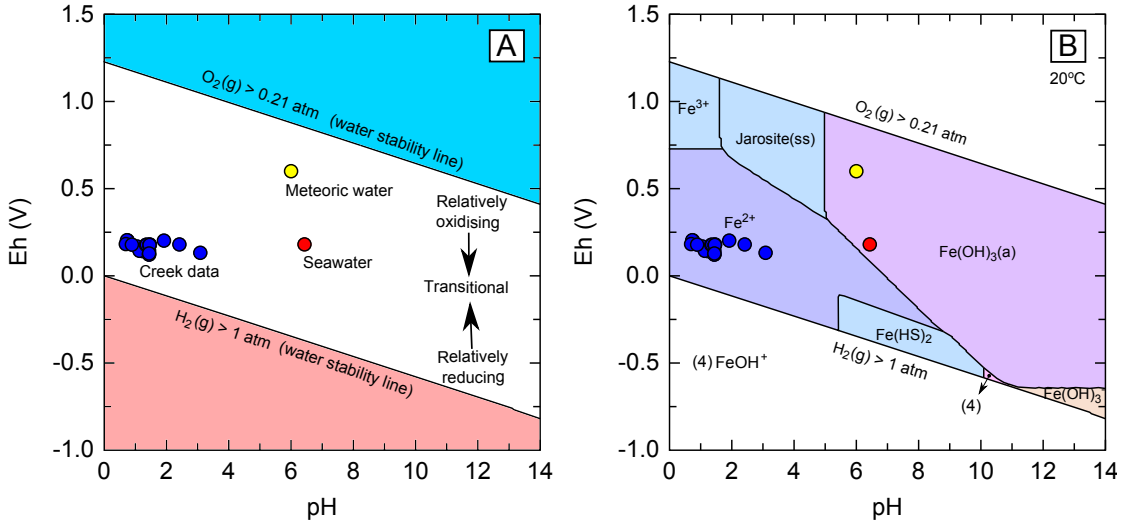

Figure 4.28 – Eh pH results with no schwertmannite precipitating for solution 2

Chapter 5: Discussion

5.1 The formation of subsurface Fe-rich precipitate layers

The subsurface environment at White Island can be visualised in terms of an series relatively static zones (i.e., alternating layers of oxidising/reducing zones). The surface environment at White Island provides an interfacial zone between atmospheric, meteoric (i.e., oxidising environments) and volcanic systems (i.e., reducing). Geochemical and potentially biogeochemical interactions can lead to the formation of secondary minerals and/or metal-rich deposits, potentially concentrating economic metal and affecting the dynamics of fluid/gas flux from the epithermal system. At White Island this geochemical interfacial zone results in an Fe-rich layer pervasively found at less than 1.5m depth within the Main Crater. The epithermal and hydrothermal systems at White Island are being structurally focused into a relatively confined area when compared to other epithermal systems (i.e., Yellowstone Park). Whether assessing White Island or other similar volcanic systems from around the world, interface geochemistry accentuates microscopic processes that could potentially affect the macroscopic character of a epithermal and potentially a volcanic system.

At the surface and in the subsurface at White Island hydrothermal fluids, gases and heat leaches/alters volcaniclastic sediments and volcanic rock creating clays and secondary minerals (Slansky, 1975; Hedenquist et al., 1993). During investigations of the field area at White Island, it was observed that many of the Fe-rich layers forming at the surface were found precipitating out of upwelling hydrothermal and/or creek waters. The subsurface Fe-rich layers are forming in crater fill sediments which are comprised of a mix of eruptive volcanic products and/or volcaniclastic sediments, including new/fresh lava, ash, tephra, bombs, old hydrothermaly altered/weathered pieces of crater wall.

The subsurface Fe-rich layers are composed of a mix of crater fill and Fe-rich minerals. The crater fill substrate is cemented by Fe-rich minerals creating cohesive layers (see Figure 5.1). The Fe-rich layers range from poorly indurated to well indurated, and from 4 to ≈50cm in thickness. Fe-rich minerals cementing the layers together are primary composed of jarosite and goethite. Jarosite species are most likely jarosite(K) $KFe_3(SO_4)_2(OH)_6$ or natrojarosite $NaFe_3(SO_4)_2(OH)_6$ jarosite types based on Raman spectroscopy (see Figure 4.16). As shown by SEM goethite forms on the surface of volcanic clasts, cementing the clasts and well formed crystals of jarosite into the subsurface Fe-rich layer (see Figure 4.20A). A mixture of jarosite and goethite was found to be the most common combination in the subsurface Fe-rich layers. An unknown needle like mineral was found to be

forming in the thin layers coating the creek(s) (see Figure 4.19A) and in some of the less indurated subsurface Fe-rich layers (see Figure 4.19C). The samples have a reddish ochre colour and the unique pin-cushion morphology seen in both the creek and less indurated subsurface Fe-rich layers matches descriptions of schwertmannite from Bigham and Nordstrom (2000). Schwertmannite is known to form in high S, Fe rich environments (Bigham et al., 1996b) and can be formed as a result of microbial activity (Kawano and Tomita, 2001; Burgos et al., 2012; Zhu et al., 2013). Schwertmannite is meta-stable and transforms into jarosite and goethite (Acero et al., 2006). Reanalysis of the possible schwertmannite six months later using SEM found that the needle like minerals had disappeared. This potentially shows the forming needle-like mineral is meta-stable like schwertmannite and most likely transforming into another Fe-rich mineral overtime. Schwertmannite was not able to be confirmed during geochemical analysis of the Fe-rich mineral samples.

Figure 5.1 – Subsurface Fe-rich layer eroded out of crater sediments by creek (geological hammer for scale).

To understand the origin of the subsurface Fe-rich precipitate layers the source of the main constituents making up the Fe-rich minerals has to be understood. Jarosite and goethite in the subsurface Fe-rich layers are made up of Fe, S and O which has been mobilised to the site where subsurface Fe-rich layers are forming and/or leached out of rock/minerals in place. Layers above the Fe-rich layers were found to be dry or slightly

damp with little to no visible Fe precipitate(s) forming in the layers. Conversely the layers below were found to be saturated with H_2O and white/grayish coloured precipitates, as well as having higher temperature than the overlying layers. The temperature at the base of the subsurface Fe-rich layer had a range of 22.0 to 35.0℃ and directly above the subsurface Fe-rich layers the temperatures had a range of 15 to 19℃. At site 5 (see Figure 4.1) the temperature changed from 35℃ at the base of the Fe-rich layer to 19℃ above, this reduction in temperature occurred over distance of 7cm (the thickness of the Fe-rich layer). XRD analysis (see Table 4.3) found the white precipitate to be natroalunite. Natroalunite is common product when volcanic rock is hydrothermally altered (Raymahashay, 1968; Slansky, 1975; Zimbelman et al., 2005; Ece et al., 2008) and it is a member of Alunite Supergroup closely related to natrojarosite. The volcanic glass and phenocrysts in the subsurface Fe-rich layers above the alunite rich zone below shows potential evidence of hydrothermal alteration in thin section. Even the pyroxenes which are more resistant than feldspar show dissolved edges (Figure 4.10) which could be the result of intense hydrothermal alteration.

Whole rock chemistry via XRF (see Figure 4.14) found that the percentage of Fe_2O_3 (T) wt% generally decreases with respect to depth. The subsurface Fe-rich layer and the layers above have 1.5 to 2 times the Fe_2O_3(T) wt% seen in the layers below subsurface Fe-rich layer. This suggests the main leaching zone being below the Fe-rich layer. The lavas and minerals erupted at White Island have a low S content <0.04 wt% (see Appendix B). EDS found that the Fe-rich minerals cementing the Fe-rich subsurface layer have S values of >13% (see Appendix G). Whole rock chemistry via XRF (see Figure 4.14) found that all the layers tested have an enhanced S concentration ranging from (1.25 to 8.10 wt%) which is over the 0.04 wt% commonly expected in erupted lavas. This enhanced amount of S is likely from hydrothermal gases (see Appendix D) and/or waters (see Appendix I) as both carry high amount of S. The movement of Fe and S is potentially related to the high flux of heat, gas and water originating from the hydrothermal system and migrating upwards through the crater sediments.

Figure 5.2 shows the chemical reactions that are involved in the formation of Fe precipitates recognised in the subsurface layers. The reactions start with the oxidation of Fe^{2+} to Fe^{3+} (reaction 5.2). The oxidised Fe is then involved in producing goethite (reaction 5.3), jarosite (reaction 5.4) and schwertmannite (reaction 5.5). Reaction 5.2 uses acidity and O_2, whereas, the Fe mineral forming reactions all generate acidity (H^+). Both jarosite, goethite and schwertmannite need an oxidising environment to form Fe^{3+}-rich precipitates unless other factors like microbial activity are involved directly in oxidising Fe^{2+} to Fe^{3+}.

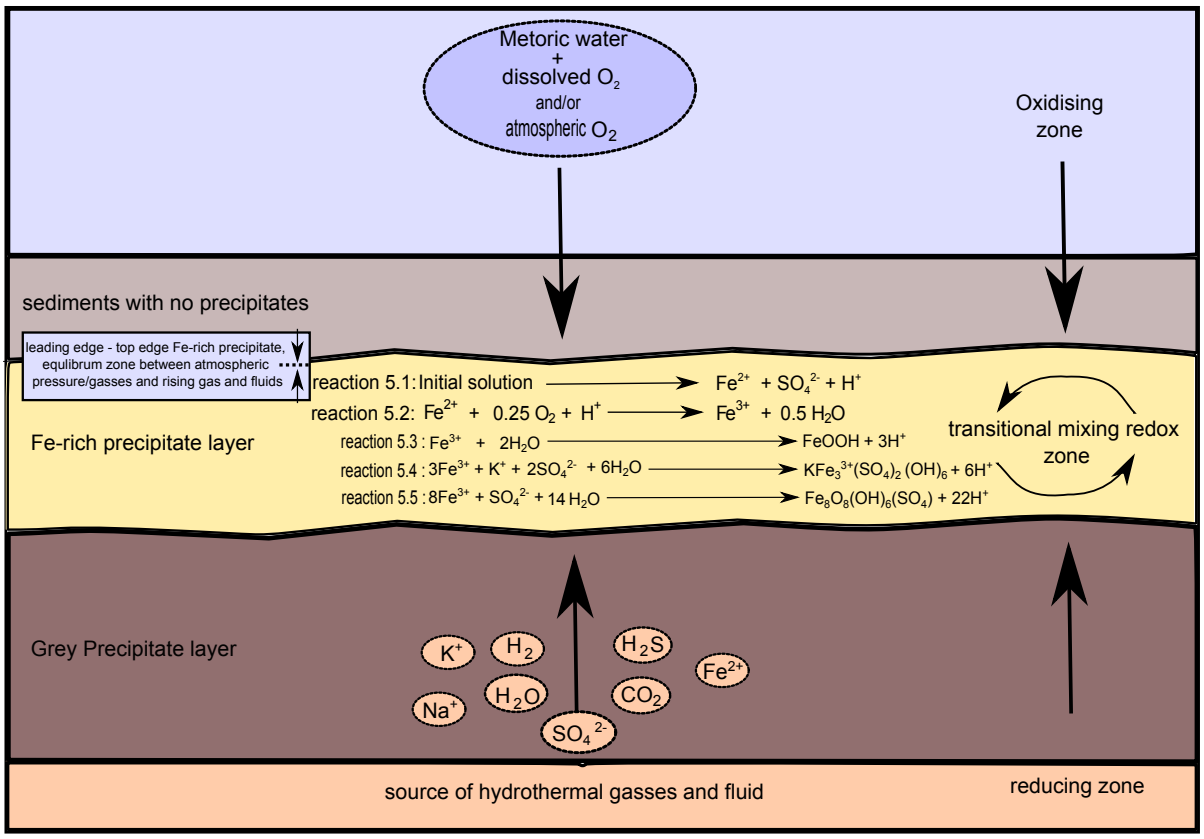

Figure 5.2 – Cross section showing deposition and creation of Fe precipitates in geothermal system, including chemical formulae from Figure 2.4.

Figure 5.3 shows the pH range jarosite, goethite, schwertmannite and ferrihydrite may form. The light grey area is the full range of pHs found in creeks (see Appendix C.3) and blue area is meteoric water (see Table 4.4). Jarosite is the only mineral that should be forming in the acidic creek water(s). The acidic creek fluids would need to be increased above a pH of >3 to precipitate schwertmannite and goethite which is possible with meteoric water. Both jarosite and goethite are forming in the subsurface Fe-rich layer(s) potentially at the same time, but they both form and are stable under divergent pH conditions. This may indicate fluctuating cycles between just hydrothermal water(s)/gases permeating the crater sediments creating an acidic environment (lowering pH) and hydrothermal water(s)/gases mixing with meteoric water neutralising acidity (raising pH). Fluctuating cycles between hydrothermal and meteoric water(s) could potentially lead to the mix of Fe minerals present in the subsurface layers.

The subsurface environment has two major sources of O_2: atmospheric gases and meteoric water (Zimbelman et al., 2005). This means the subsurface (at least at shallow depths) is most likely not O_2 limited. Oxidation resulting from the two sources may explain the slightly divergent conditions needed to create the Fe precipitates observed in the subsurface Fe-rich layer where jarosite and goethite formation are concurrent. The jarosite group minerals are stable/forms at pH <3 and goethite is stable/forms at pHs >3.

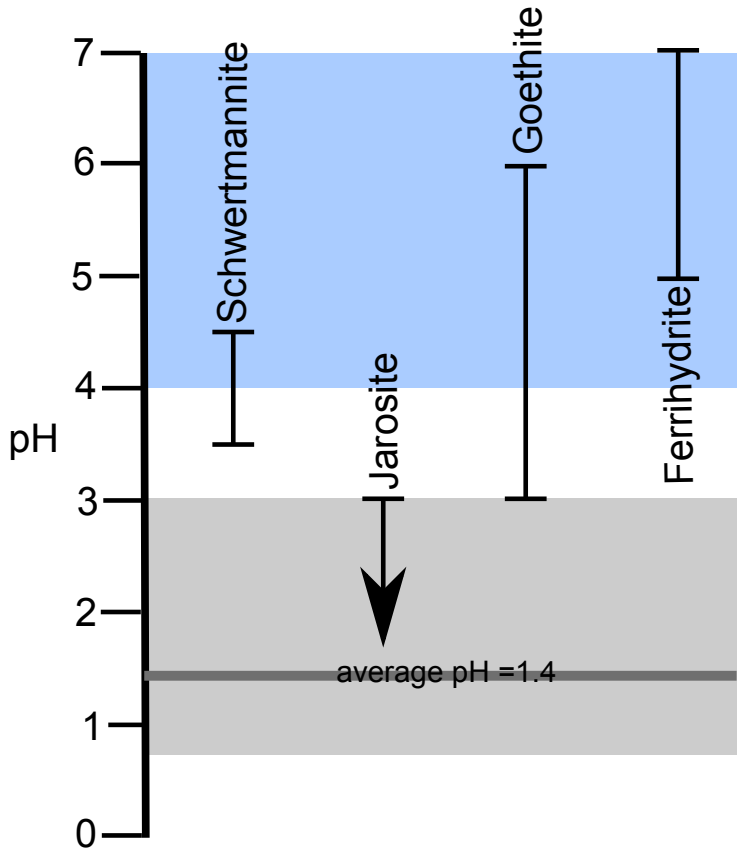

Figure 5.3 – pH ranges associated with precipitation of schwertmannite, jarosite, goethite, and ferrihydrite, relative to the pH of the water at White Island (grey colour) and meteoric water (blue) (modified from (Jones and Renaut, 2007)).

There is a relationship between pH and redox with respect to Fe mineral formation, both are coupled in natural environment(s) on Earth. A modification to the acidic (hydrothermal)/neutralisation (meteoric) flux scenario, suggested earlier, is that during dry weather the hydrothermal waters and gases creates an overall acidic environment in the subsurface. At the point where the hydrothermal systems and atmospheric gases meet (equilibrium point between the two pressurised systems), Fe^{2+} will be oxidised to Fe^{3+}. Oxidisation of Fe will remove acidity and the formation of jarosite would generate acidity keeping the overall pH of the layer low. Dry weather is more conducive to forming jarosite group minerals over goethite/schwertmannite. During wet weather hydrothermal waters and gases would mix with down flowing meteoric waters. This would have a dual affect of oxidising Fe^{3+} and increasing pH from the addition of the near neutral meteoric water.

The formation of the alunite and jarosite provides additional context into the geochemical environment within the subsurface. The formation of the jarosite in the subsurface Fe-rich layers results from the hydrothermal alteration of glass and minerals. Both jarosite and alunite need a oxidising environment to form (Arehart and O'Neil, 1993; Papike et al., 2006). Jarosite can develop instead of alunite under exceptionally low-pH and high-Fe^{3+} activity conditions (Zimbelman et al., 2005). This shows there is geochemical variations in the subsurface Fe-rich layer.

(Reaction 5.6) $K^+ + 3Fe^{3+} + 2SO_4^{-2} + 6H_2O \rightleftarrows KFe_3(SO_4)_2(OH)_6 + 6H^+$ (Jarosite)
(Reaction 5.7) $K^+ + 3Al^{3+} + 2SO_4^{-2} + 6H_2O \rightleftarrows KAl_3(SO_4)_2(OH)_6 + 6H^+$ (Alunite)

The formation of alunite over jarosite largely depends upon the amount of Fe and Al leached/weathered from minerals (Bladh, 1982). The chemical reactions for jarosite (Reaction 5.6) and alunite (Reaction 5.7) are identical except for jarosite needing Fe and alunite needing Al to form. Supergene jarosite may replace alunite of either hypogene or supergene origin in situations where fluids become either more acidic or more oxidizing or both (Stoffregen et al., 2000). Hydrothermal jarosites typically form in highly oxidised, epithermal, near-surface environments of low pH (Desborough et al., 2010). Alunite formation is most likely formed through the hydrothermal alteration, whereas, jarosite formation is related to hydrothermal alteration *and* Fe^{2+} oxidation.

The low pH needed for the formation jarosite may be created as both goethite/jarosite precipitate generating acidity (as shown in Figure 5.2, reactions 5.3 to 5.5, which generate H^+ as Fe-rich minerals form) or by the addition of volcanic gases interacting with the waters to maintain a pH low. The change in the colouration from dominantly reddish colours above subsurface Fe-rich layer to grey/white below the subsurface Fe-rich layers (see Figure 4.4) and the lack of Fe^{3+} minerals points towards a change in oxidation state across the site of the subsurface Fe-rich layer. The subsurface environment transitions from dominantly oxic in the layers above to more anoxic below the subsurface Fe-rich layer. This shows that the subsurface Fe-rich layer represents a dynamic pH, redox zone boundary/change in the subsurface geochemical environment.

The dynamics of this redox zone can be illustrated by using creek water(s) as a proxy for the redox environment in the subsurface fluids. The main source waters feeding the creeks in the Main Crater is from upwelling hydrothermal fluids. There will be some meteoric water influence in the creek waters, it is likely to be limited since there is no storage facility (i.e., lakes) and main storage would be within the crater fill sediments. It is likely the high fluxes of heat, gases, and hydrothermal water will potentially remove the meteoric waters after a rain event. The creek chemistry and redox measurements can be considered to be a good analogue for the subsurface fluid conditions. The creek waters tested were found to carry high dissolved loads of K, Na, Fe and S (see Appendix I) which are the main elements making up the Fe-rich minerals. These creek waters (shown in Figure 5.4) are relatively reducing where the dominant Fe species is Fe^{2+}. Figure 5.4 can be used to understand the formation of Fe-rich minerals from the hydrothermal source (creek fluids (blue dot)) to precipitating Fe-rich minerals. Each arrow illustrates a change Eh/pH conditions that can lead to Fe-rich minerals forming, arrows indicate: 1) increasing Eh (oxidation), 2) mixing with meteoric fluids (yellow dot), 3) increasing pH with no change to redox state of fluid. These potential pathways show that oxidation of the

subsurface fluids will form predominately jarosite, whereas, mixing with meteoric water will form a mix of jarosite, schwertmannite or goethite in the absence of schwertmannite forming (see Figure 4.27). Increasing the pH without changing the redox condition of the creek fluids shows the pH would have to be increased to a pH of <6 before Fe-rich minerals could form. The Eh/pH model shows cycling between 1 and 2 is the most likely scenario to form all minerals seen in the Fe rich subsurface layer. This supports the idea of bimodal O_2 sources. An atmospheric O_2 source which increases Eh not pH and meteoric water which carries dissolved O_2 which increases both Eh and pH.

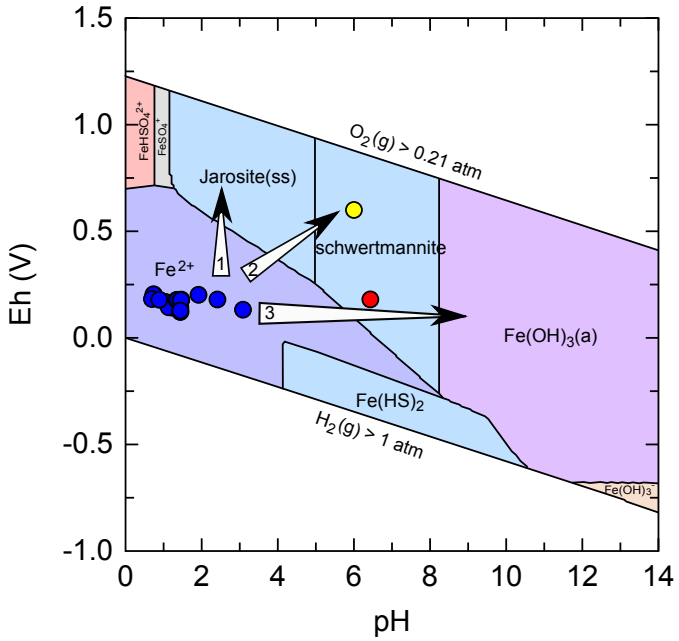

Figure 5.4 – Eh pH Fe mineral stability diagram calculated at 20°C, modified from 4.25B

There are additional processes working within the subsurface and potentially enhancing the kinetics of formation. It is likely the grains of tephra/ash rock of the crater fill are acting as nucleation sites and/or providing some buffering as they are being altered by acidic fluids. The Fe minerals (i.e., magnetite) seen in the fresh crater fill may be acting as seed material for mineral nucleation and/or the clast/mineral surfaces provide nucleation sites (i.e., pyroxenes are high in Fe). Once Fe minerals have started to nucleate the site may enhance abiotic mineral precipitation. At many sites analysed via SEM, goethite was cementing and encasing large well formed jarosite crystals onto the clast surface. This shows the jarosite may be nucleating in solution and growing into large well formed crystals before being included in the layer. Geochemical modelling of SI and Fe mineral stability (Eh pH diagrams) also found that temperature has a positive effect on SI. The amount of undersaturation of schwertmannite decreases as temperature is increases. The Eh/pH stability fields of jarosite and schwertmannite increase as temperature increases.

The age(s) of the subsurface Fe-rich layers are currently unknown, therefore, the rate of formation is unknown. Since the layers are only buried by up to 1.5m of sediment which could mean that the Fe-rich layers are potentially quite young in age. The crater is

constantly being filled with eruptive products from volcanic eruptions (Cole et al., 2000). There are potential subsurface Fe-rich layers which can be observed in the paleo-crater fill/lake sediments in the crater walls (see Figure 4.2) which shows that the formation of the subsurface Fe-rich layers, are likely to be an active ongoing process over an extended period of time. Constant fluxes of upwelling hydrothermal sources (i.e, fluids and gases) are likely to be leading to layering within the subsurface Fe-rich deposits. This could be why thicker layers look like they are made up of multiple cemented layers (see Figure 5.1).

Figure 5.5 is a cross-sectional model is illustrating the different interface zones and changes within the subsurface environment. Fe-rich minerals formation cements the unconsolidated crater fill (Figure 5.5A) into indurated Fe-rich layers (Figure 5.5B). The subsurface Fe-rich layer is forming at the interface zone between where a series transitions are taking place within the subsurface system. The interface chemistry (mixing zone) creates a geochemical environment conducive to forming Fe^{3+}-rich minerals such as jarosite and goethite (see Figure 5.5B). Iron is being concentrated and is becomes immobile as this subsurface Fe-rich layer forms. In the subsurface the high pressure/temperature hydrothermal system interfaces with the atmospheric system above (see Figure 5.5C). The Fe-rich layers are most likely forming at the equilibrium point between high and low pressurise systems. This can be observed in the field, the fluid saturation of the crater sediments stops at the level where the subsurface Fe-rich layers are forming. The change in redox chemistry (i.e., reducing to oxidising), changes the dominant Fe valence across the saturated zone (i.e., Fe^{2+} to Fe^{3+}) (see Figure 5.5D). These changes in redox and Fe valence state further supports that the top of the saturated fluid zone is the equilibrium (mixing zone) between hydrothermal (reducing) and atmospheric (oxidising) systems. The upward fluid and gases flux from the hydrothermal system delivers Fe/S upward. However, without the input of meteoric water and/or atmospheric O_2 changes needed to precipitate Fe-minerals would not be likely. Weathering processes may add Fe and other elements observed in the Fe layers, providing a supplementary source. Additionally fluxes of hydrothermal water and gases carry Fe, S and other nutrients that could be utilised by microbes to the site where the Fe-rich layer are forming. The changes in temperature and pressure as the hydrothermal system mixes with the surface environment creates a habitable zone which could be colonised by microorganisms.

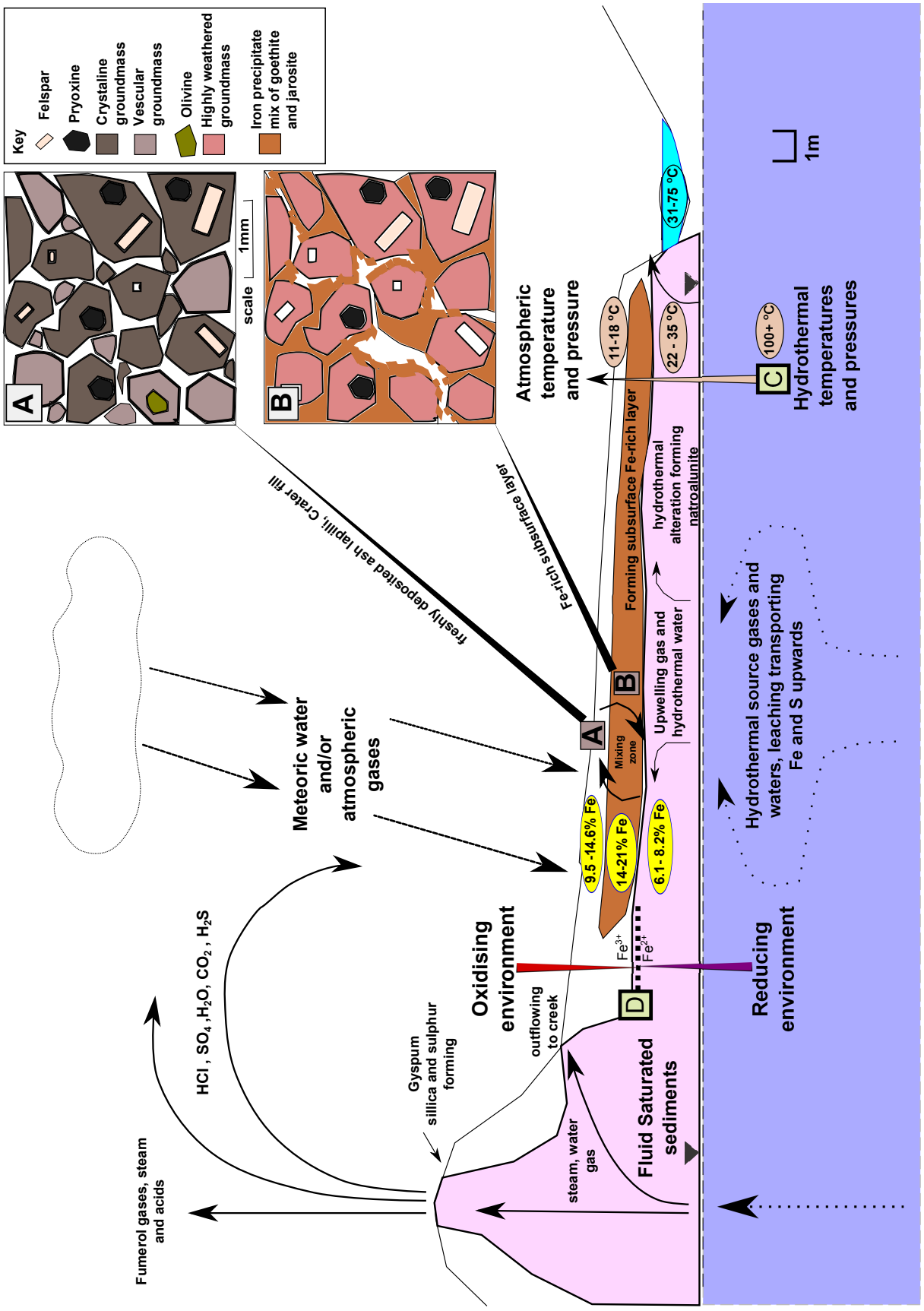

Figure 5.5 – Cross section showing deposition and creation of Fe-rich precipitate layer in White Island geothermal system, A) Fresh crater fill, B) Subsurface Fe-rich layer, C) Hydrothermal temperature and pressure transitions to atmospheric conditions, D) Transition from oxidising to reducing environments and boundary related to Fe chemistry.

5.2 Biogeochemistry

Microbes and algae are present in the creek waters and in the acidic S-rich surface environment of the Main Crater of White Island (see Figure 4.3A). Analyses of creek waters show that the subsurface redox environment is a reducing environment. The hydrothermal fluids carry high dissolved concentrations of metals as well as carrying some life-limiting nutrients necessary for microbial growth (Rogers and Bennett, 2004) (i.e., phosphorus (P), see Appendix I). Both Fe and/or S oxidising microbes prefer reducing environments as they do not have to compete with abiotic Fe oxidation (Taylor and Konhauser, 2011). Additionally the upwards fluxes of hydrothermal gases CO_2, CO and CH_4 (see Appendix D) provides a source of C that could be utilised by microorganisms to create biomass. The subsurface Fe-rich layers are forming at the boundary between oxidising and reducing environments.

SEM analysis of the subsurface layers found that microbes and diatoms are present in the subsurface Fe rich layers (see Figure 4.19). The microbes and diatoms are randomly scattered through the subsurface Fe-rich samples in low numbers. It is hard to discern if microbes that are living in Fe-rich subsurface layers were transported via fluids, or the result of contamination (natural/artificial). The presence of diatoms in the subsurface Fe-rich layers (see Figures 4.19D and 4.19E) potentially shows a downwards migration of meteoric water, transporting surface microbial life into the subsurface Fe-rich layers. Most species of diatoms need sunlight to create food and are commonly found in surface sedimentary environments. It is therefore unlikely that the subsurface Fe-rich layers are the normal habitat for the observed diatoms. However, there are some rare diatom species that can utilise other energy sources and do not need sunlight to survive (Hoover et al., 1986). It is currently unknown if the diatoms in the subsurface Fe-layers are one such species. Microbes may be living in the subsurface Fe-rich layer, but limited amounts of microbes were observed within the subsurface Fe-rich layers. All the microbes observed in the subsurface samples (see Figures 4.19C, 4.19E, 4.19F) look similar in size and shape to some of the microbe species observed in the surface creek (see Figure 4.19A) and hot outflow (see Figure 4.19B). With SEM analysis it was observed that nucleating goethite is shaped similar to individual microbes (Figure4.20B). To detect mineralised microbes visually they need to be distinct entities that can be segregated from their host matrix (Jones and Renaut, 2007). The microbes may be surrounded by and included into the depositing goethite quickly, however, this could not be confirmed. The preparation of samples for SEM dehydration using CPD may have removed loosely fixed microbes from turbidity caused by gas flow and heating of liquid CO_2.

Carbon analysis of C% (by mass) and C isotopes (of solid carbon) found that all the crater fill sediments (surface/subsurface) including the Fe-rich layer have organic carbon between 0.0619 to 0.0988 wt%. The $\delta^{13}C$ isotopic signature of the total carbon was

found to range between -23 to -26.9‰, for organic carbon between -23 to -26.5‰ and the residual between -23 to -30.9‰. Table 5.1 shows δ^{13}C values for various reservoirs, the sub -23‰ values measured in the subsurface samples is characteristic of organic carbon in rock which is primarily derived from life.

Table 5.1 – Isotopic δ^{13}C values for various reservoirs from Sharp (2007)

Reservoir	δ^{13}C (‰ vs.PDB)
Atmosphere (@ 290 PPM)	-6 to -7
Carbonates	0 to 1
Mantle	-5 to -6
Organic carbon in sedimentary rocks	-23 to -30

Looking at Table 5.2, bacteria, diatoms and C3 plants (-22‰) have δ^{13}C isotopic values/ranges similar to those found in the subsurface layers at White Island. There were no plants observed near any of the sampled site of subsurface Fe-rich layers. The only plants found in the main crater area were succulent plants near the old sulphur factory. The C isotopic signal is unlikely to be from plants, pointing towards microbiological life being present in all the subsurface sediments tested.

Table 5.2 – Isotopic δ^{13}C ranges/values for various potential sources

Potential sources	δ^{13}C (‰)	Reference
Plants	-12 to -22	(Sharp, 2007)
Filamentous cyanobacteria	-15 to -20	(Fry and Wainright, 1991)
Diatoms	-15 to -26.9	(Wada et al., 1987; Fry and Wainright, 1991)
Photosynthetic bacteria	-30.2	(Wong and Sackett, 1975)
Sulfur-oxidizing and sulfate-reducing bacteria from a hydrothermal vent field (Lokis Castle)	-26.7 to -39.7	(Jaeschke et al., 2014)

Additionally it was also found that even after digesting the sediment and subsurface Fe-rich layers in 50% hydrogen peroxide for over a month, there was still a low δ^{13}C value in the residual C by wt%. This carbon is most likely locked up in resistant rock and minerals. This indicates that some microbial life may be encased in Fe precipitates or inhabiting other resistant minerals. This is important since dead microbes will denature and brake down quickly and high temperatures, gas flow, acidic water and high amounts of metals and S is not conducive for preservation of organic carbon within the system. There may have been an abundant amount of microbes in the Fe-rich layers and/or the microbes are being encased in resident minerals quickly, preserving organic carbon within the Fe, sediment and rock layers. Species of microbes that are Fe oxidisers are covered with Fe-rich minerals and commonly become encased in Fe minerals as they oxidise Fe.

Figure 5.6A shows the theoretical zone within which the forming subsurface Fe-rich rock and sediments should plot if life is present and being included into the layers during deposition. The total carbon % (by mass) should be more than contamination and less than an organic-rich rock, since the environment is not conducive for organic C preservation. Additionally the rock should have a δ^{13}C value of between -20 to -40‰ similar to other organic rich rocks. If there is no biological involvement in the layer the δ^{13}C isotopic values should be similar to the Loihi basalt, MORB and atmospheric CO_2 (seen in Figure 5.6A) since the deposit is made up of volcanic material. Figure 5.6B shows that the results from this study plot within the zone of a theoretical rock involved with microbes. Figure 5.6B shows that all the total carbon and isotopic values for the samples tested, including the subsurface Fe-rich layers plot above contamination total C wt%, has an isotopic signature that matches up with other organic-rich rocks. This further supports the hypothesis that there is abundant microbial activity within all the subsurface layers of White Island including the subsurface Fe-rich layers.

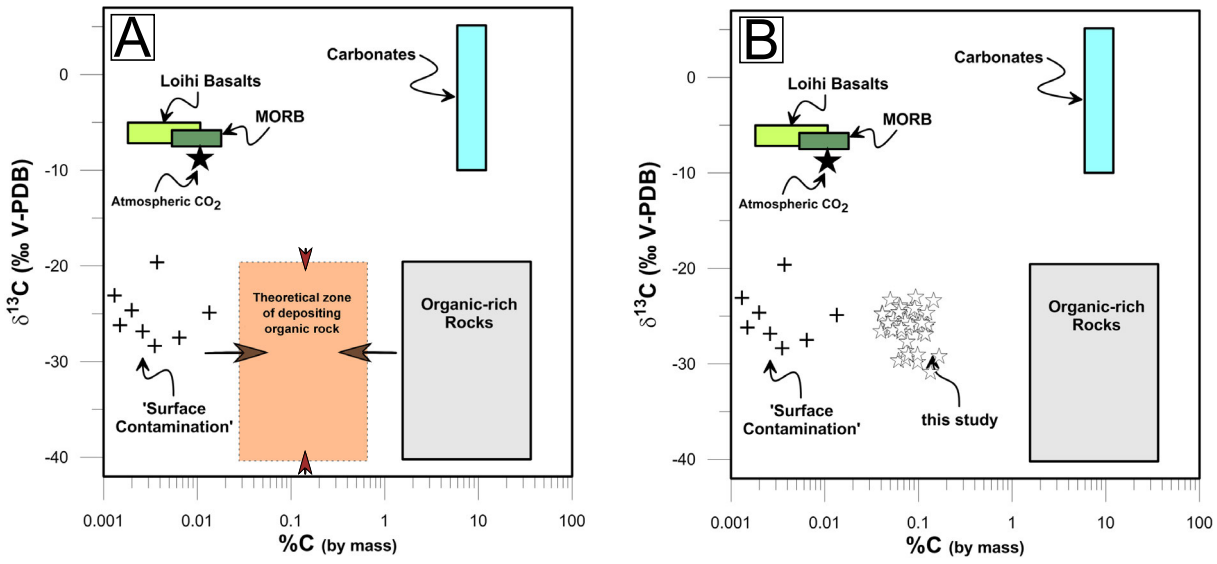

Figure 5.6 – (A) Example of what the theoretical carbon data would look like for a depositing metal rich rock in an acidic environment, δ^{13}C and total carbon values for various reservoirs data compiled from (Mattey et al., 1984; Exley et al., 1986; Sharp, 2007). (B) Results δ^{13}C vs mass % C data, for all samples carbon site 1,2 and subsurface Fe-rich layers.

It should also be noted that microbes may be actively or passively involved in the formation of the subsurface Fe-rich layers. Recognising abiotic driven Fe precipitation over biotic can be hard to recognise since the resulting Fe precipitates are often visually and chemically similar. Organic carbon is present in the subsurface environment sourced from either microbes present in the subsurface Fe-rich layer and/or transported into the site. The addition of organic carbon into the Fe-rich layer may be helping Fe minerals to nucleate, biological byproducts may be sticking to the volcanic clasts and could explain

the nuclating goethite on the mineral surfaces. The constant fluxes of CO_2, CO and/or CH_4 moving through the crater fill sediments are likely providing the C required by microorganisms to create biomass, where microbial activity in the subsurface environment locks some of the normally mobile C within the subsurface. Organic surfaces (surface of microbes/EPS) and organic carbon can act as nucleation sites in reducing acidic environments (Greenwood et al., 2013). Sequenced-based microbial investigations are required to identify the types of microorganisms present in each layer; this will provide a better overview of the potential interactions occurring in each subsurface layer.

5.3 Implications of subsurface Fe-rich layer formation

The subsurface Fe-rich layers are forming above an highly active volcanic hydrothermal system. This system actively degases through permeable sections of the crater floor at White Island, releasing large amounts of volcanic gas into the atmosphere (Giggenbach and Matsuo, 1991; Bloomberg, 2012; Letham-Brake, 2013). It is likely that the formation of the Fe-rich layers are changing the physical properties of the crater fill substrate (i.e, the forming minerals are cementing the sediments into cohesive layers). The formation of impermeable and/or reduced permeability can lead to increased hydrostatic pressure of a hydrothermal system (Foote, 2012). Work done by Letham-Brake (2013) found that the hard subsurface Fe-rich layers at site 5 (see Figure 4.1) had reduced permeability and porosity properties when compared to unconsolidated crater fill. Permeability reduced from $3.36E^{-12}$ kgas (m^2) (crater fill) down to between $3.04E^{-12}$ - $2.63E^{-12}$ kgas (m^2) and the open porosity reduced from 35% (ϕ connected porosity) down to between 21-24% (ϕ connected porosity). The formation of the hard subsurface Fe-rich layer(s) may have a pressure cooker effect increasing the hydrostatic pressure, which in turn may be increasing the intensity of the hydrothermal alteration in the layers below. Field observations support this possibility where sediments beneath the Fe-rich subsurface layer are saturated with water and alteration products. The constant fluid saturation of the sediments below the subsurface Fe-rich layers may be a consequence of increased hydrostatic pressure. As well as the abundant formation of alteration products below the layers and the temperature change across the layers, all point towards the possibility that the formation of Fe-rich layers may already affecting the gas/fluid flux(s) within the subsurface. The formation of the layers may be enhancing the potential of a hydrothermal eruption within the hydrothermal system at White Island.

Another outcome from the subsurface Fe-rich layers forming is that the organic carbon and associated biosignatures are being preserved (locked) into stable mineral layers. These layers may potentially lead to the longer term preservation of the microbial evidence within the hostile environment created by the volcanic system. This may be important for future studies looking for life within modern and paleo volcanic/hydrothermal environments. Alternatively the Fe-rich minerals/layers may be the best sites to target to identify the

potential of past life on Mars. Epithermal systems are generally stable long lived systems up to millions of years (Sillitoe, 1994) and commonly provide the necessary elements for microbial life to thrive. The mineral formation in the epithermal zone will potentially preserve any biosignature (organic carbon) (Walker et al., 2005). The carbon isotopic and C wt% data from this study was compared to data from a paleo-epithermal system (the Berlins porphyry). Evidence of microbial activity was found in Fe-rich concretions that formed in the Berlins porphyry (Cox, 2013). When the carbon data from the Berlins porphyry and the modern active White Island system were compared a clear correlation of biological C data was discovered between δ^{13}C isotopic and total C wt% values. This shows the isotopic analysis method used in this study may prove to be a valuable tool that can be applied to investigations within both active and paleo-epithermal systems.

Chapter 6: Conclusion

6.1 Conclusion

The mineralogy of the subsurface Fe-rich layers is relatively simple. The layers are primarily comprised of jarosite and goethite cementing together volcaniclastic sediments. The geochemical process(es) leading to the formation of the subsurface layers are more complex and can be constrained as presented in this thesis through geochemical and biogeochemical investigations. The layers are forming at an active redox boundary, which is a mixing interface between upwelling hydrothermal fluids/gases and downwelling atmospheric fluids/gases. Additionally cyclic mixing of sources, driven by wet (meteoric water) and dry spells (O_2 gas) are most likely leading to the mix of Fe-rich minerals seen in the subsurface layers.

The nature and abidance of microbiology in relation to the subsurface Fe-rich layers is not so simple. Observations presented here only confirm that microbes are present in the layers. To date the exact number and type of microbial species and their biogeochemical functions within the subsurface environment have not been determined. Carbon chemistry demonstrates that microbial life permeates the sediment layers and is potentially more abundant then first thought. The carbon chemistry is maintained despite chemical extractions providing additional context between microbial proliferation and preservation. Organic carbon in a acidic environment would degrade quickly and likely be removed by the upwards flux of fluid and gases. This shows that either the microbes and/or byproducts are becoming encased quickly by minerals or that the microbes are alive as they become encased. As shown in this thesis microbes and/or microbial activity could influence the deposition of subsurface Fe-rich layers, but the full scope of microbial interactions with the Fe-layers and chemistry in the subsurface is still unknown. Potentially microbial interactions are affecting the dynamics and kinetics of subsurface Fe chemistry on a microscopic scale leading to the deposition of the subsurface Fe-rich layers, which can have affects at macroscopic scales within an volcanic system.

Hydrothermal and volcanic systems are often viewed as being barren and lifeless. What is clear from this study is that these are not sterile environments. The Main Crater at White island initially looks to be completely devoid of life. On closer investigation, sections of the creeks in the Main Crater have large amounts of microbial fibres fixed to rocks that could easily be missed. The depth of sediments sampled and tested during this study was confined to accessible sections across the subsurface Fe-rich layers. The depth to which microorganisms inhabit the subsurface system could penetrate deep into the

epithermal system based on the close correlation between carbon chemistry data from the Berlins porphyry. Additionally organic carbon being preserved into the Fe-rich layers is contiguously important, especially in an active volcanic system. Without some mechanism of preservation any evidence of microbial activity would be degraded and lost overtime. This shows that interface sites and forming Fe deposits could be key sites to target when looking for evidence of life in hydrothermal and epithermal systems. Microbial life maybe more pervasive at interface sites and throughout the subsurface environment at White Island and in other volcanic systems worldwide or on other planets and satellites.

References

Acero, P., Ayora, C., Torrentó, C., and Nieto, J. M. (2006). The behavior of trace elements during schwertmannite precipitation and subsequent transformation into goethite and jarosite. Geochimica et Cosmochimica Acta, 70(16):4130–4139.

Amils, R., González-Toril, E., Fernández-Remolar, D., Gómez, F., Aguilera, A., Rodríguez, N., Malki, M., García-Moyano, A., Fairén, A. G., de la Fuente, V., and Luis Sanz, J. (2007). Extreme environments as Mars terrestrial analogs: The Rio Tinto case. Planetary and Space Science, 55(3):370–381.

Arehart, G. B. and O'Neil, J. R. (1993). D/H ratios of supergene alunite as an indicator of paleoclimate in continental settings. Geophysical Monograph Series, (78):277–284.

Bibi, I., Singh, B., and Silvester, E. (2011). Akaganéite (β-FeOOH) precipitation in inland acid sulfate soils of south-western New South Wales (NSW), Australia. Geochimica et Cosmochimica Acta, 75(21):6429–6438.

Bigham, J., Schwertmann, U., and Pfab, G. (1996a). Influence of pH on mineral speciation in a bioreactor simulating acid mine drainage. Applied Geochemistry, 11(6):845–849.

Bigham, J., Schwertmann, U., Traina, S., Winland, R., and Wolf, M. (1996b). Schwertmannite and the chemical modeling of iron in acid sulfate waters. Geochimica et Cosmochimica Acta, 60(12):2111–2121.

Bigham, J. M. and Nordstrom, D. K. (2000). Iron and Aluminum Hydroxysulfates from Acid Sulfate Waters. Reviews in Mineralogy and Geochemistry, 40(1):351–403.

Black, P. M. (1970). Observations on white island volcano, New Zealand. Bulletin Volcanologique, 34(1):158–167.

Bladh, K. W. (1982). The formation of goethite, jarosite, and alunite during the weathering of sulfide-bearing felsic rocks. Economic Geology, 77(1):176–184.

Bloomberg, S. H. (2012). Looking for permeability: Mass and heat flow assessment using high resolution soil CO2 flux surveys within the taupo volcanic zone, New Zealand. Msc thesis, Canterbury University.

Brown, D., Sherriff, B. L., Sawicki, J., and Sparling, R. (1999). Precipitation of iron minerals by a natural microbial consortium. Geochimica et Cosmochimica Acta, 63(15):2163–2169.

Browne, P. and Cole, J. (1973). Surveillance of White Island volcano, 1968-1972. New Zealand Journal of Geology and Geophysics, 16(4):959–963.

Burgos, W. D., Borch, T., Troyer, L. D., Luan, F., Larson, L. N., Brown, J. F., Lambson, J., and Shimizu, M. (2012). Schwertmannite and Fe oxides formed by biological low-pH Fe(II) oxidation versus abiotic neutralization: Impact on trace metal sequestration. Geochimica et Cosmochimica Acta, 76:29–44.

Burns, B. P., Anitori, R., Butterworth, P., Henneberger, R., Goh, F., Allen, M. A., Ibañez–Peral, R., Bergquist, P. L., Walter, M. R., and Neilan, B. A. (2009). Modern analogues and the early history of microbial life. Precambrian Research, 173(1-4):10–18.

Butterworth, P. (2004). Under the Microscope White Island : a sulphur-rich hydrothermal system. Microbiology Australia, (March):28–29.

Cole, J., Thordarson, T., and Burt, R. (2000). Magma Origin and Evolution of White Island (Whakaari) Volcano, Bay of Plenty, New Zealand. Journal of Petrology, 41(6):867–895.

Cox, T. L. (2013). Petrological and geochemical evidence for putative ancient microfossils within the Berlins porphyry, New Zealand. Msc thesis, University of Canterbury.

Cundy, A. B., Hopkinson, L., and Whitby, R. L. D. (2008). Use of iron-based technologies in contaminated land and groundwater remediation: a review. The Science of the total environment, 400(1-3):42–51.

Curtis, C. D. (2003). The aqueous geochemistry of metals in the weathering environment: strengths and weaknesses in our understanding of speciation and process. Mineralogical Magazine, 67(2):235–246.

Desborough, G. A., Smith, K. S., Lowers, H. A., Swayze, G. A., Hammarstrom, J. M., Diehl, S. F., Leinz, R. W., and Driscoll, R. L. (2010). Mineralogical and chemical characteristics of some natural jarosites. Geochimica et Cosmochimica Acta, 74(3):1041–1056.

Donachie, S. P., Christenson, B. W., Kunkel, D. D., Malahoff, A., and Alam, M. (2002). Microbial community in acidic hydrothermal waters of volcanically active White Island, New Zealand. Extremophiles : life under extreme conditions, 6(5):419–25.

Downs, R. T. (2006). The RRUFF Project: an integrated study of the chemistry, crystallography, Raman and infrared spectroscopy of minerals. Program and Abstracts of the 19th General Meeting of the International.

Ece, O. I., Schroeder, P. A., Smilley, M. J., and Wampler, J. M. (2008). Acid-sulphate hydrothermal alteration of andesitic tuffs and genesis of halloysite and alunite deposits in the Biga Peninsula, Turkey. Clay Minerals, 43(2):281–315.

Exley, R., Mattey, D., Clague, D., and Pillinger, C. (1986). Carbon isotope systematics of a mantle hotspot: a comparison of Loihi Seamount and MORB glasses. Earth and Planetary Science Letters, 78(2-3):189–199.

Foote, L. C. (2012). Experimental Modelling of Fragmentation Processes within Phreatic and Hydrothermal Eruptions. Msc, University of Canterbury.

Fortin, D. and Langley, S. (2005). Formation and occurrence of biogenic iron-rich minerals. Earth-Science Reviews, 72(1-2):1–19.

Frost, R. L., Wills, R. A., Weier, M. L., Martens, W., and Mills, S. (2006). A Raman spectroscopic study of selected natural jarosites. Spectrochimica acta. Part A, Molecular and biomolecular spectroscopy, 63(1):1–8.

Fry, B. and Wainright, S. (1991). Diatom sources of 13C-rich carbon in marine food webs. Marine Ecology Progress Series, 76:149–157.

Giggenbach, W. (1987). Redox processes governing the chemistry of fumarolic gas discharges from White Island, New Zealand. Applied Geochemistry, 2(2):143–161.

Giggenbach, W. and Matsuo, S. (1991). Evaluation of results from Second and Third IAVCEI Field Workshops on Volcanic Gases, Mt Usu, Japan, and White Island, New Zealand. Applied Geochemistry, 6(2):125–141.

Giggenbach, W. F., Shinohara, H., Kusakabe, M., and Ohba, T. (2003). Formation of acid volcanic brines through interaction of magmatic gases, seawater and rock within the White Island volcanic-hydrothermal system, New Zealand. Society of Economic Geologists Special Publication, Number 10, 10:19–40.

Gray, J. E. and Coolbaugh, M. F. (1994). Geology and Geochemistry of Summitville , Colorado: An Epithermal Acid Sulfate Deposit in a Volcanic Dome. Economic Geology, 89(8):1906–1923.

Greenwood, P., Brocks, J., Grice, K., Schwark, L., Jaraula, C., Dick, J., and Evans, K. (2013). Organic geochemistry and mineralogy. I. Characterisation of organic matter associated with metal deposits. Ore Geology Reviews, 50:1–27.

Hamasaki, S. (2002). Volcanic-related alteration and geochemistry of Iwodake volcano, Satsuma Iwojima, Kyushu, SW Japan. Earth Planets and Space, 54(3):217–229.

Haughton, B. F. and Nairn, I. A. (1991). The 1976-1982 Strombolian and phreatomagmatic eruptions of White Island, New Zealand: eruptive and depositional mechanisms at a 'wet' volcano. Bulletin of volcanology, pages 25–49.

Hedenquist, J. W. and Lowenstern, J. B. (1994). The role of magmas in the formation of hydrothermal ore deposits. Nature, 370(6490):519–527.

Hedenquist, J. W., Simmons, S. F., Giggenbach, W. F., and Eldridge, C. S. (1993). White Island, New Zealand, volcanic-hydrothermal system represents the geochemical environment of high-sulfidation Cu and Au ore deposition. Geology, 21(8):731.

Hoover, R. B., Hoyle, F., Wickramasinghe, N. C., Hoover, M. J., and Al-Mufti, S. (1986). Diatoms on earth, comets, europa and in interstellar space. Earth, Moon and Planets, 35(1):19–45.

Ibáñez–Peral, R. (2008). Analysis of Microbial Diversity in an Extreme Environment : White Island , New Zealand. Phd thesis, Macquarie University.

Jaeschke, A., Eickmann, B., Lang, S. Q., Bernasconi, S. M., Strauss, H., and Früh-Green, G. L. (2014). Biosignatures in chimney structures and sediment from the Loki's Castle low-temperature hydrothermal vent field at the Arctic Mid-Ocean Ridge. Extremophiles : life under extreme conditions, 18(3):545–60.

Johnson, D. B. and Hallberg, K. B. (2003). The microbiology of acidic mine waters. Research in microbiology, 154(7):466–73.

Jones, B. and Renaut, R. W. (2007). Selective mineralization of microbes in Fe-rich precipitates (jarosite, hydrous ferric oxides) from acid hot springs in the Waiotapu geothermal area, North Island, New Zealand. Sedimentary Geology, 194(1-2):77–98.

Kappler, A. and Straub, K. L. (2005). Geomicrobiological Cycling of Iron. Reviews in Mineralogy and Geochemistry, 59(1):85–108.

Kawano, M. and Tomita, K. (2001). Geochemical modeling of bacterially induced mineralization of schwertmannite and jarosite in sulfuric acid spring water. American Mineralogist, 86:1156–1165.

Kinniburgh, D. and Cooper, D. (2014). PhreePlot: Creating graphical output with PHREEQC.

Konhauser, K. O., Kappler, A., and Roden, E. E. (2011). Iron in Microbial Metabolisms. Elements, 7(2):89–93.

Kozubal, M. A., Macur, R. E., Jay, Z. J., Beam, J. P., Malfatti, S. A., Tringe, S. G., Kocar, B. D., Borch, T., and Inskeep, W. P. (2012). Microbial iron cycling in acidic geothermal springs of yellowstone national park: integrating molecular surveys, geochemical processes, and isolation of novel fe-active microorganisms. Frontiers in microbiology, 3(March):109.

Letham-Brake, M. J. (2013). Geological constraints on fluid flow at Whakaari volcano (White Island). Msc thesis, Canterbury University.

Majzlan, J., Navrotsky, A., and Schwertmann, U. (2004). Thermodynamics of iron oxides: Part III. Enthalpies of formation and stability of ferrihydrite ($\sim Fe(OH)_3$), schwertmannite ($\sim FeO(OH)_{3/4}(SO_4)_{1/8}$), and ϵ-Fe_2O_3. Geochimica et Cosmochimica Acta, 68(5):1049–1059.

Mathur, R., Dendas, M., Titley, S., and Phillips, A. (2011). Patterns in the Copper Isotope Composition of Minerals in Porphyry Copper Deposits in Southwestern United States. Economic Geology, 105(8):1457–1467.

Mattey, D., Carr, R., Wright, I., and Pillinger, C. (1984). Carbon isotopes in submarine basalts. Earth and Planetary Science Letters, 70(2):196–206.

Mongillo, M. A. and Wood, C. P. (2000). Thermal infrared mapping of White Island volcano , New Zealand. Journal of Volcanology and Geothermal Research, 69(June 1994):59–71.

Moon, V., Bradshaw, J., and de Lange, W. (2009). Geomorphic development of White Island Volcano based on slope stability modelling. Engineering Geology, 104(1-2):16–30.

Moon, V., Bradshaw, J., Smith, R., and de Lange, W. (2005). Geotechnical characterisation of stratocone crater wall sequences, White Island Volcano, New Zealand. Engineering Geology, 81(2):146–178.

Nealson, K. H., Belz, A., and McKee, B. (2002). Breathing metals as a way of life: geobiology in action. Antonie van Leeuwenhoek, 81(1-4):215–22.

Papike, J., Karner, J., and Shearer, C. (2006). Comparative planetary mineralogy: Implications of martian and terrestrial jarosite. A crystal chemical perspective. Geochimica et Cosmochimica Acta, 70(5):1309–1321.

Parkhurst, D. and Appelo, C. (2013). and examples for PHREEQC version 3- A computer program for speciation, batch-reaction, one-dimensional transport, and inverse geochemical calculations. Technical report, U.S. Geological Survey Water-Resources.

Raymahashay, B. C. (1968). A geochemical study of rock alteration by hot springs in the Paint Pot Hill area, Yellowstone Park. Geochimica et Cosmochimica Acta, 32(5):499–522.

Reich, M., Zúñiga, A., Amigo, A., Vargas, G., Morata, D., Palacios, C., Ángel, M., and Garreaud, R. D. (2009). Formation of cristobalite nanofi bers during explosive volcanic eruptions. Geology, 37(5):435–438.

Rogers, J. R. and Bennett, P. C. (2004). Mineral stimulation of subsurface microorganisms: release of limiting nutrients from silicates. Chemical Geology, 203(1-2):91–108.

Sanders, L. (1998). A manual of field hydrogeology. page 381. Prentice Hall, illustrate edition.

Scher, S., Williams-Jones, A. E., and Williams-Jones, G. (2013). Fumarolic Activity, Acid-Sulfate Alteration, and High Sulfidation Epithermal Precious Metal Mineralization in the Crater of Kawah Ijen Volcano, Java, Indonesia. Economic Geology, 108(5):1099–1118.

Sharp, Z. (2007). Principles of stable isotope geochemistry. page 344. Prentice Hall.

Sillitoe, R. and Hedenquist, J. (2003). Linkages between volcanotectonic settings, ore-fluid compositions, and epithermal precious metal deposits. Society of Economic Geologists Special Publication, Number 10, 10:285–314.

Sillitoe, R. H. (1994). Erosion and collapse of volcanoes: Causes of telescoping in intrusion-centered ore deposits. Geology, 22(10):945.

Slansky, E. (1975). New Zealand Journal of Natroalunite and alunite from White Island volcano , Bay of Plenty , New Zealand. New Zealand Journal of Geology and Geophysics, 18(2):285–293.

Southam, G. (2012). Minerals as Substrates for Life: The Prokaryotic View. Elements, 8(2):101–106.

Stoffregen, R. E., Alpers, C. N., and Jambor, J. L. (2000). Alunite-Jarosite Crystallography, Thermodynamics, and Geochronology. Reviews in Mineralogy and Geochemistry, 40(1):453–479.

Taylor, K. G. and Konhauser, K. O. (2011). Iron in Earth Surface Systems: A Major Player in Chemical and Biological Processes. Elements, 7(2):83–88.

Wada, E., Terazaki, M., Kabaya, Y., and Nemoto, T. (1987). 15N and 13C abundances in the Antartic Ocean with emphasis on the biogeochemical structure of the food web. Deep Sea Research Part A. Oceanographic Research Papers, 34(5-6):829–841.

Walker, J. J., Spear, J. R., and Pace, N. R. (2005). Geobiology of a microbial endolithic community in the Yellowstone geothermal environment. Nature, 434(April):861–864.

Warren, L. A. and Kauffman, M. E. (2003). Geoscience. Microbial geoengineers. Science (New York, N.Y.), 299(5609):1027–9.

White, N. C. and Hedenquist, J. W. (1990). Epithermal environments and styles of mineralization: Variations and their causes, and guidelines for exploration. Journal of Geochemical Exploration, 36(1-3):445–474.

Wong, W. and Sackett, W. M. (1975). Isotope Fractionation in Photosynthetic Bacteria during Carbon Dioxide Assimilation. Plant physiology, 55(3):475–9.

Wood, C. P. (1994). Mineralogy at the magma-hydrothermal system interface in andesite volcanoes , New Zealand. Geology, 22(1):75–78.

Zhu, J., Gan, M., Zhang, D., Hu, Y., and Chai, L. (2013). The nature of Schwertmannite and Jarosite mediated by two strains of Acidithiobacillus ferrooxidans with different ferrous oxidation ability. Materials science engineering. C, Materials for biological applications, 33(5):2679–85.

Zimbelman, D., Rye, R., and Breit, G. (2005). Origin of secondary sulfate minerals on active andesitic stratovolcanoes. Chemical Geology, 215(1-4):37–60.

Appendix A Base map data sources

Data used to create Figure 2.1 DEM, Topomap and Place names.

Data used to create Figure 2.2 Aerial photos, Place names.

Data used to create Figure 3.1 Aerial photos, Place names.

Data used to create Figure 4.1 Aerial photos, Place names.

Aerial photos

Sourced from the LINZ Data Service (https://data.linz.govt.nz/layer/1760-bay-of-plenty-025m-rural-aerial-photos-2011-2012/) and licensed by (BOPLASS Limited) for re-use under the Creative Commons Attribution 3.0 New Zealand licence.

DEM

Sourced from the LINZ Data Service (https://data.linz.govt.nz/layer/1768-nz-8m-digital-elevation-model-2012/) and licensed by (Geographx, Land Information New Zealand (LINZ)) for re-use under the Creative Commons Attribution 3.0 New Zealand licence.

Topomap

Sourced from the LINZ Data Service (https://data.linz.govt.nz/layer/767-nz-mainland-topo50-maps/) and licensed by (LINZ) for re-use under the Creative Commons Attribution 3.0 New Zealand licence.

Place names

Sourced from the Koordinates Data Service (https://koordinates.com/layer/284-nz-placenames-march-2008/) and licensed by (Suze Mavoa) for re-use under the Creative Commons Attribution 3.0 New Zealand licence." Sourced from Land Information New Zealand, 2008. Crown copyright reserved. www.linz.govt.nz

Appendix B Representative chemical analyses for individual eruption units at White Island from (Cole et al., 2000)

E no.:	E1	E1	E2	E3	E4	E5?	E5
Location:	1977-1982	1977-1982	Central Cone Pakihikura	Central Cone Mt Gisborne	Central Cone SW lava	Central Cone Club Rocks	Central Cone Otaketa Pt
Type:	1977 block	1977 bomb	scoria fall				Lava 3
Sample	P41600	TRW-35	TRW-7	RW-40	TRW-28	RW-14	TRW-2
SiO_2	55.94	58.05	56.59	63.28	60.39	56.97	60.21
TiO_2	0.63	0.61	0.65	0.79	0.68	0.59	0.50
Al_2O_3	13.26	13.80	15.76	14.71	15.41	17.12	15.21
FeO	7.33	7.66	8.01	6.25	7.27	8.03	6.66
MnO	0.14	0.14	0.15	0.11	0.13	0.15	0.13
MgO	10.14	7.80	5.98	3.35	4.05	3.97	4.44
CaO	8.69	8.26	8.47	5.50	6.27	7.90	7.01
Na_2O	2.39	2.38	2.30	3.22	2.61	2.62	2.82
K_2O	1.15	1.36	1.15	2.22	1.46	1.07	1.42
P_2O_5	0.07	0.08	0.08	0.13	0.09	0.08	0.07
LOI	0.00	-0.16	1.38	0.10	1.94	0.16	1.12
S	n.a.	0.01	0.04	n.a.	0.01	n.a.	0.03
total	100.77	99.99	100.56	99.67	100.32	98.66	99.62

E no.:	E6	E7	E8	E9	E10	Average
Location:	Central Cone Otaketa Pt	Central Cone North Bench	Troup Head Wilson Bay	Troup Head Wilson Bay	Central Cone Shark Bay	of all samples
Type:	Lava 2			Basal Lava		
Sample	TRW-61	TRW-12	RW-2	RW-4	TRW-47	
SiO_2	61.86	62.10	59.03	57.21	58.67	59.19
TiO_2	0.72	0.72	0.60	0.57	0.61	0.64
Al_2O_3	14.52	14.63	15.95	16.40	14.65	15.12
FeO	6.44	6.20	7.75	8.13	7.05	7.23
MnO	0.11	0.11	0.15	0.13	0.14	0.13
MgO	3.73	3.57	4.41	3.82	6.44	5.14
CaO	5.95	5.79	7.57	7.89	8.47	7.31
Na_2O	3.10	2.79	2.60	2.57	2.52	2.66
K_2O	2.09	2.21	1.32	1.06	1.37	1.49
P_2O_5	0.11	0.10	0.08	0.08	0.08	0.09
LOI	0.33	1.88	0.26	0.67	0.03	0.64
S	0.00	0.04	n.a.	n.a.	0.00	0.03
total	98.95	100.14	99.71	98.52	100.48	99.68

Note: The table has been edited from Cole et al. (2000) (Table 3), the data from Ngatoro Cone has not been used since its not representative of the material in the central crater, since the lavas and pyroclastics are a product of an earlier cone building sequence.

Appendix C Water temperature, pH and metal/solutes minimum maximum and averages for crater lake,surface features and creeks at White Island from GNS Science Geothermal and Groundwater Database

C.1 Crater Lake

	pH	Aluminium	Ammonium	Arsenic	Boron	Bromine	Calcium	Chloride	Copper	Fluorine	Iron
minimum	-0.68	344.00	158.00	0.10	30.00	62.00	1734.00	28823.00	0.003	116.00	1944.00
maximum	1.48	7600.00	200.00	111.00	211.00	364.00	7506.00	132251.00	19.000	1410.00	12110.00
Average	0.16	2567.80	179.00	15.53	108.78	171.00	3543.60	72809.63	3.780	470.42	4541.95
sample count	69	65	2	65	65	67	65	68	62	67	65

Lithium	Magnesium	Nitrate	Nitrogen	Phosphorus	Potassium	Silicon	Sodium	Sulphate	Sulphide	Temperature ℃
6.60	2112.00	0.02	31.00	0.04	741.00	83.00	6023.00	3200.00	0.01	14.00
39.00	9352.00	7.50	188.00	12.50	4462.00	515.00	29550.00	37612.00	0.47	74.20
16.77	4565.00	2.33	94.44	6.46	2028.48	234.29	12305.81	15126.28	0.06	53.72
65	66	57	63	29	66	65	65	67	64	68

C.2 Surface features

	pH	Aluminium	Ammonium	Arsenic	Boron	Bromine	Calcium	Chloride	Fluorine	Iron
minimum	-0.65	0.10	0.30	0.02	0.10	0.39	120.00	124.00	1.30	0.05
maximum	5.53	4681.00	210.00	45.00	318.00	136.00	6336.00	104614.00	448.00	4781.00
Average	2.09	549.20	43.62	1.71	31.46	36.97	1567.51	18258.47	66.08	1122.00
sample count	224	224	22	219	223	225	224	227	220	224

Lithium	Magnesium	Nitrate	Nitrogen	Phosphorus	Potassium	Silicon	Sodium	Sulphate	Sulphide	Temperature ℃
0.05	61.00	0.02	0.01	0.00	17.30	146.00	34.00	660.00	0.01	18.00
30.00	7316.00	2.80	360.00	2.00	2103.00	497.00	13700.00	22438.00	2.90	100.90
4.99	1403.64	0.46	64.26	0.52	363.54	346.13	3393.02	4137.00	0.14	88.24
224	224	166	200	64	224	224	224	227	217	227

C.3 Creeks

	pH	Aluminium	Ammonium	Arsenic	Boron	Bromine	Calcium	Chloride	Fluorine	Iron
minimum	-0.48	9.40	2.10	0.01	3.30	1.40	465.00	1433.00	3.00	125.00
maximum	2.93	6733.00	16.70	18.90	80.00	126.00	4136.00	93711.00	462.00	3831.00
average	1.19	1670.60	10.93	3.16	45.23	51.51	1928.49	25277.22	99.85	1529.85
sample count	78	72	3	72	72	140	72	139	136	72

Lithium	Magnesium	Nitrate	Nitrogen	Phosphorus	Potassium	Silicon	Sodium	Sulphate	Sulphide	Temperature ℃
0.48	482.00	0.02	3.60	0.08	75.00	170.00	536.00	825.00	0.01	17.30
31.00	3639.00	5.10	107.00	4.00	3810.00	444.00	12580.00	32387.00	0.15	95.10
9.10	1904.50	0.59	52.05	0.78	925.15	327.75	5601.67	6491.42	0.04	47.74
72	72	107	68	50	72	72	72	139	71	156

Note units are: all rounded to 2 decimal places (except copper 3 decimal places), Acidity pH units, Aluminium mg/L All forms as Al - filterable, Ammonium mg/L as N - total, Arsenic mg/L All forms as As - filterable, Boron mg/L - All forms as B - filterable, Bromine mg/L (bromide) as Br - filterable, Calcium mg/L - All Forms as Ca - filterable, Chloride mg/L as Cl - filterable, Copper mg/L All forms as Cu - filterable, Fluorine mg/L (fluoride) as F - filterable, Iron mg/L All forms as Fe - filterable, Lithium mg/l - All forms as Li - filterable, Magnesium mg/L - All Forms as Mg - filterable, Nitrate mg/L as N - filterable, Nitrogen mg/L All forms ammonia as NH3 - total, Phosphorus mg/L as P- Reactive - filterable, Potassium mg/L - All Forms as K -filterable, Silicon mg/L All forms as SiO2 - filterable, Sodium mg/L - All Forms as Na - filterable, Sulphate mg/L as SO4 - filterable, Sulphide mg/L as H2S - total, Temperature Deg. C

Appendix D Chemical composition of White Island gas discharges (μmol/mol)

No.	Date	°C	H_2O	H_2	CO_2	CO	CH_4	S_t	n_s	HCl	NH_3	N_2	Ar
Donald Mound													
W1	8.74	122	632000	240	323000	-	8.4	42500	3.8	44	-	1580	-
W2	11.74	400	898000	366	61200	1.8	1.8	27900	0.6	12040	1.6	360	1.03
W3	5,75	560	949000	354	37000	3.6	7.9	8000	1.9	4590	20.3	240	0.48
W4	11.75	105	961000	123	35800	1.7	12.2	2800	3.9	102	4.0	205	0.12
W5	4.76	100	900000	141	96700	>1.0	10.1	3400	3.9	152	0.9	280	1.78
W6	12.76	100	836000	46	146300	1.3	1.0	14400	3.9	2460	10.4	770	1.50
W7	5.77	195	932000	57	48100	1.4	0.7	15300	-0.8	2880	270.0	745	4.94
W8	2.78	445	876000	3010	83500	44.6	3.5	31700	1.7	4960	42.0	510	1.11
W9	8.78	540	881000	2380	98100	53.7	3.3	15600	1.6	2260	6.0	430	0.47
W10	11.79	512	575000	895	367200	52.0	2.6	52400	2.7	2940	5.1	2220	2.15
South to North Traverse													
WA	2.84	106	951000	19	44200	>0.3	65.0	3900	0.8	60	0.3	280	0.58
WB	2.84	760	952000	3020	52900	42.3	10.2	10600	2.6	5180	54.1	210	1.02
WC	2.84	457	941000	540	29100	8.7	3.0	16500	2.8	12450	49.0	180	0.41
WD	2.84	197	947000	21	40600	0.1	44.0	4600	2.9	7260	112.0	250	0.58
WE	2.84	100	960000	122	36300	>0.2	744.0	2000	-1.2	260	40.0	425	1.33

Appendix E Sample and site catalogue 2012-2013

Site	Sample	Description
1	NW 1a	Tephra sized piece of volcanic rock in base of bubbling fumarole/water outflow vent in creek next to iron crust NW 5, (temperature 80 ℃.
	NW 1b	Unconsolidated sediment taken from inside bubbling fumarole/water outflow vent in creek next to iron crust NW 5.
	NW 5a	Hard iron rich layer, yellow/orange to deep red colour. Temperature under iron layer was 35 deg c, (Same as sample number W125 (Letham-Brake, 2013)).
	NW 5b	Hard iron rich layer, yellow/orange to deep red colour. bulk sample of NW 5 were also taken for analysis.
2	NW 2a	White microbial filaments in creek above thin iron layer coating the bottom of creek, water temp approx 40 ℃.
	NW 2b	Iron crust (precipitate) coating bottom of creek under white microbe filament mass.
3	NW 3	Sample number J04 Mark Letham-Brake) Fine red clay layer, taken from behind Donald duck
	NW 4	Sample number J05 Mark Letham-Brake) Light grey clay layer below the red clay NW 3.
4	NW 6	Sediment and precipitates from a stream feed by an very active hotpool.
5	Carbon 1	1/1: 0cm - surface of Fe-rich subsurface layer, outcropping in creek, hard cemented lapilli ash
		1/2: 5cm - middle of Fe-rich subsurface layer, hard cemented lapilli ash
		1/3: 10cm - bottom of Fe-rich subsurface layer and top of grey precipitate rich layer
		1/4: 15cm - Grey precipite rich layer, coarse ash and lapilli saturated with light yellow grey precipitates
		1/5: 20cm - Grey precipite rich layer, fine to coarse ash saturated with light yellow grey precipitates
		1/6: 30cm - interface between grey and redish precipitate layer coarse ash to lapilli
		1/7: 40cm - redish precipitate layer coarse ash to lapilli
	NW 13a	Subsurface Fe-rich precipitate layer (near NW 5)(orange, red colour) hard consolidated layer out cropping in stream

Continued on next page

Table 1 – continued from previous page

Site	Sample	Description
	NW 13b	Bulk sample of Fe-rich precipitate layer (near NW 5)(orange, red colour) hard consolidated layer out cropping in stream
	NW 14	Yellow/grey precipitate layer, unconsolidated sediment 5cm below NW 13a Fe-rich layer
	NW 15	Grey precipitate layer, unconsolidated sediment 25cm below NW 13a Fe-rich layer
	NW 16	Light red precipitate layer, unconsolidated sediment 35cm below NW 13a Fe-rich layer
6		Subsurface Fe-rich layer outcropping in acid creek, light yellow to deep red from 20cm to 30cm thick
7		Subsurface Fe-rich layer outcropping in acid creek, light yellow to deep red from 20cm to 30cm thick
8		Subsurface Fe-rich layer outcropping in acid creek, light yellow to deep red from 20cm to 30cm thick
9		Subsurface Fe-rich layer outcropping in acid creek, light yellow to deep red from 20cm to 30cm thick
10		Subsurface Fe-rich layer outcropping in acid creek, light yellow to deep red from 20cm to 30cm thick
11	NW 7a	Subsurface Fe-rich layer outcropping in acid creek, light yellow to deep red from 20cm to 30cm thick, samples middle areas of layer very red sections
	NW 7b	Bulk sample of subsurface Fe-rich layer
12		subsurface Fe-rich layer, soft yellow and red layers
13	NW 8	Deep red iron layer with gypsum crystals 1-2 mm thick coating seep in side of creek
14		Subsurface Fe-rich soft yellow and red layers
15		Subsurface Fe-rich soft yellow and red layers
16		Subsurface Fe-rich layer
17		Site with thin iron layers coating creek lots of microbes coating rocks
18		Subsurface Fe-rich layer
19		Subsurface Fe-rich layer
20		Highest mound in middle of crater used to take 360 deg photos of crater
21	Carbon 2	2/1: 0cm - unconsolidated crater fill no precipitates mix of fine ash to coarse lapilli
		2/2: 10cm - Fe-rich precipitate layer cementing coarse ash

Continued on next page

Table 1 – continued from previous page

Site	Sample	Description
		2/3: 20cm - fine black ash layer, little to no precipitates
		2/4: 30cm - Thick Fe rich subsurface precipitate layer yellow colour, lightly cemented ash to coarse lapilli
		2/5: 50cm - Brown to grey layer fine ash to lapilli saturated with precipitates
	NW 11a	Fe-rich precipitate layer, orange red iron layer loosely consolidated hard
	NW 11b	Fe-rich precipitate layer, orange red precipitate from bottle storing NW 11a
22	NW 10a	Fe-rich precipitate layer Soft, orange coloured layer with some small 5 to 10mm hard pieces in layer
	NW 10b	Fe-rich precipitate layer, orange precipitate from the bottle storing NW10a
	NW 10c	sample from top very soft Fe-rich layer some small consolidated pieces (orange colour)
	NW 10d	sample from bottom very soft Fe-rich layer some small consolidated pieces (orange colour)
23		Subsurface Fe-rich layer soft yellow unconsolidated
24	NW 17	Subsurface bulk sample subsurface Fe-rich layer yellow red
25	NW 12	Heavy dark red/brown Fe-precipitate layer coating the bottom of fast hot outflow draining into main stream
26	NW 9	Greenish yellow sulphur deposit near hotpool

Appendix F Full XRF results

Sample number	SiO_2 %	TiO2 %	Al_2O_3 %	Fe_2O_3 (T) %	MnO %	MgO %	CaO %	Na_2O %	K_2O %	P_2O_5 %	SO_3 %	LOI %	Total %
NW 5b	44.03	0.43	5.93	19.05	0.13	9.57	6.07	1.42	2.04	0.08	7.90	3.25	99.90
NW 7a	53.67	0.50	8.54	14.34	0.13	8.88	5.92	1.55	1.36	0.08	2.86	1.71	99.53
NW 7b	55.64	0.57	9.35	15.08	0.09	5.43	4.73	1.69	1.37	0.11	2.71	3.18	99.93
NW 8	41.09	0.43	8.02	16.92	0.08	5.39	9.74	1.46	1.22	0.06	12.91	2.31	99.64
NW 10c	52.12	0.53	9.02	14.33	0.11	6.99	5.34	1.87	1.82	0.07	5.12	2.61	99.93
NW 10d	53.16	0.54	9.24	13.59	0.11	7.27	5.47	1.91	1.78	0.08	4.42	2.35	99.91
NW 13a	52.05	0.51	7.19	15.19	0.12	8.26	5.77	1.69	1.48	0.07	5.33	2.30	99.95
NW 13b	44.01	0.45	6.11	21.60	0.12	8.36	5.03	1.43	1.84	0.09	7.08	3.75	99.87
NW 14	60.74	0.59	8.89	8.68	0.14	9.25	5.95	1.71	1.21	0.06	1.77	0.94	99.92
NW 15	51.57	0.51	12.39	8.20	0.13	8.64	5.50	2.04	1.73	0.07	6.79	2.39	99.95
NW 16	56.34	0.55	12.77	7.36	0.12	8.17	6.71	2.12	1.21	0.08	2.78	1.57	99.77
NW 17	53.49	0.54	9.34	15.05	0.10	6.60	5.51	1.82	1.41	0.06	3.49	2.44	99.86
1/4	54.06	0.56	13.81	6.06	0.09	5.37	4.22	2.30	1.94	0.08	8.10	3.02	99.61
1/5a	62.28	0.62	10.47	6.80	0.12	7.71	5.29	1.99	1.31	0.07	2.96	-0.10	99.52
1/5b	19.40	0.23	29.40	2.74	0.02	1.13	1.18	4.34	2.21	0.09	30.00	9.47	100.21
2/1	55.73	0.56	9.52	14.59	0.12	7.38	5.52	1.80	1.11	0.12	2.00	0.20	98.65
2/3	60.24	0.54	7.60	9.25	0.16	11.43	6.52	1.40	0.94	0.06	1.25	0.62	100.01

Appendix G Full EDS results

Sample site	Number	Description	O mass %	Na mass %	Mg mass %	Al mass %	Si mass %	S mass %	K mass %	Ca mass %	Fe mass %	total %
1	001	Fe-precipitate	39.4	1.6	nd	0.8	nd	14.6	5.5	nd	38.1	100
1	002	Fe-precipitate	39.1	1.8	nd	0.8	nd	14.2	5.2	nd	39.0	100
1	003	Fe-precipitate	39.9	1.7	nd	0.9	nd	14.2	5.5	nd	37.9	100
5	001	Pyroxene	37.4	0.2	9.7	1.4	26.2	0.0	nd	15.6	9.5	100
5	002	Pyroxene	38.0	0.1	10.0	1.3	26.0	nd	0.1	15.5	9.1	100
5	003	Pyroxene	37.7	0.3	10.1	1.2	26.6	0.1	0.2	15.4	8.5	100
5	004	Fe-precipitate edge of pyroxene	39.2	1.2	0.1	0.8	1.5	13.1	5.3	0.2	38.5	100
5	006	Fe-precipitate on edge of pyroxene	38.8	1.2	0.7	0.6	2.0	13.0	4.9	1.0	37.7	100
5	007	Fe-precipitate on edge of pyroxene	38.6	0.3	8.3	1.0	21.2	2.7	1.0	12.6	14.3	100
5	008	Altered volcanic glass and Fe-precipitate	40.3	2.2	1.7	5.6	22.1	5.0	4.0	2.6	16.3	100
7	001	Pyroxene	38.6	0.1	15.7	0.9	27.5	0.0	nd	1.9	15.3	100
7	002	Feldspar	48.6	1.0	0.3	2.9	44.2	0.2	0.3	1.8	0.7	100
7	003	Feldspar	49.1	0.9	0.1	2.3	44.8	0.4	0.4	1.4	0.6	100
7	004	Volcanic glass (groundmass)	41.7	3.3	1.9	8.4	32.0	nd	2.6	4.7	5.4	100
7	005	Volcanic glass (groundmass)	41.9	3.2	2.0	8.2	32.2	0.1	2.4	5.1	4.9	100
7	006	Volcanic glass (groundmass)	42.0	3.4	2.1	8.1	32.1	0.1	2.1	5.0	5.2	100
10	001	Fe-precipitate	39.3	1.2	0.1	0.8	1.8	13.8	6.0	0.1	36.9	100
10	002	Fe-precipitate	39.4	1.2	0.2	0.6	0.7	14.1	5.9	0.0	37.9	100
10	003	Fe-precipitate	39.2	1.1	0.1	1.1	1.5	13.7	5.9	0.0	37.4	100

Appendix H Full Eh/pH and Temperature results

Sample number	water temperature °C	feature	pH	Water Temp pH measurement °C	Eh mv	Water Temp Eh measurement °C
sample 1	21.8	stream	1.054	19.3	168.1	19.1
sample 2	65.0	seep from bank	3.084	18.9	132.1	18.7
sample 3	21.4	stream	1.233	19.1	141.7	19.0
sample 4	28.0	confluence	1.357	18.9	143.7	19.0
sample 5	36.6	confluence	1.44	18.4	143.7	19.1
sample 6	29.0	confluence	1.133	19.1	143.5	18.9
sample 7	42.0	stream	1.917	19.4	202.0	18.3
sample 8	28.8	stream	0.746	19.3	199.7	18.4
sample 9	36.2	stream	0.749	19.0	203.2	18.8
sample 10	41.2	stream	0.730	18.4	204.2	18.8
sample 11	47.0	stream	0.693	18.4	182.2	17.9
sample 12	70.0	stream	0.887	18.4	178.9	18.1
sample 13	23.0	stream	2.414	18.2	180.0	18.3
sample 14	32.2	confluence	1.465	17.8	179.6	18.3
sample 15	26.8	stream	1.339	17.3	177.6	18.2
sample 16	25.8	stream	1.366	17.5	180.4	17.3
sample 17	24.4	stream	1.445	17.4	178.6	17.0
sample 18	22.2	stream	1.454	17.7	176.4	16.6
sample 19	20.8	stream	1.455	17.4	176.4	16.5
sample 20	19.8	stream	1.435	17.2	177.4	18.1
sample 21	16.4	stream	1.443	17.2	122.6	14.9
sample 22	16.4	pool at end of acid stream	1.44	17.0	122	14.8
sample 23	16.2	sea	6.431	17.3	128.2	14.6

Appendix I Full ICP-OES results

Elements	Sample 1	Sample 2	Sample 3	Sample 4	Sample 5	Sample 6	Sample 7	Sample 8
Al	411.947	1.574	278.397	327.610	369.224	769.152	217.252	1352.990
Fe	213.062	28.117	171.915	396.766	545.916	920.764	1268.020	377.892
Mn	6.618	23.145	11.201	18.780	24.467	32.454	40.895	21.636
Ca	733.751	653.090	701.157	987.160	1203.480	1797.740	2226.590	1161.460
K	84.167	114.890	89.982	101.648	110.500	177.585	72.321	271.976
Mg	216.387	655.469	343.044	578.688	746.567	988.245	1209.190	701.542
Na	180.823	740.992	330.435	567.706	755.220	1060.910	1419.800	643.776
P	1.1780		0.7938	0.7745	0.8575	2.1640	0.0246	5.3361
S	1185.570	262.139	952.105	807.643	668.349	921.224	425.775	1449.240
As	0.1415		0.0747	0.0723	0.1399	0.1902	0.0679	0.3817
B	5.394	4.562	4.721	5.170	5.601	8.770	11.349	5.818
Cd					0.0022		0.0110	0.0015
Cr	0.8632		0.5967	0.7798	0.9155	1.9865	0.3642	3.9436
Cu	0.0255		0.0223	0.0376	0.0538	0.1268		0.0955
Li	0.3145	1.5013	0.6345	0.9956	1.2998	1.7625	2.5042	0.7760
Mo								
Ni	0.1214	0.0124	0.0781	0.1009	0.0969	0.2583	0.0268	0.4378
Pb	0.0525			0.0524	0.0983	0.1912	0.3253	0.1495
Sr	2.1056	0.2182	1.4963	1.5586	1.6115	3.1444	1.1845	5.5538
Zn	0.5983	0.0311	1.0279	0.8278	1.1041	1.9212	3.1626	0.6106
Ce	0.2610		0.1573	0.1842	0.2142	0.4177	0.2076	0.6371
Dy	0.0222	0.0084	0.0114	0.0164	0.0195	0.0615	0.0407	0.0347
Er	0.0126	0.0013	0.0081	0.0096	0.0133	0.0450	0.0654	0.0108
Eu	0.0089	0.0008	0.0061	0.0092	0.0113	0.0182	0.0229	0.0153
Ho				0.002424		0.003918	0.006261	0.003745
La	0.0651	0.0014	0.0424	0.0384	0.0358	0.0722	0.0379	0.1063
Nd	0.0916		0.0611	0.0694	0.0812	0.1540	0.1801	0.1212
Pr	0.2325	0.1905	0.2030	0.2014	0.2109	0.2254	0.2244	0.2618
Sm	0.0539		0.0206	0.0346	0.0575	0.1030	0.3191	0.1219
Yb	0.0235	0.0062	0.0183	0.0277	0.0342	0.0534	0.0714	0.0346

Full ICP-OES Analysis Results of water from White Island in ppm, 1 to 22 are creek water samples and 23 is sea water sample from the beach in front of acid creek.

Elements	Sample 9	Sample 10	Sample 11	Sample 12	Sample 13	Sample 14	Sample 15	Sample 16
Al	1338.550	1360.640	1099.190	1058.960	38.901	360.786	326.648	323.809
Fe	368.916	371.957	239.612	221.864	55.746	548.054	398.501	396.602
Mn	21.417	21.452	20.999	22.686	6.500	24.434	18.579	18.540
Ca	1196.850	1178.880	1001.080	1020.100	286.221	1183.670	970.891	971.231
K	275.908	278.391	264.579	269.250	41.316	108.925	100.212	100.324
Mg	711.259	699.647	642.749	690.990	223.811	744.804	576.649	569.713
Na	641.479	646.429	658.549	709.308	196.393	754.977	575.480	570.506
P	5.2176	5.1436	4.1928	4.0822		0.8723	0.7870	0.7654
S	1449.030	1433.700	1265.300	1252.240	602.353	671.516	797.702	805.795
As	0.4065	0.4267	0.3829	0.2193		0.1496	0.0501	0.0700
B	5.751	5.790	5.826	4.927	1.339	5.604	5.248	5.173
Cd							0.0042	
Cr	3.9265	3.9615	3.1553	2.9902	0.0872	0.8969	0.7580	0.7623
Cu	0.0827	0.0819	0.0757	0.0471		0.0654	0.0425	0.0475
Li	0.7709	0.7851	0.7992	0.8535	0.4221	1.2893	1.0024	0.9966
Mo								
Ni	0.4172	0.4085	0.3012	0.2326	0.0100	0.0931	0.1013	0.0920
Pb	0.1529	0.1938	0.0950	0.0716		0.0850	0.0825	0.0697
Sr	5.4887	5.4833	4.8152	4.6491	0.1731	1.5608	1.5228	1.5100
Zn	0.5729	0.5818	0.4804	0.3720	0.2182	1.0969	0.7896	0.7910
Ce	0.6144	0.6255	0.5085	0.4956	0.0102	0.1988	0.1875	0.1981
Dy	0.0350	0.0546	0.0300	0.0279	0.0276	0.0036	0.0086	
Er	0.0109	0.0135	0.0102	0.0039	0.0059	0.0161	0.0105	0.0116
Eu	0.0157	0.0161	0.0136	0.0113	0.0022	0.0110	0.0086	0.0092
Ho								
La	0.1040	0.1082	0.1005	0.0942	0.0066	0.0370	0.0386	0.0365
Nd	0.1272	0.1120	0.1086	0.1146	0.0204	0.0726	0.0604	0.0588
Pr	0.2417	0.2557	0.2406	0.2429	0.1357	0.2027	0.2235	0.2214
Sm	0.1014	0.1227	0.0774	0.1113		0.0671	0.0488	0.0304
Yb	0.0341	0.0344	0.0269	0.0260	0.0090	0.0344	0.0277	0.0276

Full ICP-OES Analysis Results of water from White Island in ppm, 1 to 22 are creek water samples and 23 is sea water sample from the beach in front of acid creek.

Elements	Sample 17	Sample 18	Sample 19	Sample 20	Sample 21	Sample 22	Sample 23
Al	276.464	273.819	269.372	273.122	277.198	278.680	1.806
Fe	338.745	337.641	342.565	346.792	352.169	354.749	1.877
Mn	16.660	16.493	13.982	14.102	14.297	14.441	0.210
Ca	853.688	850.084	809.323	812.603	823.843	828.341	361.743
K	90.938	92.049	80.112	79.747	80.992	80.379	257.467
Mg	510.751	509.412	506.653	501.925	512.895	510.457	1216.970
Na	537.123	532.288	529.504	526.516	530.974	528.343	9928.520
P	0.6084	0.5976	0.7023	0.6628	0.6632	0.7067	0.0355
S	775.230	772.639	822.806	817.066	832.762	832.147	882.892
As	0.0634	0.0759	0.1235	0.1644	0.0677	0.1298	0.0380
B	4.652	4.540	4.601	4.606	4.640	4.653	4.982
Cd							
Cr	0.6373	0.6371	0.6790	0.6912	0.7027	0.7078	0.0208
Cu	0.0352	0.0373	0.0484	0.0541	0.0485	0.0446	
Li	0.9666	0.9472	0.9171	0.9359	0.9474	0.9476	0.2575
Mo							
Ni	0.0845	0.0845	0.0711	0.0941	0.0630	0.0826	
Pb		0.0310	0.0763	0.0940	0.1136	0.0786	0.0301
Sr	1.2949	1.2730	1.0772	1.0943	1.1032	1.1126	7.8642
Zn	0.6718	0.6670	0.7148	0.7405	0.7364	0.7433	
Ce	0.1771	0.1396	0.1519	0.1586	0.1573	0.1589	0.0134
Dy	0.0169		0.0308	0.0196	0.0271		
Er	0.0087	0.0086	0.0119	0.0071	0.0115	0.0061	
Eu	0.0085	0.0076	0.0097	0.0080	0.0074	0.0082	
Ho							
La	0.0304	0.0306	0.0320	0.0311	0.0318	0.0316	
Nd	0.0568	0.0583	0.0668	0.0646	0.0562	0.0849	
Pr	0.2133	0.2111	0.2238	0.2189	0.1981	0.2195	0.1652
Sm		0.0415	0.0466		0.0352	0.0720	0.2220
Yb	0.0244	0.0242	0.0256	0.0251	0.0257	0.0254	

Full ICP-OES Analysis Results of water from White Island in ppm, 1 to 22 are creek water samples and 23 is sea water sample from the beach in front of acid creek.

Appendix J SEM results from first trip, representative picture of each sample

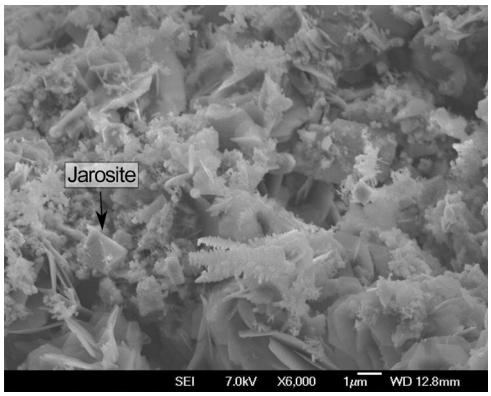

(A) NW1a

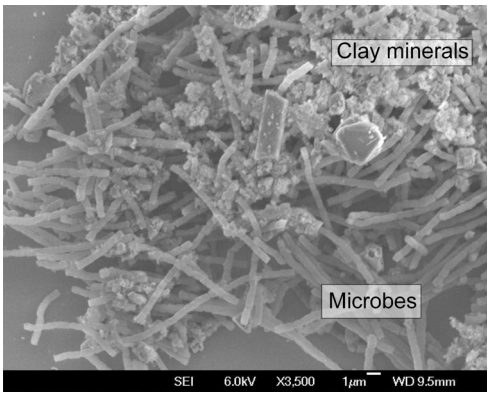

(B) NW1b

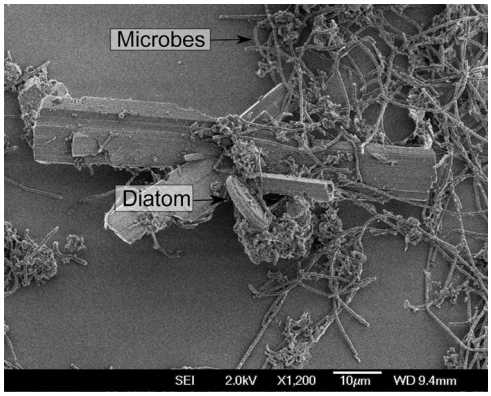

(C) NW2a

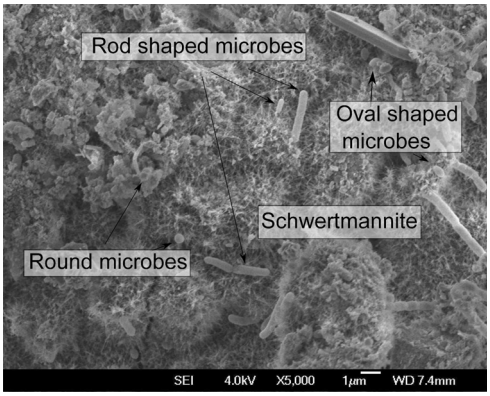

(D) NW2b

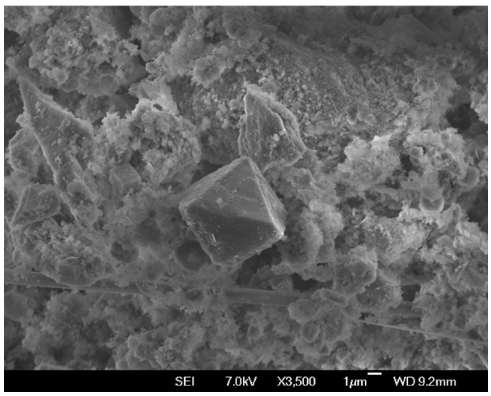

(E) NW3

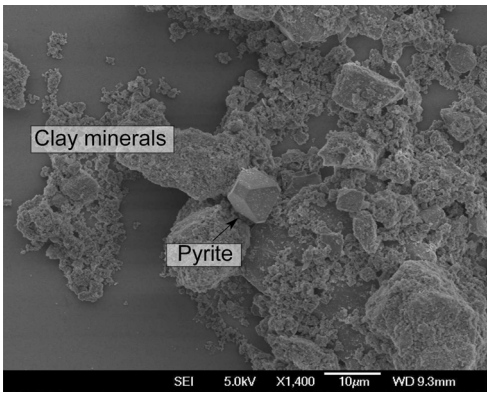

(F) NW4

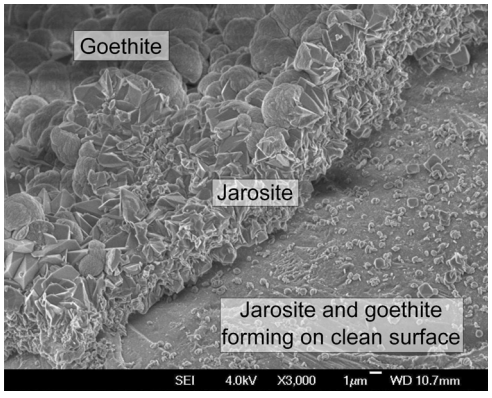

(G) NW5

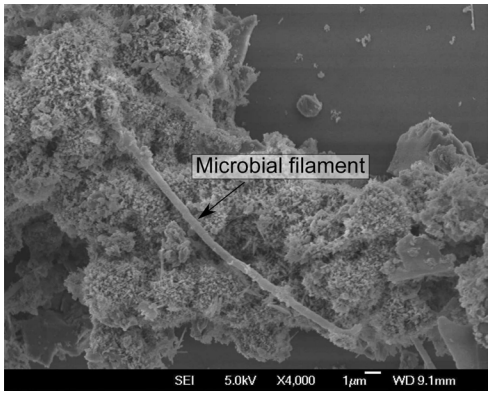

(H) NW6

Appendix K SEM results from second trip, representative picture of each sample

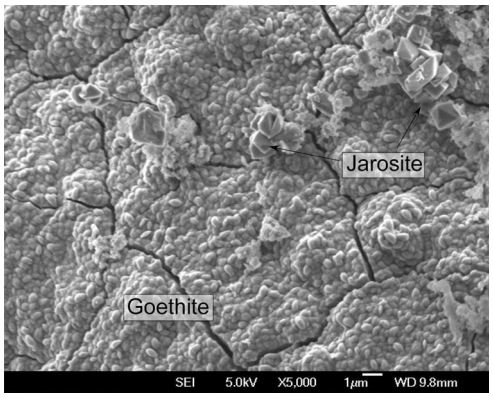

(A) NW7

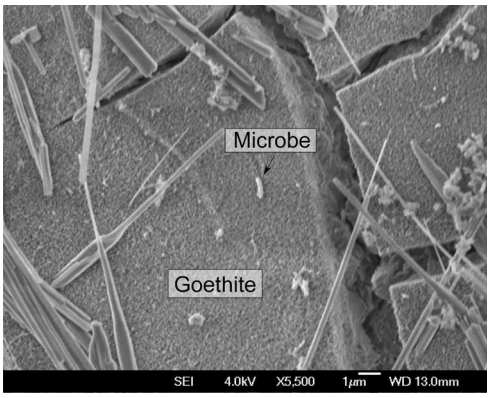

(B) NW8

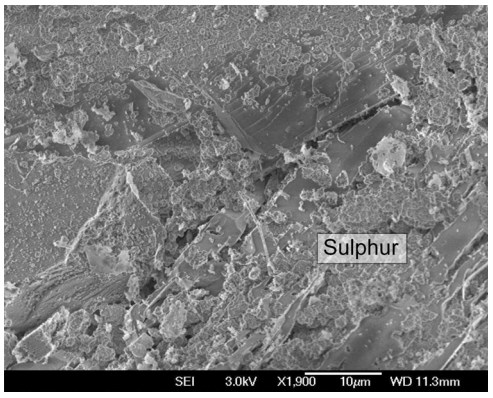

(C) NW9

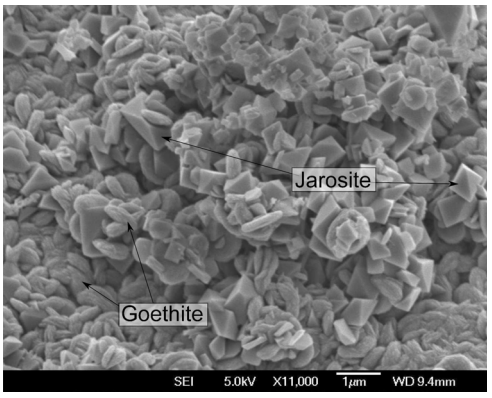

(D) NW10a

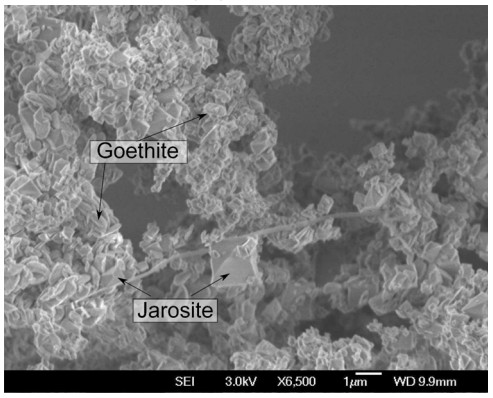

(E) NW10b

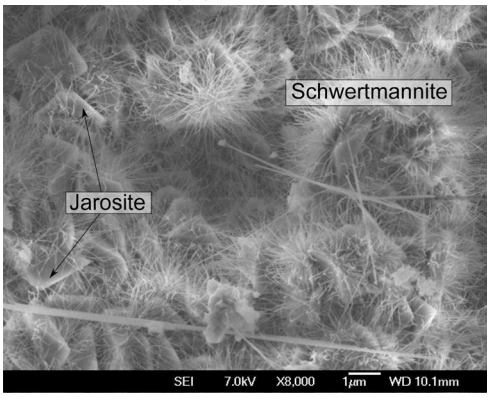

(F) NW11a

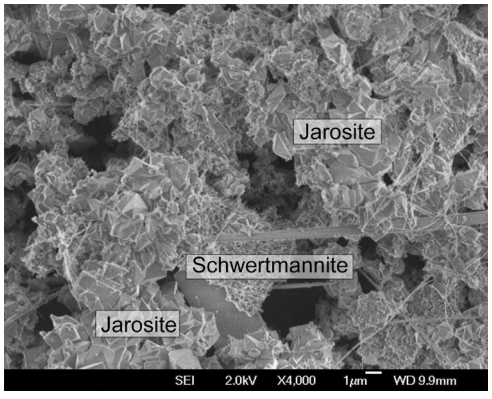

(G) NW11b

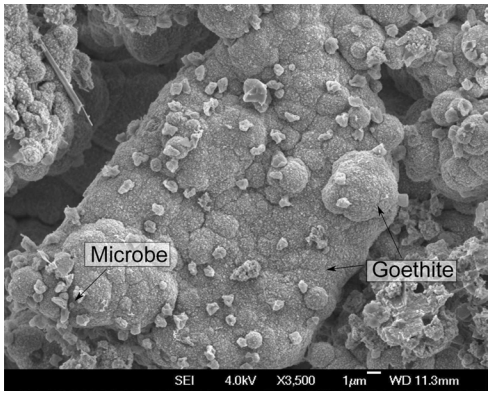

(H) NW12